ヘリオトロン系における
理想MHDモードのグローバルモード解析

陳 勁

博士（学術）

総合研究大学院大学
数物科学研究科
核融合科学専攻

平成１１年３月

Abstract

Ideal magnetohydrodynamics (MHD) equilibria are subjected to two kind of instabilities, i.e., current-driven instabilities and pressure-driven instabilities. In three-dimensional (3-D) configurations with vacuum magnetic flux surfaces , the equilibria can be obtained without net toroidal current, where the current-driven instabilities become unimportant and only the pressure-driven instabilities need to be intensively studied. The pressure-driven modes consists of interchange modes and ballooning modes, and impose MHD stability β limits. [J.P. Freidberg, *Ideal Magnetohydrodynamics*, Plenum Press, New York, 1987]. Interchange modes are basically driven by average unfavorable magnetic curvature. Thus these modes localize on mode rational magnetic field lines and are almost constant along these lines $\boldsymbol{B} \cdot \nabla \xi^{\psi} \approx 0$. On the other hand, ballooning modes are basically driven by locally unfavorable magnetic curvature, so that they localize on unfavorable magnetic curvature region and change along the magnetic field line $\boldsymbol{B} \cdot \nabla \xi^{\psi} \neq 0$. Ballooning modes are considered to be more stringent than interchange modes, whose properties have not yet been clarified in 3-D configurations. To study the properties of ballooning modes, one can proceed in two different ways, namely, local mode analysis and global mode analysis. In axisymmetric systems, the global modes can be constructed easily from the results of the local modes analysis. But this is not the case in non-axisymmetric systems, namely, 3-D systems. In fully 3-D systems, we can only make some conjectures for global modes from the properties of the local modes.

Through the local mode analysis of ballooning modes in an $L = 2/M = 10$ planar axis heliotron system with an inherently large Shafranov shift(where L and M are the polarity and toroidal field period of the helical coils, respectively), it has been demonstrated that [N. Nakajima, Phys. Plasmas **3**, 4545 and 4556(1996)]:

- The local magnetic shear (which is a stabilizing term for high-mode-number ballooning modes) is related to helicity of the helical coils in the considered vacuum

configuration. Its change due to a large Shafranov shift is essentially axisymmetric, i.e., related to toroidicity. This change leads to the disappearance of the (integrated) local magnetic shear on the outer side of torus, even in the region with a stellarator-like global magnetic shear, leading to the destabilization of the high-mode-number ballooning modes.

- The local magnetic curvature (which constructs a potentially destabilizing term for high-mode-number ballooning modes together with the pressure gradient) consists of parts due to both toroidicity and helicity of the helical coils, which determines the 3-D properties of the high-mode-number ballooning modes.

In general 3-D MHD equilibria, the eigenvalues ω^2 for high-mode-number ballooning modes are functions of the labels of the flux surface ψ, the magnetic field line α, and the radial wave number θ_k: $\omega^2 = \omega^2(\psi, \theta_k, \alpha)$. Since ω^2 has no α-dependence in axisymmetric systems, the stronger the α-dependence of ω^2 is (mainly coming from the helicity part of the local magnetic curvature), the more significant the 3-D properties of ω^2 are. The topological properties of the unstable eigenvalues $\omega^2(< 0)$ in (ψ, θ_k, α) space for the $L = 2/M = 10$ planar axis heliotron system are shown that [N. Nakajima, Phys. Plasmas **3**, 4556 (1996)]:

- In Mercier unstable equilibria, there coexist two types of topological level surfaces for ω^2 in (ψ, θ_k, α) space. One is a tokamak-like cylindrical level surface with the axis in α direction, the other is a spheroidal level surface inherent to 3-D systems. The spheroidal level surfaces are surrounded by the cylindrical level surfaces. From their relative positional relation, it is clear that modes with spheroidal level surfaces have larger growth rates than those with cylindrical level surfaces.

- In Mercier stable equilibria, only a topologically spheroidal level surface exists. In contrast to Mercier unstable equilibria, this spheroidal level surfaces are surrounded by the level surfaces of stable Toroidicity-induced Alfvén Eigenmodes (TAE).

From these results it is conjectured that the global structure of pressure-driven modes has the following properties [N. Nakajima, Phys. Plasmas **3**, 4556 (1996)]:

- Global modes that correspond to modes in the local mode analysis with a cylindrical level surface will be poloidal localized tokamak-like ballooning modes or interchange modes. Effects of the toroidal mode coupling on these modes are weak.

- Global modes that correspond to modes in the local mode analysis with a spheroidal level surface will be ballooning modes inherent to 3-D systems, with quite high poloidal and toroidal mode numbers and localized in both the poloidal and toroidal directions. These modes become to be localized within each toroidal field period of the helical coils, as their typical toroidal mode numbers become higher.

- In Mercier unstable equilibria, where both cylindrical and spheroidal level surface coexist, tokamak-like ballooning modes or interchange modes appear when their typical toroidal mode numbers are relatively small. As the typical toroidal mode numbers become larger, ballooning modes inherent to 3-D systems appear with larger growth rates.

- In Mercier stable equilibria, where only a spheroidal level surface exists, only ballooning modes inherent to 3-D systems appear.

The purposes of the work are to confirm the above conjecture and to clarify the inherent properties of pressure-driven modes through a global mode analysis in the $L = 2/M = 10$ planar axis heliotron system with an inherently large Shafranov shift [J. Chen, N. Nakajima, and M. Okamoto, Global mode analysis of ideal MHD modes in a heliotron/torsatron system: I. Mercier-unstable equilibria].

First the Mercier-unstable equilibria are categorized into two types, namely, toroidicity-dominant Mercier-unstable equilibria and helicity-dominant Mercier-unstable equilibria. This categorization is motivated by the conjecture that tokamak-like ballooning modes or interchange modes exist for relatively small toroidal mode numbers, and is related to the local properties of Mercier-unstable equilibria brought by Shafranov shift. The properties of the vacuum configuration are understood as a straight helical configuration toroidally bended. Since the aspect ratio is relatively large: $R_0/a = 7 \sim 8$ [here R_0 and a are the major and minor radii, respectively], the global and local properties of the vacuum configuration are mainly determined by helicity of the helical coils. The properties of the finite-β equilibria are basically understood as a modification of the vacuum configuration by an essentially axisymmetric and inherently large Shafranov shift. As the Shafranov shift becomes larger, the stabilizing term due to the local magnetic shear is more reduced. The toroidicity-dominant Mercier-unstable equilibria are characterized by properties that it is easy for the local magnetic shear to vanish on the outer side of torus, which is brought by a relatively large Shafranov shift. In these equilibria, it is relatively easy for

ballooning modes to be destabilized. The helicity-dominant Mercier-unstable equilibria are characterized by properties that it is hard for the local magnetic shear to vanish on the outer side of torus, which is brought by a relatively small Shafranov shift. In these equilibria, it is relatively hard for ballooning modes to be destabilized. Note that, in both types of equilibria, the Shafranov shift locally reduces (enhances) the unfavorable normal magnetic curvature on the outside (inside) of torus, which is another local property due to Shafranov shift.

On the basis of these considerations, the following two types of Mercier-unstable equilibria have been adopted. The toroidicity-dominant Mercier-unstable equilibrium is created with a peaked pressure profile $P = P_0(1 - \psi_N)^2$ and $\beta_0 = 5.9\%$, under the flux conserving condition, i.e., with a specified profile for the rotational transform. The helicity-dominant Mercier-unstable equilibrium is created with a broad pressure profile $P = P_0(1 - \psi_N^2)^2$ and $\beta_0 = 4.0\%$, under the currentless condition.

The global mode analysis are done by CAS3D2MN, a version of CAS3D: Code for Analysis of the MHD Stability of 3-D equilibrium [C. Schwab, Phys. Fluids B **5**, 3195 (1993)]. CAS3D have been designed to analyze the global ideal MHD modes of 3-D equilibria based on a formulation of the ideal MHD energy principle with incompressibility and fixed boundary in Boozer coordinate system and the application of Ritz-Galerkin method. In CAS3D2MN, a phase-factor transformation was used in order to save memory and flops.

The inverse iteration with spectral shift is an essential concept in the solution of eigenproblems. It is very efficient if the spectral shift is given to be very close to the desired eigenvalue and the initial vector is chosen to be dominant along the corresponding eigenvector. It is demonstrated in our simulation that convergence will occur after only 3 or 4 steps if the spectral shift itself is a good approximation of the desired eigenvalue and the initial vector has dominant component along the corresponding eigenvector. The left problem is how to guess the spectral shift and give a good initial vector. The spectral shift was calculated by matrix transformation in CAS3D2MN. Since the bandwidth will be destroyed by matrix transformation, the resultant memory and flops will be $O(n^2)$ and $O(n^3)$, respectively. It is shown that the use of matrix transformation is unsuitable, not only because it becomes very expensive in the sense of flops and storage but also the problem size we can deal with is limited by the available computer resources. Here this problem is solved by using the Lanczos algorithm with no re-orthogonalization which keeps

the matrix bandwidth from begin to end. The arithmetic operation mainly come from the matrix-vector multiplies and only 3 recently created Lanczos vectors need to be stored. The resultant memory and flops can be controlled to $O(n)$ and $O(n^2)$ order. This iteration process is accelerated by an shift-and-invert technique. In the new version CAS3D2MNv1, an efficient initial vector generation is also introduced [J. Chen, N. Nakajima, and M. Okamoto, Comput. Phys. Commun., **113**, 1 (1998)].

Since the local magnetic curvature due to helicity has the same period M in the toroidal direction as the toroidal field period of the equilibria, the characteristics of the pressure-driven modes in such Mercier-unstable equilibria dramatically change according to how much the local magnetic shear is reduced (whether the equilibrium is toroidicity-dominant or helicity-dominant) and also according to the relative magnitude of the typical toroidal mode numbers n of the perturbations compared with the toroidal field period M of the equilibria.

In the toroidicity-dominant Mercier-unstable equilibria, the pressure-driven modes change from interchange modes with negligible toroidal mode coupling for low toroidal mode numbers $n < M$, to tokamak-like poloidally localized ballooning modes with weak toroidal mode coupling for moderate toroidal mode numbers $n \sim M$, and finally to both poloidally and toroidally localized ballooning modes purely inherent to 3-D systems with strong poloidal and toroidal mode couplings for fairly high toroidal mode numbers $n \gg M$. Strong toroidal mode coupling, in cooperation with the poloidal mode coupling, makes the perturbation localize to flux tubes.

In the helicity-dominant Mercier-unstable equilibria, the pressure-driven modes change from interchange modes, with negligible toroidal mode coupling for $n < M$ or with weak toroidal mode coupling for $n \sim M$, directly to poloidally and toroidally localized ballooning modes purely inherent to 3-D systems with strong poloidal and toroidal mode couplings for $n \gg M$.

In the Mercier-unstable equilibria, interchange modes with low toroidal mode numbers $n < M$, experiencing the unfavorable magnetic curvature with its local structure averaged out, occur for both toroidicity-dominant and helicity-dominant equilibria. For fairly high toroidal mode numbers $n \gg M$, the perturbations can feel the fine local structure of the magnetic curvature due to helicity and also the local magnetic shear is reduced more or less in both types of equilibria, and consequently poloidally and toroidally localized ballooning modes inherent to 3-D systems are destabilized for both toroidicity-dominant and helicity-

dominant Mercier-unstable equilibria. The situation for moderate toroidal mode numbers $n \sim M$ is different. The local magnetic shear is more reduced in toroidicity-dominant Mercier-unstable equilibria than in helicity-dominant Mercier-unstable equilibria, and also the modes with moderate toroidal mode numbers $n \sim M$ can not effectively feel the local structure of the normal magnetic curvature due to helicity. Thus, tokamak-like poloidally localized ballooning modes with a weak toroidal mode coupling can be easily destabilized for toroidicity-dominant Mercier-unstable equilibria, and interchange modes, driven by the average unfavorable magnetic curvature and not experiencing the effect of toroidal mode coupling, can be destabilized for helicity-dominant Mercier-unstable equilibria. Since the normal magnetic curvature becomes more unfavorable on the inner side than on the outer side of the torus by the Shafranov shift, the interchange modes are localized on the inner side of the torus for both types of equilibria. This type of interchanges mode is anti-ballooning with respect to the poloidal mode coupling.

In both types of Mercier-unstable equilibria, the pressure-driven modes, i.e., ballooning modes and interchange modes, become more unstable and more localized both on flux tubes and in the radial direction, and have stronger toroidal mode coupling through the normal magnetic curvature due to helicity, as the typical toroidal mode numbers increase. Thus, we can expect that ballooning modes localized in one toroidal field period, as suggested in [N. Nakajima, Phys. Plasmas **3**, 4556 (1996)], may occur with very narrower radial extent and larger growth rates, as the typical toroidal mode numbers become larger and larger. All of these properties of the pressure-driven modes in two types of Mercier-unstable equilibria are quite consistent with the conjecture from local mode analysis. These properties are independent of the mode family. (J. Chen, N. Nakajima, and M. Okamoto, Global mode analysis of ideal MHD modes in a heliotron/torsatron system: I. Mercier-unstable equilibria)

Acknowledgments

First of all, I would like to thank Professor M.Okamoto, whose elaborate guidance and continuous encouragement with generosity benefit me throughout my graduate study. Moreover, I'd like very much to thank him to give me this chance to study plasma physics in School of Mathematical and Physical Science, Graduate University for Advanced Studies (GUAS) in Japan.

I gratefully acknowledge Dr N. Nakajima, for his kind support and elaborate guidance based on the remarkable understanding in physics throughout my doctor course. He has many bright ideas, by which I am always enlightened. Without his helps over my work, the completion of this thesis would not have been possible.

My appreciation is extended to Professor T. Torii of Nagoya University for his kindness and valuable discussions. Professor T. Torii retired in March, 1998 from Nagoya University, and continues Professor life in Nanzan University from April 1998.

I would like very much to thank Dr. K. Ichiguchi for his valuable suggestions, discussions, and assistance in the past three years.

I am greatly indebted to Prof. J. Nührenberg and Dr C. Nührenberg for providing us the CAS3D2MN code to implement this work.

I wish to express my many gratitude to Dr Y. Sugiura of Nagoya University (1998) and Dr S.L. Zhang of the University of Tokyo for their suggestive discussions.

I am indebted to all other members of Theory and Data Analysis Division of NIFS for their helps in my research and life outside plasma physics.

The numerical calculations were performed on the Super SX-4 computing system in NIFS. Here I also wish to express my gratitude to the kind cooperation from "workgr" in Theory and Computer Simulation Center of NIFS.

Financial support by Research Fellow of the Japan Society for the Promotion of Science (JSPS Research Fellow) is also acknowledged.

Special thanks go to my husband, Weixing Wang, for his constant mental support and encouragement throughout my graduate life; and to my daughter, Lianyi Wang, whose laughter and growth lightup every second of my day, and is my forever support.

Contents

Chapter 1

Introduction

The Magnetohydrodynamic (MHD) stability analysis is formulated first as an initial value problem ($\rho\frac{\partial^2\boldsymbol{\xi}}{\partial t^2} = \boldsymbol{F}(\boldsymbol{\xi})$). Here ρ is the mass density, $\boldsymbol{F}$ is called the force operator, and $\boldsymbol{\xi}$ stands for the plasma displacement from an equilibrium state $(\boldsymbol{J}_0, \boldsymbol{B}_0, p_0)$. $\boldsymbol{J}_0$, $\boldsymbol{B}_0$, and p_0 are the current density, magnetic field, and pressure profile, respectively. The initial value approach has the advantage of directly determining the actual time evolution of a given initial perturbation. It is also useful in the numerical formulation of the full nonlinear problem. The drawback is that it often contains much more information than is required to determine stability, leading to that numerical calculations are usually very expensive.

A more efficient way to study the linear stability is to reformulate the initial value problem as a normal mode problem by assuming a time dependence of the form $\boldsymbol{\xi}(\boldsymbol{r}, t) = \boldsymbol{\xi}(\boldsymbol{r})exp(-i\omega t)$, where ω is a frequency or a growth rate of the normal mode. The resulting system has the form of three coupled homogeneous partial differential equations, with eigenvalue ω^2 ($-\omega^2\rho\boldsymbol{\xi} = \boldsymbol{F}(\boldsymbol{\xi})$). $\boldsymbol{F}$ possesses an important mathematical property, namely, self-adjointness. This leads to the conclusion that ω^2 is purely real and the discrete normal modes are orthogonal to each other. Therefore, $\omega^2 > 0$ indicates a purely oscillation, and $\omega^2 < 0$ indicates an exponential growth or damping.

The most powerful and intuitive way to determine plasma stability is known as the energy principle introduced by Bernstein *et al.* [1]. The physical basis for this principle is the exact, nonlinear conservation of energy in ideal MHD. Stability is tested by examining the sign of potential energy, δW ($\delta W(\boldsymbol{\xi}^*, \boldsymbol{\xi}) = -\frac{1}{2}\int \boldsymbol{\xi}^* \cdot \boldsymbol{F}(\boldsymbol{\xi})d\boldsymbol{r}$) for all allowable displacements, $\boldsymbol{\xi}$. The system is said to be stable if and only if $\delta W \geq 0$. The most unstable trial function that minimize δW is given by $\boldsymbol{\xi}$ satisfying the incompressibility

condition: $\nabla \cdot \boldsymbol{\xi} = 0$.

According to average free energy, the various MHD instabilities that can occur can be divided into two classes, namely, the current-driven instabilities and the pressure-driven instabilities. The former are driven by currents flowing parallel to the equilibrium magnetic field, and the latter are driven by currents flowing perpendicular to this field. The pressure-driven modes can exist even if no net parallel currents are present in the plasma. In the meantime, in three-dimensional (3-D) configurations with vacuum magnetic flux surfaces, the equilibria can be obtained without net toroidal current, where the current-driven instabilities become unimportant and only the pressure-driven instabilities need to be intensively studied. Substantial progresses have already been made in this aspect [2]-[12], and several codes appeared [13], [14], [15], [16], [17].

The pressure-driven modes consists of interchange modes and ballooning modes, and impose MHD stability β limits [18]. As a general feature, interchange modes are driven by the average unfavorable magnetic curvature with local structure averaged out and thus, they are essentially constant along a mode rational magnetic field line: $\boldsymbol{B} \cdot \nabla \boldsymbol{\xi} \approx 0$. They are not sensitive to the change of local magnetic curvature from favorable to unfavorable region, or vice versa. These modes occur in 1-D, 2-D, and 3-D equilibria. However, ballooning modes are basically driven by the locally unfavorable magnetic curvature and hence they change along such a line: $\boldsymbol{B} \cdot \nabla \boldsymbol{\xi} \neq 0$. They are localized in a region where local magnetic curvature is unfavorable. These modes occur only in 2-D and 3-D equilibria.

Interchange modes are very similar in nature to the Rayleigh-Taylor instability [19]. The interchange perturbation can lead to instability depending upon the relative sign of the magnetic field line curvature with respect to the pressure gradient. If the field lines are concave toward the plasma their tension tends to make them shorten and collapse inward. The plasma pressure, on the other hand, has a nature tendency to expand outward. In such cases a perturbation that "interchange" two flux tubes at different radii leads to a system with lower potential energy and hence instability. When the field lines are convex to the plasma, the system is stable to interchange perturbations. From this description it follows that the interchange stabilities represent plasma perturbations which are nearly constant along a field line (i.e., no line bending). Also, interchange modes have a tendency that the growth rates become larger as the perpendicular wave number, i.e., $k_{\parallel}/k_{\perp} \ll 1, k_{\perp} a \gg 1$, where $k_{\parallel}$ and $k_{\perp}$ constitute the two components of wave number $\boldsymbol{k}$ parallel and perpendicular to the magnetic field line, respectively. a is the minor

radius. Thus, if interchange modes are stable in the limit of the infinity perpendicular wave number, then interchange modes with any wave number are stable. These two facts leads to the stabilizing criterion (local mode analysis of interchange modes), which is expressed only by the equilibrium quantities. As such a criterion, Suydam criterion was first derived by Suydam [20] in 1-D system as early as in 1958, under the assumption that the displacement is a highly localized function of radius in the evaluation of δW. This criterion was generalized to 2-D axisymmetric toroidal configuration by Mercier [21] in 1960, and to 3-D non-axisymmetric configuration in [22]. There is an overall review in [23].

Ballooning modes can be destabilized in a system even when the interchange modes are stable. Thus, the former are usually considered to be more stringent than the later. In multi-dimensional geometries the curvature of the magnetic field line often alternates between regions of favorable and unfavorable curvature. Thus, a perturbation that is not constant, but varies slowly along a field line in such a way that the mode is concentrated in the unfavorable curvature region, can lead to more unstable situations than the simple interchange perturbations. In effect, ballooning nature of the perturbation in the unfavorable curvature region increases the pressure-driven destabilizing contribution to δW_F. The local magnetic shear can be helpful in stabilizing ballooning modes through the field line bending. If the localization is not too severe, the accompanying increase in stability from the line bending cannot compensate this destabilizing effect. As well as interchange modes, the most unstable modes occur in the limit of the infinity perpendicular wave number, $k_{\parallel}/k_{\perp} \ll 1$ and $k_{\perp}a \gg 1$. however, their amplitudes changes along the magnetic field line. By exploiting such short perpendicular wavelength nature of the instabilities, the stability of ballooning modes can be investigated by the ballooning equation (local mode analysis of ballooning modes) [23].

To study the properties of ballooning modes, one can proceed in two different ways, namely, local mode analysis mentioned above and global mode analysis. In axisymmetric systems, the global modes can be constructed easily from the results of the local modes analysis [23]. But this is not the case in non-axisymmetric systems, namely, 3-D systems. In fully 3-D systems, we can only make some conjectures for global modes from the properties of the local modes analysis.

3-D non-axisymmetric configurations are very complicate and three different magnetic topologies have been suggested: the stellarator, the heliotron, and the torsatron [18]. Here

we only consider an $L = 2/M = 10$ planar axis heliotron system with an inherently large Shafranov shift, where L and M are the polarity and toroidal field period of the helical coils. In this system, two helical coils have same direction of current flow, and make ten toroidal field period of equilibria. [24].

The equilibria in such a 3-D configurations have been explicitly categorized into strongly Mercier-unstable equilibria and slightly Mercier-unstable equilibria or completely Mercier-stable equilibria according to the Mercier criterion D_M [11],[12]. Through the local mode analysis of ballooning modes for finite-β MHD equilibria in this system, it has been shown that:

1. The local magnetic shear (which makes a stabilizing term for high-mode-number ballooning modes) is related to helicity of the helical coils in the considered vacuum configuration. Its change due to a large Shafranov shift is essentially axisymmetric, i.e., related to toroidicity. This change leads to the disappearance of the (integrated) local magnetic shear on the outer side of the torus, even in the region with a stellarator-like global magnetic shear, resulting in the destabilization of high-mode-number ballooning modes. [11]

2. The local normal magnetic curvature (which constructs a potentially destabilizing term for high-mode-number ballooning modes together with the pressure gradient) consists of parts due to both toroidicity and helicity of the helical coils, which determines the 3-D properties of the high-mode-number ballooning modes.[12]

In 3-D finite-β MHD equilibria, the eigenvalues ω^2 for high-mode-number ballooning modes are functions of the labels of the flux surface ψ, and the magnetic field line α, and the radial wave number θ_k from eikonal representation: $\omega^2 = \omega^2(\psi, \theta_k, \alpha)$. Note that ω^2 has no α-dependence in axisymmetric systems. Therefore, the stronger the α-dependence of ω^2 is (mainly coming from the helicity part of the local magnetic curvature), the more significant the 3-D properties of ω^2 are. The topological properties of the unstable eigenvalues $\omega^2(< 0)$ in (ψ, θ_k, α) space in the $L = 2/M = 10$ planar axis heliotron system with an inherently large Shafranov shift are shown that [12]:

- In Mercier unstable equilibria, there coexist two types of topological level surfaces for ω^2 in (ψ, θ_k, α) space. One is a tokamak-like cylindrical level surface with the axis in α direction, the other is a spheroidal level surface inherent to 3-D systems.

The spheroidal level surfaces are surrounded by the cylindrical level surfaces. From this relative positional relation, it is clear that modes with spheroidal level surfaces have larger growth rates than those with cylindrical level surfaces.

- In Mercier stable equilibria, only a topologically spheroidal level surface exists. In contrast to Mercier unstable equilibria, these spheroidal level surfaces are surrounded by the level surfaces of stable Toroidicity-induced Alfvén Eigenmodes (TAE).

From the results of local mode analysis, it has been conjectured in this system that [12]

- Global modes that correspond to modes in the local mode analysis with a cylindrical level surface will be poloidally localized tokamak-like ballooning modes or interchange modes. Effects of the toroidal mode coupling on these modes are weak.

- Global modes that correspond to modes in the local mode analysis with a spheroidal level surface will be ballooning modes inherent to 3-D systems, with quite high poloidal and toroidal mode numbers and localized in both the poloidal and toroidal directions. These modes become to be localized within each toroidal field period of the helical coils, as their typical toroidal mode numbers become higher.

- In Mercier unstable equilibria, where both cylindrical and spheroidal level surface coexist, poloidally localized tokamak-like ballooning modes or interchange modes appear when their typical toroidal mode numbers are relatively small. As the typical toroidal mode numbers become larger, ballooning modes inherent to 3-D systems appear with larger growth rates and localized in both the poloidal and toroidal directions, which leads to modes localized within each toroidal field period of the helical coils.

- In Mercier stable equilibria, where only a spheroidal level surface exists, only ballooning modes inherent to 3-D systems appear with quite high poloidal and toroidal mode numbers and localized in both the poloidal and toroidal directions. These modes become to be localized within each toroidal field period of the helical coils, as their typical toroidal mode numbers become higher.

The purposes of the work are to confirm the above conjecture and to clarify the inherent properties of pressure-driven modes through a global mode analysis of the ideal

MHD modes in an $L = 2/M = 10$ planar axis heliotron system with an inherently large Shafranov shift.

The global mode analysis are done by CAS3D2MN, a version of CAS3D: Code for Analysis of the MHD modes in 3-D equilibrium [17]. CAS3D have been designed to analyze the global ideal MHD stability of 3-D equilibria based on a formulation of the ideal MHD energy principle in Boozer coordinate system [25] and the application of Ritz-Galerkin method [26]. It deals with the full 3-D problem under the assumption of incompressibility and fixed boundary, and does not use either the stellarator expansion [27] or averaging method [28]. In CAS3D2MN, a phase-factor transformation [26] was used in order to save memory and flops.

The critical part in CAS3D2MN is thought to be a part solving the eigenproblem of a large but sparse, real symmetric band matrix which is usually indefinite. Eigenproblems continue to be an important and highly relevant area of research in numerical linear algebra. By the effort of many well-known people, a sophisticated toolbox of algorithms, together with analysis, became available. The eigenproblem in this work is roughly divided into two parts, namely, to obtain the approximate eigenvalue, and to obtain the exact eigenvalue and eigenfunction by the inverse iteration. The approximate eigenvalue is used as the initial spectral shift of the inverse iteration.

The inverse iteration [29] with spectral shift is an essential concept in the solution of eigenproblems. It is very efficient if the spectral shift is given to be very close to our desired eigenvalue and the starting vector is chosen to be dominant along the corresponding eigenvector. The convergence are quadratic or even cubic (in the diagonalizable case) [30]. The spectral shift was calculated by matrix transformation in CAS3D2MN. Since the bandwidth will be destroyed by matrix transformation, the resultant memory and flops will be $O(n^2)$ and $O(n^3)$, respectively.

With large problems coming into the picture, it soon became clear that the matrix transforming techniques could not solve these problems with reasonable computing resources, and, as an alternative, iterative methods were investigated. Here the Lanczos algorithm with no re-orthogonalization is introduced, which keeps the matrix bandwidth from begin to end [32]. Lanczos and Arnoldi started the research on modern iteration methods [33] [34] in the early 1950s. After a period of little interest in these methods, mainly because of poor understanding of their numerical properties, Paige [35] [36] showed the potential of the Lanczos method. This marked the start of an entire new area of re-

search. In these methods, the given large problem is reduced to a much smaller problem. This smaller problem can then be solved by the standard techniques for dense matrices. The arithmetic operation mainly come from the matrix-vector multiplies and only 3 recently created Lanczos vectors need to be stored. The resultant memory and flops can be controlled to $O(n)$ and $O(n^2)$ order. This process is accelerated by shift-and-invert technique. An efficient starting vector generator is also adopted.

CAS3D2MN is used to analyze the global modes in Mercier-unstable equilibria of $L = 2/M = 10$ planar axis heliotron system.

The Mercier-unstable equilibria are categorized into two types, viz., toroidicity-dominant Mercier-unstable equilibria and helicity-dominant Mercier-unstable equilibria. This categorization comes from the change of local properties of Mercier-unstable equilibria brought by an essentially axisymmetric, inherently large Shafranov shift. The toroidicity-dominant Mercier-unstable equilibria are less Mercier unstable than helicity-dominant Mercier-unstable equilibria.

Perturbations with long wavelength mainly utilize the average unfavorable magnetic curvature and perturbations with short wavelength can effectively utilize the local unfavorable magnetic curvature. The 3-D equilibria considered here have toroidal field period M, and this is what mainly determines the toroidal period of the local magnetic curvature due to helicity. Considering that perturbations with long wavelength mainly utilize the average unfavorable magnetic curvature and perturbations with short wavelength can effectively utilize the local unfavorable magnetic curvature, we investigate the inherent properties of pressure-driven modes by changing relative magnitude of the typical toroidal mode number of the perturbation, n, as compared to the toroidal period of the local magnetic curvature due to helicity, M: namely, $n < M$, $n \sim M$, and $n \gg M$.

This thesis is organized as follows. In chapter 2, we review the energy principle in general configuration, particular we will concentrate on an intuitive form, which clearly shows the role played by different physical mechanisms. In chapter 3, the results from local mode analysis will be reviewed in an $L = 2/M = 10$ planar axis heliotron system with an inherently large Shafranov shift in detail. Code CAS3D and CAS3D2MN are the basis of this work and we will review them in chapter 4. Some techniques which are important in the present global mode analysis, such as the selection of Fourier modes of equilibria, the construction of Fourier modes of perturbation, and radial resolution, etc., will be discussed in detail. In chapter 5, we introduce an efficient eigensolver, the Lanczos

recursion, which is an iterative subspace method [39]. The main results of global mode analysis is given in chapter 6. According to the characteristics of equilibria, the Mercier-unstable equilibria are categorized into toroidicity-dominant Mercier-unstable equilibria and helicity-dominant Mercier-unstable equilibria. Then, the global mode analysis are carried out for the toroidicity-dominant Mercier-unstable equilibria and helicity-dominant Mercier-unstable equilibria. Finally we summarize the main results obtained in this work in the chapter 7.

We use the standard notation to distinguish scalars (lower- or upper-case italic letters) and vectors (lower- or upper-case bold letters), such as

$$(\boldsymbol{B}\cdot\nabla)\boldsymbol{B} = B\frac{\partial}{\partial s}(B\boldsymbol{b}) = \boldsymbol{b}\frac{\partial}{\partial s}\frac{B^2}{2} + \boldsymbol{n}\frac{B^2}{R}$$

except in chapter 5, where the upper-case bold letters are used to denote matrices, such as

$$\|\boldsymbol{q}\| = \sqrt{\boldsymbol{q}^T\boldsymbol{q}}, \quad \|\boldsymbol{A}\| = \sup_{\|\boldsymbol{q}\|=1}\|\boldsymbol{A}\boldsymbol{q}\|,$$

Chapter 2

The Energy Principle

The two most important and interesting concepts in ideal MHD studies are equilibrium and its stability [18]. The equilibrium given by

$$\begin{aligned} \boldsymbol{J}_0 \times \boldsymbol{B}_0 &= \nabla p_0 \\ \nabla \times \boldsymbol{B}_0 &= \boldsymbol{J}_0 \\ \nabla \cdot \boldsymbol{B}_0 &= 0 \end{aligned} \tag{2.1}$$

in a static system describes a multi-dimensional system which poses completely force balance: radial force and/or toroidal force balance. Whether this system is linearly stable or not is judged by an energy principle [1] based upon the lineralization of the ideal MHD model [18]:

$$\begin{aligned} &\frac{\partial \rho}{\partial t} + \nabla \cdot (\rho \boldsymbol{v}) = 0 \\ &\rho \frac{\partial \boldsymbol{v}}{\partial t} = \boldsymbol{J} \times \boldsymbol{B} - \nabla p \\ &\frac{d}{dt}\left(\frac{p}{\rho^\gamma}\right) = 0 \\ &\boldsymbol{E} + \boldsymbol{v} \times \boldsymbol{B} = 0 \\ &\nabla \times \boldsymbol{E} = -\frac{\partial \boldsymbol{B}}{\partial t} \\ &\nabla \times \boldsymbol{B} = \boldsymbol{J} \\ &\nabla \cdot \boldsymbol{B} = 0 \end{aligned} \tag{2.2}$$

In these equations, the electromagnetic variables are electric field $\boldsymbol{E}$, the magnetic field

$\boldsymbol{B}$, and the current density $\boldsymbol{J}$. The fluid variables are the mass density ρ, the fluid velocity $\boldsymbol{v}$, and the pressure p. Also, $\gamma = \frac{5}{3}$ is the ratio of specific heats and $\frac{d}{dt} = \frac{\partial}{\partial t} + \boldsymbol{v} \cdot \nabla$ is the convective derivative.

The physical basis for the Energy Principle is the fact that energy is exactly conserved in the ideal MHD model. As a consequence, the extremum corresponding to the most negative eigenvalue for ω^2 [1] actually represents a minimum in potential energy δW. This in turn implies that the question of stability or instability can be determined by analyzing only the sign of $\delta W(\boldsymbol{\xi}^*, \boldsymbol{\xi})$. Specifically, the Energy Principle states that an equilibrium given by (2.1) is linearly stable if and only if [40]

$$\delta W(\boldsymbol{\xi}^*, \boldsymbol{\xi}) \geq 0 \tag{2.3}$$

for all allowable displacements $\boldsymbol{\xi}$ (i.e., $\boldsymbol{\xi}$ bounded in energy and satisfying appropriate boundary conditions); that is, if the minimum of the potential energy is positive for all displacements, the system is stable. If it is negative for any displacement, the system is unstable. Here

$$\delta W(\boldsymbol{\xi}^*, \boldsymbol{\xi}) = -\frac{1}{2} \int \boldsymbol{\xi}^* \cdot \boldsymbol{F}(\boldsymbol{\xi}) d\boldsymbol{r} \tag{2.4}$$

with $\boldsymbol{F}(\boldsymbol{\xi})$ a self-adjoint operator

$$\boldsymbol{F}(\boldsymbol{\xi}) = (\nabla \times \boldsymbol{B}) \times \boldsymbol{Q} + (\nabla \times \boldsymbol{Q}) \times \boldsymbol{B} + \nabla(\boldsymbol{\xi} \cdot \nabla p + \gamma p \nabla \cdot \boldsymbol{\xi}) \tag{2.5}$$

where $Q = \nabla \times (\boldsymbol{\xi} \times \boldsymbol{B})$ is the perturbed magnetic field, and the third term represents the perturbed pressure. Here all perturbed quantities have been expressed in terms of $\boldsymbol{\xi}$ and the zero subscript has been dropped from all equilibrium quantities for convenience.

Separating $\boldsymbol{\xi}^*$ as $\boldsymbol{\xi}_\perp^*$ and $\xi_\parallel^*$, we can rearrange the first term and the the first part in the third term as

$$\begin{aligned} &\boldsymbol{\xi}^* \cdot [(\nabla \times \boldsymbol{B}) \times \boldsymbol{Q} + \nabla(\boldsymbol{\xi} \cdot \nabla p)] = \\ &\boldsymbol{\xi}_\perp^* \cdot [(\nabla \times \boldsymbol{B}) \times \boldsymbol{Q} + \nabla(\boldsymbol{\xi} \cdot \nabla p)] + \xi_\parallel^* \frac{\boldsymbol{B}}{B} \cdot [(\nabla \times \boldsymbol{B}) \times \boldsymbol{Q} + \nabla(\boldsymbol{\xi} \cdot \nabla p)]. \end{aligned} \tag{2.6}$$

Since

$$\begin{aligned} \boldsymbol{B} \cdot (\nabla \times \boldsymbol{B}) \times \boldsymbol{Q} &= B \times \boldsymbol{J} \cdot \boldsymbol{Q} = -\nabla p \cdot \boldsymbol{Q} = -\nabla p \cdot \nabla \times (\boldsymbol{\xi} \times \boldsymbol{B}) \\ &= -(\boldsymbol{\xi} \times \boldsymbol{B}) \cdot \nabla \times \nabla p + \nabla \cdot (\nabla p \times (\boldsymbol{\xi} \times \boldsymbol{B})) \\ &= -\nabla \cdot ((\boldsymbol{\xi} \cdot \nabla p) \boldsymbol{B}) \quad (\nabla p \cdot \boldsymbol{B} = 0) \\ &= -\boldsymbol{B} \cdot \nabla(\boldsymbol{\xi} \cdot \nabla p) \quad (\nabla \cdot \boldsymbol{B} = 0), \end{aligned} \tag{2.7}$$

[1] ω^2 ($-\omega^2 \rho \boldsymbol{\xi} = \boldsymbol{F}(\boldsymbol{\xi})$). $\boldsymbol{F}$ is given by (2.5)

the last term in (2.6) is dropped. Considering the fixed boundary problem only, the basic form (2.4) can be expressed as

$$\delta W_F = \frac{1}{2}\int dr \left[|\boldsymbol{Q}|^2 - \boldsymbol{\xi}_\perp^* \cdot \boldsymbol{J}\times\boldsymbol{Q} + \gamma p|\nabla\cdot\boldsymbol{\xi}|^2 + (\boldsymbol{\xi}_\perp\cdot\nabla p)\nabla\cdot\boldsymbol{\xi}_\perp^*\right] \tag{2.8}$$

where $\boldsymbol{\xi}^*\cdot\nabla p = \boldsymbol{\xi}_\perp^*\cdot\nabla p + \xi_\parallel^*\dfrac{\boldsymbol{B}}{B}\cdot\nabla p = \boldsymbol{\xi}_\perp^*\cdot\nabla p.$

Define $\boldsymbol{b} = \dfrac{\boldsymbol{B}}{B}$ to be the local unit vector tangential to the magnetic field line, and $\boldsymbol{\kappa} = \boldsymbol{b}\cdot\nabla\boldsymbol{b}$ to be the local magnetic curvature. By carefully rearranging the terms in the integrand of (2.8)

$$\begin{aligned}
&|\boldsymbol{Q}|^2 = |\boldsymbol{Q}_\perp|^2 + |Q_\parallel|^2\\
&\boldsymbol{\xi}_\perp^*\cdot\boldsymbol{J}\times\boldsymbol{Q} = J_\parallel(\boldsymbol{\xi}_\perp^*\times\boldsymbol{b})\cdot\boldsymbol{Q}_\perp + Q_\parallel\boldsymbol{\xi}_\perp^*\cdot\boldsymbol{J}_\perp\times\boldsymbol{b}\\
&\boldsymbol{J}_\perp = \frac{\boldsymbol{b}\times\nabla p}{B}\\
&Q_\parallel \quad = \boldsymbol{b}\cdot\nabla\times(\boldsymbol{\xi}_\perp\times\boldsymbol{B})\\
&\qquad = \boldsymbol{b}\cdot[(\boldsymbol{B}\cdot\nabla)\boldsymbol{\xi}_\perp - (\boldsymbol{\xi}_\perp\cdot\nabla)\boldsymbol{B} - \boldsymbol{B}\nabla\cdot\boldsymbol{\xi}_\perp]\\
&\qquad = [(\boldsymbol{B}\cdot\nabla)(\boldsymbol{\xi}_\perp\cdot\boldsymbol{b}) - \boldsymbol{\xi}_\perp\cdot((\boldsymbol{B}\cdot\nabla)\boldsymbol{b})] - \boldsymbol{b}\cdot[\nabla\boldsymbol{B}\cdot\boldsymbol{\xi}_\perp - \boldsymbol{\xi}_\perp\times(\nabla\times\boldsymbol{B})] - B(\nabla\cdot\boldsymbol{\xi}_\perp)\\
&\qquad = -B\boldsymbol{\xi}_\perp\cdot(\boldsymbol{b}\cdot\nabla\boldsymbol{b}) - (\boldsymbol{b}\cdot\nabla\boldsymbol{B})\cdot\boldsymbol{\xi}_\perp + \boldsymbol{b}\cdot\boldsymbol{\xi}_\perp\times\boldsymbol{J} - B(\nabla\cdot\boldsymbol{\xi}_\perp)\\
&\qquad = -B(\nabla\cdot\boldsymbol{\xi}_\perp + 2\boldsymbol{\xi}_\perp\cdot\boldsymbol{\kappa}) + \frac{1}{B}\boldsymbol{\xi}_\perp\cdot\nabla p
\end{aligned} \tag{2.9}$$

expression (2.8) can be casted into an intuitive form

$$\begin{array}{lccccc}
\delta W_F = & \frac{1}{2}\int dr[& |\boldsymbol{Q}_\perp|^2 & + & B^2|\nabla\cdot\boldsymbol{\xi}_\perp + 2\boldsymbol{\xi}_\perp\cdot\boldsymbol{\kappa}|^2 & + \quad \gamma p|\nabla\cdot\boldsymbol{\xi}|^2\\
 & & \text{shear Alfvén mode} & & \text{Fast mode} & \text{Slow mode}\\
 & & -2(\boldsymbol{\xi}_\perp\cdot\nabla p)(\boldsymbol{\kappa}\cdot\boldsymbol{\xi}_\perp^*) & & -J_\parallel(\boldsymbol{\xi}_\perp^*\times\boldsymbol{b})\cdot\boldsymbol{Q}_\perp &].\\
 & & \text{pressure-driven term} & & \text{current-driven term} &
\end{array} \tag{2.10}$$

The terms in the above equation have the following physical interpretation. The $|\boldsymbol{Q}_\perp|^2$ term represents the energy required to bend magnetic field lines. It is the dominant potential energy contribution to the shear Alfvén wave. The second term corresponds to the energy necessary to compress the magnetic field and describes the major potential energy contribution to the compressional Alfvén wave. The $\gamma p|\nabla\cdot\boldsymbol{\xi}|^2$ term represents the energy required to compress the plasma. It is the main source of potential energy for the sound wave. Each of the contributions just described is stabilizing. The remaining

two terms can be positive or negative and thus can drive instabilities. The first of this is proportional to $\nabla p \sim \boldsymbol{J}_\perp \times \boldsymbol{B}$ while the second is proportional to $J_\parallel$. Thus, either perpendicular or parallel currents represent potential sources of instabilities. The former type are referred to pressure-driven instabilities and the latter referred to current-driven instabilities.

Here it is useful to understand the meaning of the net toroidal current. From (2.1), we have

$$\nabla \cdot \boldsymbol{J} = 0 \tag{2.11}$$

and

$$\begin{aligned} \boldsymbol{J} &= \frac{\boldsymbol{J}\cdot\boldsymbol{B}}{B^2}\boldsymbol{B} + \frac{\boldsymbol{B}\times\nabla p}{B^2} \\ &\equiv J_\parallel \boldsymbol{b} + \boldsymbol{J}_\perp. \end{aligned} \tag{2.12}$$

Then

$$\nabla \cdot (\frac{\boldsymbol{J}\cdot\boldsymbol{B}}{B^2}\boldsymbol{B}) = -\nabla\cdot\boldsymbol{J}_\perp \tag{2.13}$$

and we can get a magnetic differential equation for the parallel current

$$\boldsymbol{B}\cdot\nabla(\frac{\boldsymbol{J}\cdot\boldsymbol{B}}{B^2}) = -\nabla\cdot\boldsymbol{J}_\perp. \tag{2.14}$$

since $\nabla\cdot\boldsymbol{B} = 0$. $\boldsymbol{J}\cdot\boldsymbol{B}$ consists of two components, i.e.,

$$\begin{aligned} \boldsymbol{J}\cdot\boldsymbol{B} = \quad & (\boldsymbol{J}\cdot\boldsymbol{B})_{\rm PS} \quad + \quad \frac{B^2}{\langle B^2\rangle}\langle \boldsymbol{J}\cdot\boldsymbol{B}\rangle. \\ & \text{Pfirsch-Schluter current} \qquad \text{net toroidal current} \end{aligned} \tag{2.15}$$

$(\boldsymbol{J}\cdot\boldsymbol{B})_{\rm PS} \propto \dfrac{dp}{d\psi}$ and this term is zero when averaged on the flux surface: $\langle(\boldsymbol{J}\cdot\boldsymbol{B})_{\rm PS}\rangle = 0$. Here ψ is the flux surface label. The second term on the right-hand-side of (2.15) is an average on the flux surface. According to this term being zero or not, an equilibrium can be said to be with or without net toroidal current.

The pressure-driven modes can be destabilized even if there is no net parallel current. Moreover, In 3-D configurations with vacuum magnetic flux surfaces, the equilibria can be obtained without net toroidal current. Therefore, the current-driven instabilities become unimportant and only the pressure-driven instabilities need to be intensively studied.

Finally we give a form first introduced by Bernstein *et. al.* [1] and to be used in CAS3D [17].

$$\delta W_F = \frac{1}{2}\int dr[\boldsymbol{Q} + \boldsymbol{n}\cdot\boldsymbol{\xi}\boldsymbol{J}\times\boldsymbol{n}|^2 + \gamma p|\nabla\cdot\boldsymbol{\xi}|^2 - 2\boldsymbol{J}\times\boldsymbol{n}\cdot(\boldsymbol{B}\cdot\nabla\boldsymbol{n})(\boldsymbol{n}\cdot\boldsymbol{\xi})^2] \tag{2.16}$$

where $\boldsymbol{n} = \nabla p/|\nabla p|$ is the unit vector normal to the equilibrium magnetic surfaces.

The energy principle forms the basis of linear stability analysis of ideal MHD[15] [13] [14] [17] [16]. In this work, CAS3D will be used with the application of $\nabla \cdot \boldsymbol{\xi}$. We will give a brief review of CAS3D and its version CAS3D2MN in chapter 4.

Chapter 3

Review of Local Mode Analysis

3.1 Ballooning equation and the Mercier criterion

Modes with infinity wavenumber ($|\boldsymbol{k}_\perp| \to \infty$) and happening to be localized along the field lines, have the largest growth rates. Analysis of this type of modes can be done using eikonal approximation and then solving the resultant ballooning equation.

The high-mode-number ballooning equation can be obtained from the intuitive form (2.10) using an eikonal representation for $\boldsymbol{\xi}_\perp$:

$$\boldsymbol{\xi}_\perp = \boldsymbol{X}_\perp e^{iS}. \tag{3.1}$$

S is called the eikonal. Here it represents the rapid perpendicular motion. The envelop, $\boldsymbol{X}_\perp$ which determines the parallel structure, is assumed to vary "slowly" on the equilibrium length scale: $|a\nabla \boldsymbol{X}_\perp|/|\boldsymbol{X}_\perp| \sim 1$, where a represents the minor radius. By definition,

$$\boldsymbol{B} \cdot \nabla S = 0. \tag{3.2}$$

This leads to the natural definition of the perpendicular wavenumber as

$$\boldsymbol{k}_\perp = \nabla S. \tag{3.3}$$

The assumption $|\boldsymbol{k}_\perp| \to \infty$ implies that the variation of S is rapid: $|a\nabla S| \gg 1$.

By assuming that a physically acceptable function, S, can be found to satisfy $|\boldsymbol{k}_\perp| \to \infty$ and $\boldsymbol{B} \cdot \nabla S = 0$, the intuitive form of δW_F (2.10) can be reformed as

$$\delta W_F = \frac{1}{2}\int dr \quad \underbrace{\left[|\nabla \times (\boldsymbol{X}_\perp \times \boldsymbol{B})_\perp|^2\right.}_{\text{shear Alfvén mode}} + \underbrace{B^2|i\boldsymbol{k}_\perp \cdot \boldsymbol{X}_\perp + \nabla \cdot \boldsymbol{X}_\perp + 2\boldsymbol{\kappa} \cdot \boldsymbol{X}_\perp|^2}_{\text{Fast mode}}$$
$$\underbrace{-2(\boldsymbol{X}_\perp \cdot \nabla p)(\boldsymbol{X}_\perp^* \cdot \boldsymbol{\kappa})}_{\text{pressure-driven mode}} - \underbrace{\left. J_\parallel(\boldsymbol{X}_\perp^* \times \boldsymbol{b}) \cdot \nabla \times (\boldsymbol{X}_\perp \times \boldsymbol{B})_\perp\right]}_{\text{current-driven mode}}. \tag{3.4}$$

The plasma compressibility term is not included and the only explicit appearance of S (i.e., $\boldsymbol{k}_\perp$) occurs in the magnetic compression term. Considering the limit $|\boldsymbol{k}_\perp| \to \infty$ and expanding $\boldsymbol{X}_\perp$ as

$$\boldsymbol{X}_\perp = \boldsymbol{X}_{\perp 0} + \boldsymbol{X}_{\perp 1} + \cdots \tag{3.5}$$

with $|\boldsymbol{X}_{\perp 0}|/|\boldsymbol{X}_{\perp 1}| \sim \frac{1}{k_\perp a}$, we obtain the energy principle of the incompressible high-mode-number ballooning mode[23]

$$\delta W_F = \frac{1}{2}\int dr\left[|\boldsymbol{k}_\perp|^2|\boldsymbol{b} \cdot \nabla\Phi|^2 - \frac{2}{B^2}(\boldsymbol{b} \times \boldsymbol{k}_\perp \cdot \nabla p)(\boldsymbol{b} \times \boldsymbol{k}_\perp \cdot \boldsymbol{\kappa})|\Phi|^2\right] \tag{3.6}$$

where $\boldsymbol{X}_{\perp 0} = \Upsilon \boldsymbol{b} \times \boldsymbol{k}_\perp$ and $\Phi \equiv \Upsilon B$. (3.6) exhibits the competition between the stabilizing effect of the field line bending, representing by $|\boldsymbol{k}_\perp|^2$, and the destabilizing effect of the pressure gradient when the magnetic curvature is unfavorable. In the limit of $|\boldsymbol{k}_\perp| \to \infty$, the unstable modes do not involve any compression of the magnetic field, and the kink term makes no contribution to stability. This will become more clear in chapter 6.

Only considering the perturbation perpendicular to the magnetic field line [23], the kinetic energy can be obtained in the same way.

$$\begin{aligned} K &= \tfrac{1}{2}\int \rho|\boldsymbol{\xi}_\perp|^2 d\boldsymbol{r} = \tfrac{1}{2}\int \rho|\boldsymbol{X}|^2 d\boldsymbol{r} = \tfrac{1}{2}\int \rho|\Upsilon|^2|\boldsymbol{b} \times \boldsymbol{k}_\perp|^2 d\boldsymbol{r} \\ &= \tfrac{1}{2}\int \rho|\frac{|\boldsymbol{k}_\perp|^2}{B^2}|\Phi|^2 d\boldsymbol{r}. \end{aligned} \tag{3.7}$$

Then the Euler equation can be obtained through the variational principle

$$\omega^2 = \frac{\delta W}{K}. \tag{3.8}$$

Letting $\Phi \to \Phi + \delta\Phi$ and $\omega^2 \to \omega^2 + \delta\omega^2$, and setting $\delta\omega^2 \to 0$ in (3.6) and (3.7), the corresponding vector form is an ordinary differential equation in the parallel direction

$$\boldsymbol{B}\cdot\nabla\Big[\frac{|\boldsymbol{k}_\perp|^2}{B^2}\boldsymbol{B}\cdot\nabla\Phi\Big] + \frac{\rho}{B^2}\omega^2|\boldsymbol{k}_\perp|^2\Phi + \frac{2}{B^2}(\boldsymbol{b}\times\boldsymbol{k}_\perp\cdot\nabla p)(\boldsymbol{b}\times\boldsymbol{k}_\perp\cdot\boldsymbol{\kappa})\Phi = 0, \qquad (3.9)$$

which is called the ballooning equation. This is an eigenvalue problem. Physical requirements (periodicity) restrict the allowed solutions of ω^2 and corresponding normal modes.

The Mercier criterion can be given as a function of normalized toroidal flux Φ_T [12]

$$\begin{aligned} D_M = \; & \frac{(\iota')^2}{4} - p'V'[-\langle\frac{B^2}{|\nabla\Phi_T|^2}\rangle V'' + \iota'\langle\frac{(\boldsymbol{J}\cdot\boldsymbol{B})_{PSN}}{|\nabla\Phi_T|^2}\rangle] \\ & -(p'V'')^2[\langle\frac{(\boldsymbol{J}\cdot\boldsymbol{B})^2_{PSN}}{|\nabla\Phi_T|^2B^2}\rangle\langle\frac{B^2}{|\nabla\Phi_T|^2}\rangle \\ & -\langle\frac{(\boldsymbol{J}\cdot\boldsymbol{B})_{PSN}}{|\nabla\Phi_T|^2}\rangle^2 + \langle\frac{B^2}{|\nabla\Phi_T|^2}\rangle\langle\frac{1}{B^2}\rangle]. \end{aligned} \qquad (3.10)$$

Here $\langle f\rangle \equiv (d/dV)\int f d\tau$ (flux surface average) where V is the volume inside a flux surface. Prime indicates the derivative $' \equiv (d/d\Phi_T)$ where Φ_T is related to the toroidal flux inside the flux surface. $(\boldsymbol{J}\cdot\boldsymbol{B})_{PSN}$ represents the Pfirsch-Schluter current divided by p' and is given by

$$(\boldsymbol{J}\cdot\boldsymbol{B})_{PSN} = -\boldsymbol{B}\times\boldsymbol{\nabla}\Phi_T\cdot\nabla\tilde{\beta}_N, \qquad \boldsymbol{B}\cdot\boldsymbol{\nabla}\tilde{\beta}_N = 1 - \frac{B^2}{\langle B^2\rangle}. \qquad (3.11)$$

Mercier stability corresponds to satisfying the condition $D_M > 0$. The first term on the right-hand side of (3.10) represents the stabilizing effect of global magnetic shear. The last term is destabilizing, due to the Pfirsch-Schluter current (geodesic curvature) and the diamagnetic current. only the second term can change sign, depending on the average magnetic well index V'' and the global magnetic shear ι'.

3.2 Local mode analysis in in heliotron system

In the following analysis, it will be convenient to introduce the Boozer coordinate system (ψ, θ, ζ) [25], with ψ the flux surface label, θ, and ζ the poloidal and toroidal angle-like variables, respectively, The origin for the poloidal angle θ is on the outer side of the torus and the origin for the toroidal angle is on the vertically elongated poloidal cross section.

Here ψ is defined as $\psi = \Phi_t/(2\pi)$ with Φ_t the toroidal flux inside a flux surface. In such a case, the covering space (ψ, η, α) can be given as

$$\begin{aligned} &\eta = \theta, && -\infty < \eta < +\infty \\ &\alpha = \zeta - \theta/\iota, && 0 \le \alpha \le 2\pi/M \end{aligned} \tag{3.12}$$

where α labels the magnetic field line on the flux surface ψ, and ι is the global rotational transform.

$\boldsymbol{k}_\perp$ can be expressed as:

$$\begin{aligned} \boldsymbol{k}_\perp &= k_\alpha \nabla\alpha + k_q \nabla q \\ &= k_\alpha(\nabla\alpha + \theta_k \nabla q) \end{aligned} \tag{3.13}$$

where $\theta_k = k_q/k_\alpha$ is the radial wave number, $k_\alpha = \dfrac{\partial S}{\partial \alpha}$ and $k_q = \dfrac{\partial S}{\partial q}$, and $q = \dfrac{1}{\iota}$.

In the covering space, the high-mode-number ballooning equation (3.9) can be written as

$$\begin{aligned} \frac{\partial}{\partial\eta}\left[|\boldsymbol{k}_\perp|^2 \frac{\partial}{\partial\eta}\Phi\right] &+\Omega^2 \left(\frac{\langle B^2\rangle}{B^2}\right)^2 |\boldsymbol{k}_\perp|^2 \Phi \\ &\frac{2}{B_0}\frac{J + \iota I}{\iota^2}\sqrt{g}\frac{dP}{d\psi}\left[\kappa^n - \kappa_g \int^\eta \hat{s} d\eta\right]\Phi = 0 \end{aligned} \tag{3.14}$$

where $|\boldsymbol{k}_\perp|^2$ has a form

$$|\boldsymbol{k}_\perp|^2 = \frac{|\nabla\psi|^2}{2\psi B_0}\left[\left(\frac{2\psi B}{|\nabla\psi|^2}\right)^2 + \left[\int^\eta \hat{s} d\eta\right]\right]. \tag{3.15}$$

$\Omega = \omega\tau_A$ is the eigenfrequency normalized by the Alfvén time τ_A, which is given by

$$\tau_A^2 = \rho_m / \left(2\pi\iota d\Phi_T/dV\right)^2. \tag{3.16}$$

$2\pi J$ is the poloidal current outside a flux surface and $2\pi I$ is the toroidal current inside.

The local magnetic shear $\hat{s}$ is decomposed into the global magnetic shear s and the oscillatory part $\tilde{s}$ as

$$\hat{s} = \frac{2\psi\sqrt{g}}{\iota}\boldsymbol{s}\cdot\nabla\times\boldsymbol{s} = s + \tilde{s} \tag{3.17}$$

with

$$\begin{aligned} \boldsymbol{s} &= \frac{\nabla\psi\times\boldsymbol{B}}{|\nabla\psi|^2}, \\ s &\equiv \frac{2\psi}{\iota}\frac{d\iota}{d\psi}, \\ \tilde{s} &= \left(\frac{1}{\iota}\frac{\partial}{\partial\zeta} + \frac{\partial}{\partial\theta}\right)\left[\frac{2\psi(Jg_{\psi\theta} - Ig_{\psi\zeta})}{\sqrt{g}|\nabla\psi|^2}\right]. \end{aligned} \tag{3.18}$$

The covariant metrics are given by

$$\begin{aligned} g_{\psi\theta} &= \partial_\psi \boldsymbol{r} \cdot \partial_\theta \boldsymbol{r}, \\ g_{\psi\zeta} &= \partial_\psi \boldsymbol{r} \cdot \partial_\zeta \boldsymbol{r}. \end{aligned} \tag{3.19}$$

The magnetic curvature $\boldsymbol{\kappa}$ is also decomposed into the normal magnetic curvature κ^n and the geodesic magnetic curvature κ_g as

$$\boldsymbol{\kappa} \equiv \boldsymbol{b} \cdot \nabla \boldsymbol{b} = \kappa^n \frac{\nabla \psi}{2\psi} + \kappa_g \boldsymbol{s} \tag{3.20}$$

in which

$$\begin{aligned} \kappa^n &= \frac{2\psi \boldsymbol{\kappa} \cdot \nabla \psi}{|\nabla \psi|^2} = \frac{2\psi}{B^2 |\nabla \psi|^2} \nabla \psi \cdot \nabla \left(p + \frac{B^2}{2} \right). \\ \kappa_g &= \frac{|\nabla \psi|^2}{B^2} \boldsymbol{\kappa} \cdot \boldsymbol{s} = \frac{1}{2} \boldsymbol{B} \times \nabla \psi \cdot \nabla \left(\frac{1}{B^2} \right). \end{aligned} \tag{3.21}$$

The integrated local magnetic shear along a magnetic field line $\int^\eta \hat{s} d\eta$ contributes to the first stability of high-mode-number ballooning modes as stabilizing term, and also does to their second stability together with the geodesic curvature κ_g. The unfavorable normal magnetic curvature κ^n contributes to the first stability of high-mode-number ballooning modes as destabilizing term. It was found from local mode analysis in the $L = 2/M = 10$ planar axis heliotron system with an inherently large Shafranov shift that

- The local magnetic shear (which is a stabilizing term for high-mode-number ballooning modes) is related to helicity of the helical coils in the considered vacuum configuration. Its change due to a large Shafranov shift is essentially axisymmetric, i.e., related to toroidicity. This change leads to the disappearance of the (integrated) local magnetic shear on the outer side of torus, even in the region with a stellarator-like global magnetic shear, leading to the destabilization of the high-mode-number ballooning modes. [11]

- The local magnetic curvature (which constructs a potentially destabilizing term for high-mode-number ballooning modes together with the pressure gradient) consists of parts due to both toroidicity and helicity of the helical coils, which determines the 3-D properties of the high-mode-number ballooning modes. [12]

As a result of these two effects brought by a large Shafranov shift, It was shown [12] that

- In Mercier unstable equilibria, the high-mode-number ballooning modes are unstable, and are destabilized before the stabilizing effects within a single poloidal period along a field line are much suppressed by the Shafranov shift.

- In Mercier stable equilibria, the high-mode-number ballooning modes are unstable, and are destabilized after the stabilizing effects within a single poloidal period along a field line are much suppressed by the Shafranov shift.

In 3-D MHD equilibria, the eigenvalues ω^2 for high-mode-number ballooning modes are functions in the (ψ, θ_k, α) space: $\omega^2 = \omega^2(\psi, \theta_k, \alpha)$. Since ω^2 has no α-dependence in axisymmetric systems, the stronger the α-dependence of ω^2 is (mainly coming from the helicity part of the local magnetic curvature), the more significant the 3-D properties of ω^2 are. The topological properties of the unstable eigenvalues $\omega^2(< 0)$ in (ψ, θ_k, α) space in such planar axis system are shown in [12] that:

- In Mercier unstable equilibria, there coexist two types of topological level surfaces for ω^2 in (ψ, θ_k, α) space. One is a tokamak-like cylindrical level surface with the axis in α direction, The other is a spheroidal level surface inherent to 3-D systems. The spheroidal level surfaces are surrounded by the cylindrical level surfaces. From this relative positional relation, it is clear that modes with spheroidal level surfaces have larger growth rates than those with cylindrical level surfaces.

- In Mercier stable equilibria, only a topologically spheroidal level surface exists. In contrast to Mercier unstable equilibria, this spheroidal level surfaces are surrounded by the level surfaces of stable Toroidicity-induced Alfvén Eigenmodes (TAE).

These are schematically shown in Figure 3.1.

From the results of local mode analysis in an $L = 2/M = 10$ planar axis heliotron system with an inherently large Shafranov shift, it has been conjectured in [12] that

- Global modes that correspond to modes in the local mode analysis with a cylindrical level surface will be poloidally localized tokamak-like ballooning modes or interchange modes. Effects of the toroidal mode coupling on these modes are weak.

- Global modes that correspond to modes in the local mode analysis with a spheroidal level surface will be ballooning modes inherent to 3-D systems, with quite high

poloidal and toroidal mode numbers and localized in both the poloidal and toroidal directions. These modes become to be localized within each toroidal field period of the helical coils, as their typical toroidal mode numbers become higher.

- In Mercier unstable equilibria, where both cylindrical and spheroidal level surface coexist, poloidally localized tokamak-like ballooning modes or interchange modes appear when their typical toroidal mode numbers are relatively small. As the typical toroidal mode numbers become larger, ballooning modes inherent to 3-D systems appear with larger growth rates and localized in both the poloidal and toroidal directions, which leads to modes localized within each toroidal field period of the helical coils.

- In Mercier stable equilibria, where only a spheroidal level surface exists, only ballooning modes inherent to 3-D systems appear with quite high poloidal and toroidal mode numbers and localized in both the poloidal and toroidal directions. These modes become to be localized within each toroidal field period of the helical coils, as their typical toroidal mode numbers become higher.

Chapter 4

CAS3D and CAS3D2MN

CAS3D [17] has been designed to investigate the global ideal MHD stability in fully 3-D configurations under the assumptions of incompressibility and fixed boundary. It was written through the formation of the energy principle (2.8) in Boozer coordinates (ψ, θ, ζ) [25] and the application of Ritz-Galerkin method. The energy principle is reduced to an eigenvalue problem of a large sparse, real symmetric band matrix.

4.1 Mode family

The perturbation can be divided into different independent mode families. In an topological torus with M toroidal field periods there are $1 + [M/2]$ mode families. All of the elements in one mode families belong to one type of perturbation. The mode family has basic index N_f, which changes from 0 to $[M/2]$ and are used to label the mode family. In the same mode family two toroidal mode numbers n^1 and n^2 satisfy an equivalent relation

$$\begin{aligned} n^1 - n^2 &= 0, \\ &\quad mod(M) \\ n^1 + n^2 &= 0. \end{aligned} \tag{4.1}$$

Here n_e is the toroidal Fourier index of an equilibrium. By the introduction of this concept, the work in global mode analysis is greatly reduced since only $1 + [M/2]$ of perturbations need to be investigated. For the configuration considered here, $M = 10$. Then there are six mode families and N_f will be $0, 1, 2, 3, 4$, and 5.

4.2 CAS3D and the energy principle

In CAS3D, (ψ, θ, ζ) is used in a left-hand manner. Considering the toroidal field period being M, this triplets describes one field period of the toroidal domain $\mathcal{D} = [0,1] \times [[0,1] \times [0,1]$. The Jacobian is given by $\sqrt{g}^{-1} = \nabla\psi \cdot \nabla\theta \times \nabla\zeta$. In the Boozer coordinate system (ψ, θ, ζ) the field line is straight. The co- and contra- variant representation of $\boldsymbol{B}$ are

$$\begin{aligned} \boldsymbol{B} &= -\frac{F_T'}{\sqrt{g}}\boldsymbol{r}_{,\zeta} - \frac{F_P'}{\sqrt{g}}\boldsymbol{r}_{,\theta} \\ &= J\nabla\zeta + I\nabla\theta + \tilde{\beta}\nabla\psi \end{aligned} \tag{4.2}$$

where $F_T = F_T(\psi)$ is the toroidal flux and $I = I(\psi)$ the toroidal current. $F_P = F_P(\psi)$ is the poloidal flux and $J = J(\psi)$ the poloidal current in one field period. The primes represents differentiation with respect to flux surface label ψ. $\tilde{\beta} = \tilde{\beta}(\psi, \theta, \zeta)$ satisfies the following inhomogeneous magnetic differential equation

$$\sqrt{g}\boldsymbol{B} \cdot \nabla\tilde{\beta} = p'(\sqrt{g} - V') \tag{4.3}$$

which is related to $J_\parallel \propto \boldsymbol{J} \cdot \boldsymbol{B}$. $\int V'(\psi)d\psi$ gives the volume of one field period.

In (ψ, θ, ζ) coordinate system, the form (2.16) is expressed as

$$\delta W_F = \frac{1}{2}\int\int\int d^3r\{|\boldsymbol{C}|^2 - \mathcal{A}(\boldsymbol{\xi} \cdot \nabla s)^2 + \gamma p(\nabla \cdot \boldsymbol{\xi})^2\}. \tag{4.4}$$

Here

$$\boldsymbol{C} = \nabla \times (\boldsymbol{\xi} \times \boldsymbol{B}) + \frac{\boldsymbol{J} \times \nabla\psi}{|\nabla\psi|^2}\boldsymbol{\xi} \cdot \nabla\psi$$

and

$$\mathcal{A} = 2|\nabla\psi|^{-1}(\boldsymbol{J} \times \nabla\psi) \cdot (\boldsymbol{B} \cdot \nabla)\nabla\psi.$$

Compressive term enters the integral in two ways, one via the fluid compression, that is the $\nabla \cdot \boldsymbol{\xi}$ and thus proportional to γp, whereas the other is closely connected to the field line compression term, which equals the component of $\boldsymbol{C}$ parallel to the magnetic field within a factor of B. Both contributions have a stabilizing effect. Furthermore, $\boldsymbol{C}$ can be decomposed in $\frac{\nabla\psi}{|\nabla\psi|}$, $\frac{\nabla\psi \times \boldsymbol{B}}{|\nabla\psi|B}$, and $\frac{\boldsymbol{B}}{B}$ directions, i.e.,

$$\boldsymbol{C} = C^1\frac{\nabla\psi}{|\nabla\psi|} + C^2\frac{\nabla\psi \times \boldsymbol{B}}{|\nabla\psi|B} + C^3\frac{\boldsymbol{B}}{B} \tag{4.5}$$

with

$$
\begin{aligned}
C^1 &= \frac{1}{|\nabla\psi|}\boldsymbol{B}\cdot\boldsymbol{\xi}^{\psi},\\
C^2 &= -\frac{|\nabla\psi|}{B\sqrt{g}}\left(\sqrt{g}\boldsymbol{B}\cdot\nabla\eta - \iota F_T'^2\xi^{\psi} + \frac{\boldsymbol{J}\cdot\boldsymbol{B}}{|\nabla\psi|^2}\sqrt{g}\xi^{\psi} + \frac{\tilde{\sigma}B}{|\nabla\psi|^2}\sqrt{g}\boldsymbol{B}\cdot\nabla\xi^{\psi}\right),\\
C^3 &= \frac{1}{B\sqrt{g}}\left[I\eta_{,\zeta} - J\eta_{,\theta} + (F_T'J + F_P'I)\xi^{\psi}_{,\psi} + (IF_P'' + JF_T'')\xi^{\psi} - p'\sqrt{g}\xi^{\psi} + \tilde{\beta}\sqrt{g}\boldsymbol{B}\cdot\nabla\xi^{\psi}\right],\\
\sqrt{g}\mathcal{A} &= F_T''J' + F_P''I' - F_T''\tilde{\beta}_{,\zeta} - F_P''\tilde{\beta}_{,\theta} + \frac{|J|^2\sqrt{g}}{|\nabla\psi|^2} - p'\sqrt{g}_{,\psi} + \sqrt{g}\boldsymbol{B}\cdot\nabla\left(\frac{\sqrt{g}J^{\zeta}g^{\theta\psi} - \sqrt{g}J^{\theta}g^{\zeta\psi}}{|\nabla\psi|^2}\right).
\end{aligned}
\tag{4.6}
$$

(4.6) is called C-version in CAS3D. Although CAS3D applies the C-version to calculate the potential energy, the intuitive form called T-version in CAS3D can be easily constructed through some arrangements.

$$
\begin{aligned}
T^1 &= (C^1)^2 + (C^2 + \frac{\boldsymbol{J}\cdot\boldsymbol{B}}{B|\nabla\psi|}\xi^{\psi})^2 = B^{-2}|\boldsymbol{Q}\times\boldsymbol{B}|^2,\\
T^2 &= (C^3)^2 = B^{-2}|\boldsymbol{Q}\cdot\boldsymbol{B} - \boldsymbol{\xi}\cdot\nabla p|^2,\\
T^3 &= -\frac{F_T'^2}{\sqrt{g}}\tilde{D}\xi^{\psi 2} + \frac{\boldsymbol{J}\cdot\boldsymbol{B}}{B^2}\boldsymbol{B}\cdot\nabla(\xi^{\psi}\eta) = -2(\boldsymbol{\xi}\cdot\nabla p)(\boldsymbol{\kappa}\cdot\boldsymbol{\xi}_{\perp}^{*}),\\
T^4 &= \frac{\boldsymbol{J}\cdot\boldsymbol{B}}{B^2}(2\xi^{\psi}\boldsymbol{B}\cdot\nabla\eta - \frac{F_T'^2\iota'}{\sqrt{g}}\xi^{\psi 2}) - \frac{\boldsymbol{J}\cdot\boldsymbol{B}}{B^2}\boldsymbol{B}\cdot\nabla(\xi^{\psi}\eta),\\
&= \frac{\boldsymbol{J}\cdot\boldsymbol{B}}{B^2}\boldsymbol{Q}_{\perp}\cdot\boldsymbol{B}\times\boldsymbol{\xi},\\
&= J_{\parallel}(\boldsymbol{\xi}_{\perp}^{*}\times\boldsymbol{b})\cdot\boldsymbol{Q}_{\perp}.\\
\tilde{D} &= p'\left[\sqrt{g}p'/B^2 - \sqrt{g}_{,s} - B^{-2}(JF_P'' + IF_T'') + \sqrt{g}\boldsymbol{B}\cdot\nabla(\tilde{\beta}B^{-2})\right]/F_T'^2.
\end{aligned}
\tag{4.7}
$$

Then we have

$$
\delta W_F = \frac{1}{2}\int\int\int d^3r\{T^1 + T^2 + T^3 + T^4\} \tag{4.8}
$$

which corresponds to the intuitive form (2.10).

4.3 CAS3D2MN and phase factor transformation

Phase factor transformation was introduced in CAS3D2MN in order to save memory and flops. This technique was widely used since it is particularly efficient when a perturbation with large toroidal mode number ($n \gg M$) is studied.

Suppose M_P and N_P are poloidal and toroidal mode numbers of a chosen phase factor, the Fourier modes for a perturbation (m, n) was created by coupling the selected Fourier modes (m_e, n_e) from the equilibrium Fourier subset with the phase factor (M_P, N_P) in the following manner

$$\begin{aligned} & m = M_P + m_e, n = N_P + n_e, \\ & \text{or} \\ & m = M_P - m_e, n = N_P - n_e. \end{aligned} \tag{4.9}$$

If an equilibrium Fourier subset consists of M_{eq}^0 Fourier modes and M_{eq} $(M_{eq} \leq M_{eq}^0)$ Fourier modes are selected from this subset, the resultant number of Fourier modes for a perturbation is given by $M_{pt} = 2 \times M_{eq} - 1$. Here all of the equilibrium quantities were Fourier analyzed in both the poloidal and toroidal direction in Boozer coordinate systems. The two Mercier-unstable equilibria, $\mathcal{S}1$ and $\mathcal{S}2$, to be applied in this work are discussed in detail in Appendix A.

The Fourier mode of the perturbation (m, n) intersects ι profile in the way of $\frac{n}{m}$. Both the number of equilibrium Fourier modes and the phase factor (M_P, N_P) are carefully chosen in order to create an efficient resonant modes around (M_p, N_p). That the perturbation belongs to which mode family is determined by the toroidal index N_P of the phase factor. All of the perturbations to be considered in this work are given in Appendix B.

Due to the above considerations, the displacements are Fourier decomposed in the following manner.

$$\begin{aligned} \xi^{\psi} &= X^e \cos 2\pi(M_P\theta - \tfrac{N_P}{M}\zeta) + X^o \sin 2\pi(M_P\theta - \tfrac{N_P}{M}\zeta) \\ \eta &= Y^e \sin 2\pi(M_P\theta - \tfrac{N_P}{M}\zeta) + Y^o \cos 2\pi(M_P\theta - \tfrac{N_P}{M}\zeta) \end{aligned} \tag{4.10}$$

X^e and Y^e are even, and X^o and Y^o are odd functions with respect to variables (ψ, θ, ζ). They are Fourier decomposed in terms of the equilibrium Fourier modes (m_e, n_e).

$$\begin{aligned} X^e &\equiv \sum \hat{X}_i^e(\psi_N) \cos[m_e(i)\theta - n_e(i)\zeta] \\ Y^o &\equiv \sum \hat{Y}_i^o(\psi_N) \sin[m_e(i)\theta - n_e(i)\zeta] \\ & \quad i = 1, 2, \cdots, M_{eq} \end{aligned} \tag{4.11}$$

The energy principle is still expressed by (2.16). But the expression of coefficients in C-version and T-version should be changed correspondingly.

By means of Fourier decomposition in the angle-like coordinate θ and ζ, and a simple finite element method in the radial direction, the kinetic energy corresponds to a sym-

metric positive matrix and the potential corresponds to a symmetric band matrix. The energy principle is related to its eigenvalue problem, which is the topic of next chapter.

Chapter 5

Lanczos Eigensolver

5.1 Introduction

One of the important part in the global mode analysis is related to the solution of the following generalized eigenproblem

$$\boldsymbol{P}\boldsymbol{x} = \bar{\lambda}\boldsymbol{K}\boldsymbol{x} \tag{5.1}$$

where $\boldsymbol{P}$ and $\boldsymbol{K}$, arising from Ritz-Galerkin methods, corresponds to potential and kinetic energy, respectively. Both of them are symmetric matrices. Furthermore, $\boldsymbol{K}$ is positive definite. By non-physical normalization, problem (5.1) can be converted into

$$\boldsymbol{A}\boldsymbol{x} = \lambda\boldsymbol{x}. \tag{5.2}$$

In this work, $\boldsymbol{A}$ is a large but sparse, real symmetric matrix with order n and half bandwidth b, $b \ll n$. In this chapter, we use upper-case bold letters to denote the matrices, and integer n their orders. The lower-case bold letters are still used to denote the vectors.

The set $(\lambda, \boldsymbol{x})$ is called the eigenelement of $\boldsymbol{A}$. Usually $\boldsymbol{A}$ is indefinite. In fusion research and here too, one is mainly interested in the negative end of spectrum, particularly the smallest one (λ_{min}). $\lambda_{min} < 0$ indicates that an equilibrium is unstable to a given perturbation. The perturbation is given by the corresponding eigenvector which can be an interchange or a ballooning mode in our case.

In CAS3D the following inverse iteration (see [29])

$$\begin{aligned} &\text{for} \quad k = 1, 2, \ldots \\ &\qquad \text{Solve } (\boldsymbol{A} - ewshift\ \boldsymbol{I})\boldsymbol{z}^k = \boldsymbol{x}^{k-1} \\ &\qquad \boldsymbol{x}^k = \boldsymbol{z}^k / \|\boldsymbol{z}^k\|_2 \\ &\qquad \lambda^k = \boldsymbol{x}^{k^T} \boldsymbol{A} \boldsymbol{x}^k \\ &\text{end} \end{aligned} \tag{5.3}$$

has been applied to calculate the smallest eigenvalue and its corresponding eigenvector, in which the spectral shift $ewshift$ in Eq.(5.3) is given by the Givens QR iteration algorithm (for CAS3D):

$$ewshift = \lambda_{min} \text{ (from Givens QR iteration)} \tag{5.4}$$

But this kind of matrix transformation is not suitable for eigenproblems of very large but sparse matrices in the following three aspects:

- the given matrix will be modified during the computation and fill-ins are inevitably brought in. So the sparsity will be destroyed,
- $O(n^3)$ flops are needed to run because of application of the orthogonal similarity transformation,
- $O(n^2)$ words must be specified for storage.

which greatly limit the size of problems we can handle. As well known, Stability analysis in 3-D systems is time and memory consuming. Specially storage requirement is much more stringent. For example for a work set with 1840 radial meshes and 793 Fourier modes, a minimum of 16GB is necessary before the solution of eigenproblem starts. In such a case, the application of orthogonal similarity transformation, such as EISPACK [37] or LAPACK [38] routines, will obviously fail. Whether the flops and storage can be controlled or not becomes critical in this work. Therefore, it is natural to consider Lanczos recursion with no re-orthogonalization which supersedes the above softwares:

- The given matrix $\boldsymbol{A}$ enters the recursion only through the matrix-vector multiplies $\boldsymbol{Aq}$ and its sparsity will not be modified during the calculation,
- For a sparse matrix, flops required to generate the Lanczos matrices using the recursion with no re-orthogonalization is $O(n^2)$, and storage requirements is just $O(n)$.

The increase in memory can be controlled naturally in a neglected order. It is just the above advantage that makes the Lanczos algorithm with no re-orthogonalization be particularly suitable for and extensively applied.

In ideal MHD range, the eigenvalues are real. They can be separated into positive and negative parts. The positive one refer to three branches of waves: the fast magnetosonic waves, the shear Alfvén waves, and the slow magnetosonic waves, respectively. With the application of the incompressibility condition $\nabla \cdot \boldsymbol{\xi} = 0$, the slow branch is dropped. By the normalization of kinetic energy in (5.2), the resultant spectrum has quite different orders of magnitude. The negative part, what we are interested in, remains very small (usually $\sim 10^{-3}$). But the positive part is enlarged considerably (as large as $\sim 10^{6}$). One example is given in Figure 5.1 and Figure 5.2. The overall spectrum, given in Figure 5.1, is calculated by LAPACK, where the number of the Fourier modes M_{pt} and the number of the radial meshes N_S are 35 and 120, respectively. The eigenvalues have been scaled by the function $\sinh^{-1}(\alpha x)$ with $\alpha = 10^5$ in Figure 5.2. Obviously, it is the large positive eigenvalues are dominant rather than the small negative ones. To compute the smallest one which lies in the negative part, application of a shift and invert strategy is preferred to make the negative part dominant in the spectrum. A shift is chosen to transform the matrix into a positive definite one in order to construct an efficient Cholesky factorization in invert Lanczos recursion. Therefore, memory can be expected not to increase, but convergence be sped up.

5.2 Lanczos Algorithm with no re-orthogonalization

The Lanczos recursion is a method for replacing the eigenproblem of a given symmetric matrix $\boldsymbol{A}$ by eigenproblems on a series of much simpler Lanczos tridiagonal matrices, given by $\boldsymbol{T}_m$. Subsets of eigenvalues of these tridiagonal matrices are selected as approximate eigenvalues of the original matrix $\boldsymbol{A}$. Their approximation accuracy depends on the magnitude of the last component of the corresponding eigenvectors of $\boldsymbol{T}_m$ as long as the eigenvalues being considered are isolated eigenvalues of the associated Lanczos matrix.

For the considered real, symmetric matrix $\boldsymbol{A}$ with order n, the Lanczos matrices can be given by the following recursion, which is highly recommended by Paige [35] due to finite computer precision. Define $\beta_1 \equiv 0$ and $\boldsymbol{q}_0 \equiv 0$, and choose $\boldsymbol{q}_1$ as a random vector

with $\|\boldsymbol{q}_1\| = 1$. Then for $i = 1, 2, \ldots, m$ define Lanczos vectors $\boldsymbol{q}_i$ and scalars α_i and β_{i+1} by

$$\begin{aligned} \boldsymbol{q} &= \boldsymbol{A}\boldsymbol{q}_i - \beta_i \boldsymbol{q}_{i-1} \\ \alpha_i &= \boldsymbol{q}_i^T \boldsymbol{q} \\ \boldsymbol{q} &= \boldsymbol{q} - \alpha_i \boldsymbol{q}_i \\ \beta_{i+1} &= \|\boldsymbol{q}\| \\ \boldsymbol{q}_{i+1} &= \boldsymbol{q}/\beta_{i+1} \end{aligned} \tag{5.5}$$

The $\alpha_i \boldsymbol{q}_i$ and the $\beta_i \boldsymbol{q}_{i-1}$ are, respectively, projection of $\boldsymbol{A}\boldsymbol{q}_i$ onto $\boldsymbol{q}_i$ and $\boldsymbol{q}_{i-1}$.

For each m, the corresponding Lanczos matrix $\boldsymbol{T}_m$ is defined as a real symmetric and tridiagonal matrix

$$\boldsymbol{T}_m = \begin{bmatrix} \alpha_1 & \beta_2 & & & & \\ \beta_2 & \alpha_2 & \cdot & & & \\ & \cdot & \cdot & \cdot & & \\ & & \cdot & \cdot & \cdot & \\ & & & \cdot & \alpha_{m-1} & \beta_m \\ & & & & \beta_m & \alpha_m \end{bmatrix}. \tag{5.6}$$

In compact form

$$\boldsymbol{A}\boldsymbol{Q}_m = \boldsymbol{Q}_m \boldsymbol{T}_m + \beta_{m+1} \boldsymbol{q}_{m+1} \boldsymbol{e}_m^T \tag{5.7}$$

where $\boldsymbol{Q}_m = [\boldsymbol{q}_1, \boldsymbol{q}_2, \ldots, \boldsymbol{q}_m]$ and $\boldsymbol{e}_m^T = (0, \ldots, 0, 1)$. Thus, given a real symmetric matrix $\boldsymbol{A}$ and a starting vector $\boldsymbol{q}_1$, the Lanczos recursion generates a family of real symmetric tridiagonal matrices related to $\boldsymbol{A}$ and to $\boldsymbol{q}_1$ through (5.5). Problem (5.2) is equivalent to solve

$$\boldsymbol{T}_m \boldsymbol{y} = \mu \boldsymbol{y} \tag{5.8}$$

where the set $(\mu, \boldsymbol{y})$ corresponds to the eigenpair of the Lanczos matrix $\boldsymbol{T}_m$. Clearly only

- memory for generating the matrix-vector multiplies $\boldsymbol{A}\boldsymbol{q}_i$
- memory for only two Lanczos vectors $\boldsymbol{q}_i$ and $\boldsymbol{q}_{i-1}$ of length n
- space for the tridiagonal Lanczos matrix $\boldsymbol{T}_m(\alpha_i, \beta_{i+1})$ itself

should be specified, since $\boldsymbol{q}_{i-1}$ can be overwritten by $\boldsymbol{q}$. Usually no extra memory will be needed in $\boldsymbol{A}\boldsymbol{q}_i$ calculation except space for $\boldsymbol{A}$ itself. The increase in memory results from 4 vectors: $\boldsymbol{q}_i$, $\boldsymbol{q}_{i-1}$, $\boldsymbol{\alpha}$, and $\boldsymbol{\beta}$. $\boldsymbol{\alpha} = \{\alpha_i\}, \boldsymbol{\beta} = \{\beta_{i+1}\}$. This will be a neglected quantity when m is much smaller than n. Arithmetic operations mainly come from calculating $\boldsymbol{A}\boldsymbol{q}_i$.

Since the ratio of zero entries to non-zero entries is smaller than $(2b+1)/n$ (at present $\sim O(10^{-2})$) for the matrices resulting from the present calculations, these matrices are very sparse. Therefore, the operation counts just grow as the square of n.

For any real symmetric matrix $\boldsymbol{A}$, our implementation of the above recursion is based upon the following fact called Lanczos Phenomenon:

When m becomes large enough, every distinct eigenvalue of $\boldsymbol{A}$ can be approximated by an eigenvalue of $\boldsymbol{T}_m$.

and the identification test:

the convergence of the eigenvalues of the Lanczos matrices as the size m is increased.

We choose the necessary number of Lanczos steps m automatically. Suppose μ' and μ'' are the smallest eigenvalues of successive Lanczos matrices $\boldsymbol{T}_{m'}$ and $\boldsymbol{T}_{m''}$ ($m' \neq m''$). If the difference $|\mu' - \mu''|$ between μ' and μ'' is smaller than the given convergence tolerance, we then set $\mu = \mu' = \mu'', m = m''$ and compute the magnitude of mth component $\boldsymbol{y}(m)$ of μ's eigenvector $\boldsymbol{y}$ (of $\boldsymbol{T}_m$). This is according to Paige [1980] [31]).

For a given m and for any isolated eigenvalue μ of the Lanczos matrix $\boldsymbol{T}_m$, there exists an eigenvalue λ of $\boldsymbol{A}$ such that

$$|\lambda - \mu| \leq 2.5[|\beta_{m+1}\boldsymbol{y}(m)|(1+2\epsilon_0) + 2\epsilon_1\|\boldsymbol{A}\|m^{1/2}] \tag{5.9}$$

where ϵ_0 and ϵ_1 are related to machine precision ϵ, and satisfy $4m(3\epsilon_0 + \epsilon_1) \ll 1$. The term $\epsilon_\mu \equiv |\beta_{m+1}\boldsymbol{y}(m)|$ plays the key role in estimating the convergence of computed eigenvalue μ. That is, if the last component $\boldsymbol{y}(m)$ is very small, eigenvalue μ will be a good approximation of eigenvalue λ of $\boldsymbol{A}$.

We use inverse iteration (5.3) to compute $\boldsymbol{y}(m)$ of corresponding Lanczos matrix $\boldsymbol{T}_m$. In our experiences, μ is as accurate as what have been computed by EISPACK

or LAPACK subroutine (Givens QR itetation algorithm). At each iteration only the incremental scalars α_i, β_{i+1} have to be generated. The Lanczos recursion with no re-orthogonalization can be given as:

- step 1. Specify an initial Lanczos step $m \ll n$, increase step $k > 0$, and convergence tolerances $CONTOL1$ and $CONTOL2$.
- step 2. Putting $m = m + k$, generate the real symmetric tridiagonal matrix $\boldsymbol{T}_m$ by recursion (5.5) and keep $\boldsymbol{q}_m$ and $\boldsymbol{q}_{m+1}$ for next iteration.
- step 3. Compute the smallest eigenvalue μ of the Lanczos matrix $\boldsymbol{T}_m$.
- step 4. Select μ which appears in successive $\boldsymbol{T}_m$ by $CONTOL1$ and compute its convergence by inverse iteration method (5.3).
- step 5. If convergence is observed by $CONTOL2$, accept μ as the approximation of λ_{min} of the given matrix $\boldsymbol{A}$ and terminate. Otherwise, go to step 2 to enlarge $\boldsymbol{T}_m$.

In the present work, the matrix $\boldsymbol{A}$ is indefinite. Its spectrum has quite different orders of magnitude corresponding to positive or negative part. As shown in Figure 5.1, $\boldsymbol{A}$ is rich in positive eigenvalues with magnitude as large as $\sim 10^6$. On the other end of spectrum, i.e., the negative part what we are interested in, the number is few and their magnitudes are as small as $\sim 10^{-3}$. They are undominant in the spectrum. Moreover, these matrices have gap stiffness behaving like what Cullum and Willoughby called the worst case [32]. For these reasons, the smallest eigenvalue converges very slowly by recursion (5.5). But this process can be accelerated significantly by shift-and-invert strategy which is the topic of the next section.

5.3 Shift-and-invert Lanczos algorithm

Since the smallest eigenvalue lies in the negative end of spectrum which is dominated by positive part, it will be preferred to apply the Lanczos recursion (5.5) to $\boldsymbol{A}^{-1}$. With this transformation, the desired part of spectrum becomes dominant. The Lanczos recursion is expected to be accelerated in the sense that the size of the Lanczos matrix required to obtain the smallest eigenvalue is much smaller.

Similarly to section 5.3, main arithmetic operations come from $\boldsymbol{A}^{-1}\boldsymbol{q}$. The efficient calculation of $\boldsymbol{A}^{-1}\boldsymbol{q}$ becomes important concerning flops and storage. In order to save flops and storage, an $SHIFT$ is carefully chosen to shift $\boldsymbol{A}$ to be positive definite

$$\boldsymbol{C} = (\boldsymbol{A} + SHIFT\ \boldsymbol{I})/S0 \tag{5.10}$$

where $S0$ is used to scale the given matrix $\boldsymbol{A}$ in order to avoid overflow. Sparsity of $\boldsymbol{C}$ is the same as that of $\boldsymbol{A}$. The calculation of $\boldsymbol{A}^{-1}\boldsymbol{q}$ is transformed to the calculation of $\boldsymbol{C}^{-1}\boldsymbol{q}$ which can be efficiently done by sparse Cholesky factorization

$$\boldsymbol{C} = \boldsymbol{U}^T\boldsymbol{U} \tag{5.11}$$

Here $\boldsymbol{C}$ is overwritten with upper triangular matrix $\boldsymbol{U}$ which has the same upper bandwidth as $\boldsymbol{C}$. Consequently, no extra memory will be increased compared with $\boldsymbol{Aq}$ multiplies. Moreover, flops is kept to be a minimum. Then for any given vector $\boldsymbol{q}$, the vector $\boldsymbol{p} = \boldsymbol{C}^{-1}\boldsymbol{q}$ can be evaluated efficiently by solving sequentially two triangular systems of equations

$$\boldsymbol{U}^T\boldsymbol{U}\boldsymbol{p} = \boldsymbol{q}: \qquad \boldsymbol{U}^T\bar{\boldsymbol{p}} = \boldsymbol{q}, \qquad \boldsymbol{U}\boldsymbol{p} = \bar{\boldsymbol{p}} \tag{5.12}$$

The shift-and-invert Lanczos algorithm can be formed as follows:

$$\begin{aligned}
&\boldsymbol{C} = \boldsymbol{U}^T\boldsymbol{U}(\text{ Cholesky factorization of } \boldsymbol{C})\\
&\boldsymbol{p} = \boldsymbol{q}_i\\
&\boldsymbol{p} = \boldsymbol{U}^{-T}\boldsymbol{p}\\
&\boldsymbol{p} = \boldsymbol{U}^{-1}\boldsymbol{p}\\
&\boldsymbol{q} = \boldsymbol{p} - \beta_i\boldsymbol{q}_{i-1}\\
&\alpha_i = \boldsymbol{q}_i^T\boldsymbol{q}\\
&\boldsymbol{q} = \boldsymbol{q} - \alpha_i\boldsymbol{q}_i\\
&\beta_{i+1} = \|\boldsymbol{q}\|\\
&\boldsymbol{q}_{i+1} = \boldsymbol{q}/\beta_{i+1}
\end{aligned} \tag{5.13}$$

Compared with (5.5), only space for one more vector $\boldsymbol{p}$ with length n, 5 vectors in total, is increased in the above recursion. Although each step using $\boldsymbol{C}^{-1}$ is more expensive than a corresponding step using $\boldsymbol{A}$, the large decrease in the number of Lanczos steps required and the fact that the factors are also sparse, yield overall large gains in flops and storage. CAS3D2MN with (5.13) is denoted by CAS3D2MNv1 [39] for convenience.

Suppose $(\mu, \boldsymbol{y})$ is an eigenpair of $\boldsymbol{T}_m$, i.e. $\boldsymbol{T}_m \boldsymbol{y} = \mu \boldsymbol{y}$, then

$$\|[(\boldsymbol{A} + SHIFT\ \boldsymbol{I})/S0]^{-1} \boldsymbol{Q}_m \boldsymbol{y} - \mu \boldsymbol{Q}_m \boldsymbol{y}\| = |\beta_{m+1} \boldsymbol{y}(m)| \tag{5.14}$$

and the eigenvalue λ of $\boldsymbol{A}$ can be evaluated as

$$\boldsymbol{A}\boldsymbol{x} = \lambda \boldsymbol{x} \Longleftrightarrow [(\boldsymbol{A} + SHIFT\ \boldsymbol{I})/S0]^{-1} \boldsymbol{x} = [(\lambda + SHIFT)/S0]^{-1} \boldsymbol{x} \tag{5.15}$$

so

$$(\lambda + SHIFT)/S0 = \mu^{-1} \tag{5.16}$$

that is

$$\lambda = S0/\mu - SHIFT \tag{5.17}$$

5.4 Efficiency of the Lanczos eigensolver

The original Lanczos recursion given by (5.5) and the shift-and-invert Lanczos recursion given by (5.13) both have been applied to solve the eigenvalue problem resulting from the ideal MHD stability analysis in a 3-D MHD equilibrium. In order to clarify the properties of the matrix in (5.2), we begin with the definition of gap stiffness and matrix stiffness [32]. These quantities show how the convergence of Lanczos recursion are affected by the spectrum distribution.

Definition. For a real symmetric matrix $\boldsymbol{A}$ with distinct eigenvalues $\lambda_{k_1} > \lambda_{k_2} > \cdots > \lambda_{k_s}$, define the minimal gap g_j for each eigenvalue $\lambda_{k_j}, 1 \leq j \leq s$ as follows:

$$\begin{aligned} g_1 &\equiv (\lambda_{k_1} - \lambda_{k_2}) \\ g_s &\equiv (\lambda_{k_{s-1}} - \lambda_{k_s}) \\ g_j &\equiv min[\lambda_{k_j} - \lambda_{k_{j+1}}, \lambda_{k_{j-1}} - \lambda_{k_j}],\ \text{for } j = 2, \ldots s-1 \end{aligned} \tag{5.18}$$

The overall gap stiffness is defined by

$$S_g(\boldsymbol{A}) \equiv \max_j g_j / \min_j g_j \tag{5.19}$$

and the matrix stiffness by

$$S(\boldsymbol{A}) \equiv \max_j |\lambda_j| / \min_j |\lambda_j| \tag{5.20}$$

As the gap stiffness increases, the degree of difficulty in computing the desired part of spectrum with small gaps increases. The gap stiffness corresponding to Figure 5.2 is

shown in Figure 5.3. From these figures we can see that the type of matrix in CAS3D2MN has very bad stiffness. Its eigenvalues range from 10^6 to 10^{-3} orders with positive ones dominant. The smallest eigenvalue, what we are interested in, lies in the negative part of spectrum. The negative eigenvalues are small in number as well as quantity. It is undominant. This is the reason why Lanczos recursion given by Eq.(5.5) does not work well. In the parameters used in Figure 5.1 $\sim$ 5.3, it has taken us as much as $2n$ steps to obtain the negative eigenvalues and $11n$ steps to obtain the smallest one, where n is the matrix order. Here $\lambda_{min} = -2.14952 \times 10^{-3}$, $\lambda_{max} = 6.47634 \times 10^6$, $S(\boldsymbol{A}) = 3.01292 \times 10^9$, $S_g(\boldsymbol{A}) = 8.70109 \times 10^7$, and $n = 8435$. Recursion (5.5) is sped up significantly by introducing a shift-and-invert strategy given in (5.13). In the same case, it takes only 20 steps to get λ_{min} although $S(\boldsymbol{A})$ is in $O(10^{13})$ order at this time. Thus, it is the location of desired eigenvalues in the spectrum, the local separation of eigenvalues, and primally the overall gap stiffness of matrix $\boldsymbol{A}$ which determine the convergence of the desired eigenvalues as the size m of $\boldsymbol{T}_m$ is increased.

As what we expected, an increase in memory is kept to be 5 vectors in (5.13), leading to a neglected quantity in a work set.

Table 5.1 gives the increase in memory in a work set from matrix creation (memory1) to eigenvalue calculation by (5.13) (memory2). It is shown that only a small quantity of memory, at most 1.5%, is increased. From this aspect of view, (5.13) is also efficient.

Table 5.1 increase in memory by (5.13)

Order (n)	bandwidth (b)	memory1 (bytes)	memory2 (bytes)	increase rate
72631	453	411811880	417842920	1.5%
490091	1113	4718272264	4756377880	0.8%
738955	1473	9116965656	9175310824	0.6%
956175	2013	15807398584	15887217912	0.5%

The comparison of the shift-and-invert Lanczos recursion (5.13) with EISPACK and LAPACK routines is given in Table 5.2 for calculating the smallest eigenvalue, which is negative here. Only the number of Fourier modes $M_{\mu t}$ and the number of the radial meshes N_S are changed, as shown in the first column in Table 1, which leads to the variation of the matrix order n and half bandwidth b. The $SHIFT$ in Eq.(5.10) is chosen to be 0.01. From the second column to the sixth column, the smallest eigenvalue, matrix order, memory[1], CPU time, and speedup rate of recursion (5.13) compared to EISPACK are

[1]The storage requirement is mainly determined by matrix order and bandwidth. Storage size for

shown. The name of algorithms is marked at the right end of the Table, for which the data in the same row have been obtained. From the table we can see that LAPACK subroutine has relatively smaller storage requirement but more CPU time compared with EISPACK. For (5.13), usually $15 \sim 20$ Lanczos steps are enough. That is, the extreme eigenvalue of Lanczos tridiagonal matrix $\boldsymbol{T}_m$ with order $15 \sim 20$ is a good approximation of $\boldsymbol{A}$'s smallest eigenvalue. Its storage requirement is much smaller compared with EISPACK and LAPACK, and $50 \sim 100$ times of speedup are achieved easily. In the final part of the table where N_S is increased to 300 and M_{pl} to 201, EISPACK and LAPACK both have failed to calculate λ_{min} in 10 hours, but for recursion (5.13) only 903sec are sufficient. From this point, the shift-and-invert strategy is a quite efficient tool for the solution of very large scale eigenproblem.

Table 5.2 $(M_P, N_P) = (8, -5), SHIFT = 0.01$

(N_S, M_{pl})	$\lambda_{min}(\times 10^{-3})$	Order	memory (MB)	CPU(sec)	S_p	Algorithm
(120, 35)	-2.14952	8435	35	170.38		EISPACK
		8435	18	367.39		LAPACK
		20	11	3.14	54.25	(5.13)
(180, 35)	-1.97229	12635	94	374.52		EISPACK
		12635	25	585.76		LAPACK
		30	15	5.26	71.20	(5.13)
(180, 59)	-2.29349	21299	81	2068.69		EISPACK
		21299	63	2688.61		LAPACK
		20	34	16.75	123.50	(5.13)
(300, 201)	-2.90651	120801	-	-		EISPACK
		120801	-	-		LAPACK
		20	567	902.52	-	(5.13)

- means CPU times exceeds 10 hours. Note that the data given in Table 5.2 are obtained on the general SX-4 with peak performance 2GF in the National Institute for Fusion Science.

EISPACK is an approximate value but there is only a little difference.

5.5 Inverse iteration

Here we briefly explain the properties of inverse iteration given by (5.3). Inverse iteration is an essential concept and also an efficient algorithm in the solution of eigenproblems. Usually it is applied with an application of spectral shift. If the spectral shift is given to be very close to a desired eigenvalue and a starting vector is generated to have dominant component along the corresponding eigenvector, the iteration will converge very quickly. Shown in the following table is an example of the convergence rate of (5.3) in the process of global mode analysis.

Table 5.3 The effect of initial vector

ewshift = -1.19357454E-02

iteration steps	λ^k	x_0	$\tilde{x}_0$
0	λ^0	1.98488076E-01	-1.19357391E-02
1	λ^1	3.59349633E-03	-1.19357428E-02
2	λ^2	7.04385068E-04	-1.19357428E-02
3	λ^3	-3.80683468E-04	
4	λ^4	-1.30524650E-03	
5	λ^5	-2.52578259E-03	
6	λ^6	-3.90999787E-03	
7	λ^7	-4.98182517E-03	
8	λ^8	-5.58911537E-03	
9	λ^9	-5.89530187E-03	
10	λ^{10}	-6.05553769E-03	

The result in the first column is obtained by the application of a constant starting vector

$$\boldsymbol{x}_0 = \{x_{0,i} : x_{0,i} = \frac{1}{n}, i = 1, \cdots, n\} \tag{5.21}$$

where $n = 793629$ is the order of given matrix. There is a stationary point at $-8.19558928E-03$ which corresponds to the third smallest eigenvalue λ_3. The second and first ones are $\lambda_2 = -1.05485652E-02$ and $\lambda_1 = -1.11935745E-02$, respectively, which are relatively far from λ_3. Clearly $\boldsymbol{x}_0$ is a bad choice of starting vector, leading to a slow convergence to the stationary point λ_3, and be difficult to converge to λ_1. In contrast, another starting vector, generated by

$$\tilde{\boldsymbol{x}}_0 = random(n) \tag{5.22}$$

which is uniformally distributed in $(-1, 1)$ region, works. It needs only 3 times to converge to λ_1. This results from the characteristics of pressure-driven modes, which will become clear in the next chapter.

The most safety way is to generate a starting vector randomly and then discard undesired eigenvector components from this starting vector using some filtering techniques.

In fact, equally important is how to give a spectral shift to let it approximate our desired eigenvalue. Suppose $ewshift$ is a good approximation to the smallest eigenvalue of $\boldsymbol{A}$, $\bar{\lambda}_{min}$, namely, $\exists\ 0 < \delta < 1 \ni |ewshift - \bar{\lambda}_{min}| < \delta$, then the sequence λ^k generated by the recursion (5.3) has following properties

- if $\lim_{k\to\infty} \lambda^k = \bar{\lambda}_{min}$, then

$$\frac{\lambda^{k+1} - \bar{\lambda}_{min}}{\lambda^k - \bar{\lambda}_{min}} \to \gamma$$

  with γ constant.

- When $\boldsymbol{A}$ is normal,

$$\frac{\lambda^{k+1} - \bar{\lambda}_{min}}{(\lambda^k - \bar{\lambda}_{min})^2} \to \gamma$$

  with γ constant.

Note that a matrix is said to be normal if it can commute with its conjugate transpose $\boldsymbol{A}^H$. $\bar{\lambda}_{min}$ differs from λ_{min} in (5.4) which is approximately computed by Givens QR iteration algorithm.

Chapter 6

Global Mode Analysis

6.1 Introduction

In this chapter we investigate the global properties of pressure-driven modes in the $L = 2/M = 10$ heliotron system with an essentially axisymmetric, and inherently large Shafranov shift, and prove the conjectures [12] reviewed in chapter 3. with the application of CAS3D2MNv1.

Since the properties of the finite-β equilibria are basically understood as a modification of the vacuum configuration by the large Shafranov shift, the local and global properties of these equilibria change considerably according to the magnitude of Shafranov shift. Associated with the properties of pressure-driven modes discussed in chapter 1 and 3, some local and global properties of equilibria are investigated. As global properties, the following surface quantities are ermined.

- the global rotational transform ι,
- the global magnetic shear $s \equiv \dfrac{2\psi}{\iota}\dfrac{d\iota}{d\psi}$,
- the quantity V'' that measures the averaged magnetic well

  [here a prime denotes the derivative $' \equiv d/d\psi_N$, and $V'' < 0$ means an average favorable magnetic well],
- the Mercier criterion parameter D_M [$D_M > 0$ means Mercier stable] (see (3.10)),

where ψ is the label of the flux surface and is defined as $\psi = \Phi_t/(2\pi)$ with Φ_t the toroidal flux inside a flux surface, and $\psi_N = \psi/\psi_{edge}$ is the normalized toroidal flux. On the other hand, as local quantities, the following local quantities are ermined.

- the local magnetic shear $\hat{s}$ (see (3.17)),
- the normal magnetic curvature κ^n (see (3.20)).

Pressure-driven modes with long wavelengths - e.g., long wavelength interchange modes - experience the magnetic curvature with its local variation averaged out. As the wave length becomes shorter, pressure-driven modes begin to feel the local structure of the magnetic curvature. Since the 3-D equilibria considered here have toroidal field period M, the local magnetic curvature due to helicity also has the toroidal period M. Therefore, we investigate the inherent properties of pressure-driven modes by changing the relative magnitude of their typical toroidal mode number n, as compared to the toroidal period of the local magnetic curvature due to helicity, M: namely, $n < M$, $n \sim M$, and $n \gg M$.

The present chapter is organized as follows. In section 2, the local and global characteristics are given for the Mercier-unstable in the $L = 2/M = 10$ planar axis heliotron system. The Mercier-unstable equilibria are categorized into two types, namely, toroidicity-dominant Mercier-unstable equilibria and helicity-dominant Mercier-unstable equilibria, according to the degree of reduction of the local magnetic shear on the outer side of torus by Shafranov shift. The global mode analysis is described in section 3 for toroidicity-dominant Mercier-unstable equilibria; in section 4 for helicity-dominant Mercier-unstable equilibria.

6.2 Characteristics of MHD equilibria

As the vacuum configuration, we use an $L = 2/M = 10$ planar axis heliotron configuration like that for the Large Helical Devices (LHD)[24]. This configuration is exactly the same as that used in Refs. [11] and [12].

The properties of the vacuum configuration can be understood as a straight helical configuration toroidally bended. Since the aspect ratio is relatively large: $R_0/a = 7 \sim 8$ [here R_0 and a are the major and minor radii, respectively], the global and local properties of the vacuum configuration are mainly determined by helicity of helical coils. As global

properties, surface quantities are drawn in Figure 6.1 (dash-dotted line) as functions of the normalized radial coordinate $r_N \equiv \sqrt{\psi_N}$. The stellarator-like global magnetic shear s and the average unfavorable magnetic curvature (magnetic hill): $V'' > 0$ are shown in the whole plasma region, just as in a corresponding straight helical system.

As well as the global properties, the local quantities associated with high-mode-number ballooning modes analysis (local mode analysis) are strongly related to helicity in the vacuum configuration. Shown in Figure 6.2 are their equally spaced (ψ, ζ) meshes and the corresponding contours for the local magnetic shear $\hat{s}$ and for the normal magnetic curvature multiplied by the Jacobian $\sqrt{g}\kappa^n$; these are shown both on vertically and horizontally elongated poloidal cross sections for the vacuum configuration. It is shown in Figure 6.2 that the local properties of the local magnetic shear and the normal magnetic curvature mainly come from helicity in the vacuum configuration. The effect of toroidicity is more apparent in the normal magnetic curvature $\sqrt{g}\kappa^n$ than in local magnetic shear $\hat{s}$. On horizontally elongated poloidal cross section, the locally unfavorable magnetic curvature due to helicity is superposed on that due to toroidicity on the outer side of torus, and hence the normal magnetic curvature on the outer side of torus is more unfavorable than that on the inner side of torus. In contrast, on vertically elongated poloidal cross section, the locally favorable magnetic curvature due to helicity cancels the locally unfavorable magnetic curvature due to toroidicity, leading to locally favorable magnetic curvature even on the outer side of torus.

An MHD equilibrium can be completely determined by specifying pressure profile, current condition, and boundary condition. Here the 3-D finite β equilibria are calculated with the Variational Moment Equilibrium Code (VMEC) under the condition of a fixed boundary. The boundary is determined from the outermost flux surface of the vacuum magnetic field, which has nearly concentric circular magnetic flux surfaces when averaged in the toroidal direction.

The properties of the finite-β equilibria are understood as a modification of the vacuum configuration by an essentially axisymmetric and inherently large Shafranov shift. The essential structure of the Shafranov shift is understood by a model equation. With the use of the stellarator expansion under high-β ordering, namely

$$\beta \sim O(\epsilon_t), \epsilon_t = a/R_0. \tag{6.1}$$

The Shafranov shift Δ can be expressed as [11]

$$\frac{d\Delta}{dr} = \frac{R_0}{4\iota^2}\frac{d\beta}{dr} \sim O(1) \tag{6.2}$$

where r is the radial coordinate, $\beta = 2p_0/B_0^2$, and B_0 is the magnetic field strength at $R = R_0$.

From equation (6.2), it is found that peaked pressure profile with net toroidal toroidal current or peaked pressure profile decreasing the rotational transform ι create a large Shafranov shift. In contrast, for the same beta value β_0 at the magnetic axis, broad pressure profiles with no net toroidal current or broad pressure profiles with a net toroidal current decreasing the rotational transform ι create a small Shafranov shift. Since the properties of the vacuum configuration is mainly determined by helicity as shown in Figure 6.2 and since the Shafranov shift is essentially axisymmetric, the larger the Shafranov shift becomes, the more significant the effects due to toroidicity become, compared with helicity. Such a Shafranov shift changes the local and global properties of equilibria, namely,

- the reduction of the local magnetic shear on the outer side of torus (local property),
- the formation of the average favorable normal magnetic curvature near the magnetic axis (global property).

The former is unfavorable to ballooning modes through the reduction of the stabilizing effects and the latter is favorable to interchange modes through the Mercier criterion D_M. According to the reduction of the local magnetic shear and the formation magnitude of the average favorable normal magnetic curvature brought by the Shafranov shift, the 3-D MHD Mercier-unstable equilibria can be categorized into toroidicity-dominant Mercier-unstable equilibria and helicity-dominant Mercier-unstable equilibria. The toroidicity-dominant Mercier-unstable equilibria have a relatively large Shafranov shift. These equilibria are characterized by the local properties that the (integrated) local magnetic shear is much reduced by the Shafranov shift, leading to the situation that ballooning modes would be easy to destabilize. In contrast, the helicity-dominant Mercier-unstable equilibria have a relatively small Shafranov shift. These equilibria are characterized by local properties that the (integrated) local magnetic shear is less reduced by the Shafranov shift, leading to ballooning modes to be hard to destabilize.

On the basis of the above considerations, the following two types of Mercier-unstable equilibria are introduced in order to examine the competitive or synergetic effects of

toroidicity and helicity on the pressure-driven modes. One is toroidicity-dominant Mercier-unstable equilibria, and the other is helicity-dominant Mercier-unstable equilibria. The toroidicity-dominant Mercier-unstable equilibrium is created with a peaked pressure profile

$$p(\psi_N) = p_0(1 - \psi_N)^2 \tag{6.3}$$

under the flux conserving condition, i.e., with a specified profile of rotational transform ι. $\beta_0 = 5.9\%$. The helicity-dominant Mercier-unstable equilibrium is created with a broad pressure profile

$$p(\psi_N) = p_0(1 - \psi_N^2)^2 \tag{6.4}$$

under the currentless condition. $\beta_0 = 4.0\%$. Note that this equilibrium is exactly the same as used in reference [12].

Surface quantities are shown in Figure 6.1 in functions of r_N: (a) for toroidicity-dominant Mercier-unstable equilibrium, (b) for helicity-dominant Mercier-unstable equilibrium. Shown in Figure 6.1(a) and (b) in dash lines are two auxiliary equilibria with respect to the study of the corresponding of helicity-dominant and toroidicity-dominant Mercier-unstable equilibria. Clearly the helicity-dominant Mercier-unstable equilibrium is more Mercier unstable than the toroidicity-dominant one.

Shown in Figures 6.3 and 6.4 are the same local quantities (given in Figure 6.2 for vacuum) for the toroidicity-dominant Mercier-unstable equilibrium and helicity-dominant Mercier-unstable equilibrium. The effect of the introduction of the large Shafranov shift can be clearly understood with a comparison of Figure 6.2 (vacuum) with Figures 6.3 $\sim$ 6.4 (finite-β equilibria). A comparison of Figures 6.2(b), 6.3(b), and 6.4(b) indicates that the local magnetic shear, which is the stabilizing term of high-mode-number ballooning modes, is significantly reduced on the outer side of the torus, especially at the horizontally elongated poloidal cross section, as the Shafranov shift increases. Moreover, it is understood from a comparison of Figures 6.2(c), 6.3(c), and 6.4(c) that the locally unfavorable magnetic curvature at the horizontally elongated poloidal cross section becomes stronger on the inner side of the torus than that on the outer side of the torus. The reason is as follows. In this horizontally elongated poloidal cross section, the normal magnetic curvature κ^n is approximated as

$$\kappa^n = \frac{\psi}{B^2}\frac{\partial B^2}{\partial \psi}. \tag{6.5}$$

At the considered β-value, the diamagnetic effect is so weak that the distribution of the magnetic field strength hardly changes. However, the change in the distribution of flux surfaces due to the Shafranov shift is quite large as shown in Figures 6.3(a), 6.4(a). The interval of flux surfaces on the inner side of the torus is wider than that on the outer side of the torus. Therefore, the locally unfavorable magnetic curvature at the horizontally elongated poloidal cross section becomes stronger on the inner side of the torus than that on the outer side of the torus.

As β increases, the toroidicity-dominant Mercier-unstable equilibria created by peaked pressure profiles with no net toroidal current have a second stability region with respect to interchange modes. The reason is that the average magnetic curvature due to the Shafranov shift is favorable in the region where the maximum pressure gradient of peaked pressure profiles exists (see figure 6.1(a)). In contrast, helicity-dominant Mercier-unstable equilibria created by broad pressure profiles with no net toroidal current do not have second stability against interchange modes, because the maximum pressure gradient still exists in an average unfavorable magnetic curvature region (see figure 6.1(b)). Thus, the toroidicity-dominant equilibria are more Mercier stable than the helicity-dominant equilibria.

6.3 Global mode analysis in toroidicity-dominant Mercier-unstable equilibria

The typical phase factors (M_P, N_P) are chosen to be $(5,3)$ for low toroidal mode numbers $n < M$, $(19,11)$, $(23,13)$, $(28,16)$, and $(38,22)$ for moderate toroidal mode numbers $n \sim M$, and $(114,66)$, $(133,77)$, $(152,88)$, and $(171,99)$ for fairly high toroidal mode numbers $n \gg M$. The Fourier modes and their number are carefully chosen from $\mathcal{S}1$, the Fourier space of toroidicity-dominant equilibrium given in Appendix A, to span an Fourier subset of perturbation which centers at the corresponding phase factor and create the efficient resonant modes.

For low toroidal mode numbers $n < M$, interchange modes occur, which feel the average magnetic curvature with its local variation averaged out. One with phase factor $(M_P, N_P) = (5,3)$ is shown is Figure 6.5, where the perturbation is given by $\mathcal{P}1$ in Ap-

pendix B. The radial distribution of the Fourier components of the normal displacements $\boldsymbol{\xi} \cdot \nabla \psi$ is shown in Figure 6.5(a). Three resonant mode structures with $n = 3$ are visible, whereas the amplitudes of other modes with different toroidal mode numbers are quite small, and hence the toroidal mode coupling is negligible. Since the Mercier level in this toroidicity-dominant equilibrium is relatively low as shown in Figure 6.1(a), the dominant mode with $(m, n) = (5, 3)$ is quite localized radially around the resonant surface with $\iota = 3/5$ in the Mercier unstable region with $D_M < 0$, together with two small resonant structures with $\iota = 3/6$ and $\iota = 3/4$, both of which are slightly outside the Mercier unstable region. The corresponding contours of the perturbed pressure

$$p_1 = -\nabla p \cdot \boldsymbol{\xi} \tag{6.6}$$

on both vertically and horizontally elongated poloidal cross sections are shown in Figure 6.5(b) and (c). Comparison of the direction between magnetic field lines and constant level surfaces of (6.6) shows that the amplitude of the perturbation is almost constant along a magnetic field line. From these properties, it is concluded that this perturbation is an interchange mode almost free from the toroidal mode coupling. These interchange structure more radially extend on the inner side of torus than on the outer side of torus. The mode structure of the interchange modes will be discussed in detail in the next section.

For moderate toroidal mode numbers $n \sim M$, the modes begin to feel the local structure of the magnetic curvature due to helicity. Since the Shafranov shift strongly reduces the stabilizing effects due to the local magnetic shear on the outer side of torus in the toroidicity-dominant Mercier-unstable equilibrium as shown in Figure 6.3(b), tokamak-like poloidally localized ballooning modes with weak toroidal mode coupling occur. One with phase factor $(M_P, N_P) = (38, 22)$ is shown in Figure 6.6, where the perturbation is given by $\mathcal{P}3$ in Appendix B. The typical toroidal mode numbers are still so small that the pressure-driven modes can not effectively feel the local structure of the magnetic curvature due to helicity, and hence the toroidal mode coupling is weak. Three groups of Fourier modes for the normal displacement $\boldsymbol{\xi} \cdot \nabla \psi$ with different toroidal mode numbers are visible, namely, $n = 22$, $n = 32$, and $n = 42$. This fact results from the weak toroidal mode coupling in 3-D equilibria, as shown in Figure 6.6(a), where the most dominant toroidal mode number is 32. Each group, however, consists of many Fourier modes with different poloidal mode numbers caused by the poloidal mode coupling, and the Fourier

modes existing in the region with a finite global magnetic shear ($r_N \geq 0.55$) have the largest amplitude around the resonant flux surface satisfying $\epsilon = n/m$. Thus, the structure of each group due to the poloidal mode coupling is quite similar to that of ballooning modes in tokamak plasma. The Fourier modes have the finite amplitude in the region where the rotational transform monotonically increases in the radial direction ($r_N \geq 0.4$), as shown in Figure 6.1(a), so that the group of Fourier modes with higher toroidal mode number appear in the outer flux surfaces. The most dominant group of the Fourier modes with $n = 32$ exists around the Mercier-unstable region, and other two groups with $n = 22$ and $n = 42$ extend from the Mercier-unstable region into the Mercier-stable region. The group with $n = 22$ extends into a considerably weak magnetic shear region ($r_N \sim 0.45$), where the high-mode-number ballooning formalism breaks down, and slightly off-resonant modes without the resonant surface have the finite amplitude there. Note that among the three groups of Fourier modes with different toroidal mode numbers, neighboring groups have opposite phase: e.g., between $n = 22$ and $n = 32$, and between $n = 32$ and $n = 42$. The relation between this relative phase difference and the position of the origin of the toroidal angle, which is located where the poloidal cross section is vertically elongated, indicates a weak localization of the mode in the toroidal direction. A comparison of Figures 6.6(b) and (c) shows that on the outer side of the torus, the radial extension of the perturbed pressure (6.6) is larger on the horizontally elongated poloidal cross section with locally unfavorable magnetic curvature at the outside of the torus, than on the vertically elongated poloidal cross section with locally favorable magnetic curvature at the outside of the torus. On the vertically elongated poloidal cross section, the perturbed pressure on the outer side of torus changes phase in the radial direction.

The influence of the mode family is considered for moderate toroidal mode numbers $n \sim M$. All of the parameters are fixed except for the phase factor, as is shown in the Appendix B. One with phase factor $(M_P, N_P) = (19, 11)$ is shown in Figure 6.7, where the perturbation is given by $\mathcal{P}4$ in Appendix B. This mode belongs to $N_f = 1$ mode family. The three visible groups have toroidal mode number $n = 11$, 21, and 31. The group with toroidal mode number $n = 21$ is the most dominant one and extends around the Mercier-unstable region. Similarly to the tokamak-like ballooning modes given in Figure 6.6, the group with toroidal mode number $n = 11$ extends into the weak magnetic shear region. In the other two mode families, namely, $N_f = 3$ and $N_f = 4$, tokamak-like ballooning modes with phase factors $(M_P, N_P) = (23, 13)$, and $(M_P, N_P) = (28, 16)$ are shown in Figures

6.8 and 6.9, where the perturbation are given by $\mathcal{P}5$ and $\mathcal{P}6$ in Appendix B, respectively. From the four tokamak-like ballooning modes shown from 6.6 to 6.9, it is understood that the growth rate becomes larger as the toroidal mode number increases.

For fairly high toroidal mode numbers $n \gg M$, the modes can easily distinguish the local fine structure of the magnetic curvature due to helicity. This results in the appearance of ballooning modes inherent to 3-D systems, which have so strong poloidal and toroidal mode coupling as to localize highly in both the poloidal and toroidal directions. One is shown in Figure 6.10 with phase factor $(M_P, N_P) = (171, 99)$, where the perturbation is given by $\mathcal{P}7$ in Appendix B. There are six groups of Fourier modes with different toroidal mode numbers for $\boldsymbol{\xi}\cdot\nabla\psi$ through the strong toroidal mode coupling. The different toroidal mode numbers are shown in Figure 6.10(a), namely, $n = 69, 79, 89, 99, 109, 119$, and 129. All groups exist around Mercier-unstable region, where the rotational transform ι monotonically increases in the radial direction. The groups of Fourier modes with higher toroidal mode numbers exist in the region with higher rotational transform, and neighboring groups of Fourier modes have opposite phase to each other, just as in the case of tokamak-like ballooning modes. This relative phase difference of the neighboring groups leads to the clear localization of the perturbed pressure (6.6) in the toroidal direction, as shown in Figures 6.10(c) and 6.10(d). On the outer side of the torus, the perturbed pressure, which localized on the horizontally elongated poloidal cross section with the locally unfavorable magnetic curvature at the outside of torus, almost disappears on the vertically elongated poloidal cross section with the locally favorable magnetic curvature at the outside of torus. Moreover, the strong toroidal mode coupling causes a type of localization that is different from the kind only due to poloidal mode coupling. This phenomenon becomes quite clear in Figure 6.10(b), which shows the corresponding contours of the perturbed pressure on the (θ, ζ) plane with one period in the poloidal direction and one-tenth of a period (one field period) in the toroidal direction at $r_N = 0.710$, where $\iota = 0.57$ and the Fourier mode with $n = 99$ has its maximum amplitude, as indicated in Figure 6.10(a). In Figure 6.10(b), it can be seen that regions where the perturbed pressure has large amplitude (indicated by dark diagonal stripes) alternate with regions of quite small amplitude (denoted by white diagonal stripes). Judging from the value of the rotational transform on this flux surface, namely, $\iota = 0.57$, we conclude that these high-amplitude and low-amplitude stripes are aligned along magnetic field lines, and that the strong the toroidal mode coupling in addition to the poloidal mode coupling makes

the perturbation be localized on the selected flux tubes. The small amplitude regions, i.e., white diagonal stripes, also show that, as well as in the poloidal direction, there is a region with rather low amplitude in the toroidal direction on the outer side of torus, around the vertically elongated poloidal cross section, namely, at $\theta \sim 0$ and $\zeta \sim 0$ (since the origins for the poloidal and toroidal angles exist on the outer side of torus and on the vertically elongated poloidal cross section, respectively). In the case of a tokamak, these low-amplitude regions occur due only to the poloidal mode coupling, and consequently their widths are very narrow. The ballooning modes that are inherent to 3-D systems still have fairly extended structures in the toroidal direction, as shown in Figure 6.10.

Independent of the mode family, ballooning modes inherent to 3-D systems occur for fairly high toroidal mode numbers $n \gg M$. Ones with phase factors $(M_P, N_P) = (114, 66)$, $(M_P, N_P) = (133, 77)$, and $(M_P, N_P) = (152, 88)$ are shown in Figures 6.11, 6.12, and 6.13, respectively. The perturbations are given in $\mathcal{P}8$, $\mathcal{P}9$, and $\mathcal{P}10$ in Appendix B, and they belong to $N_f = 4$, $N_f = 3$, and $N_f = 2$ mode families. They have strong poloidal and toroidal mode couplings, and they localize in the radial direction. Here all of the parameters are the same excepts the phase factors as given in Appendix B. From Figures 6.10 to 6.13, the growth rate, the poloidal and toroidal mode couplings, and the radial localization becomes larger or stronger, as the toroidal mode number increases.

Independent of the value for the typical toroidal mode numbers and the mode families, unstable modes are radially localized near the Mercier-unstable region. As the typical toroidal mode numbers increase, the radial intervals, in which modes are localized, become more and more narrow, the modes become more and more unstable, and also the toroidal mode coupling becomes stronger and stronger through the utilization of the normal magnetic curvature due to helicity. Therefore, it is expected that more unstable ballooning modes localized in one toroidal field period, which are conjectured in the local mode analysis [12], may occur in quite narrow radial intervals as the typical toroidal mode numbers become increasingly larger.

6.4 Global mode analysis in helicity-dominant Mercier-unstable equilibria

The typical phase factors (M_P, N_P) are chosen to be $(7, 4)$ for low toroidal mode numbers $n < M$, $(19, 11)$, $(23, 13)$, $(28, 16)$, and $(38, 22)$ for moderate toroidal mode numbers $n \sim M$, and $(114, 66)$, $(133, 77)$, $(152, 88)$, and $(171, 99)$ for fairly high toroidal mode numbers $n \gg M$. The Fourier modes and their number are carefully chosen from $\mathcal{S}2$, the Fourier space of helicity-dominant equilibrium given in Appendix A, to span an Fourier subset of perturbation which centers at the corresponding phase factor and create the efficient resonant modes.

For low toroidal mode numbers $n < M$, interchange modes occur just as in the case of toroidicity-dominant Mercier-unstable equilibria, which feel the average magnetic curvature. One of them is shown is Figure 6.14 with phase factor $(M_P, N_P) = (7, 4)$, where the perturbation is given by $\mathcal{P}2$ in Appendix B. The radial distribution of the Fourier components of the normal displacements $\xi \cdot \nabla\psi$ is shown in Figure 6.14(a) (where the origin of the poloidal angle is on the outer side of the torus) and (b) (where the origin of the poloidal angle is on the inner side of the torus), where three resonant mode structures with $n = 4$ are visible. The amplitudes of other modes with different toroidal mode numbers are quite small. This equilibrium is strongly Mercier-unstable as shown in Figure 6.1(b), hence the interchange mode has a fairly radially extended structure around the mode rational surfaces with $\iota = 4/7, 4/6$, and $4/5$, all of which are inside the Mercier unstable region with $D_M < 0$. The contours of the perturbed pressure (6.6) shown in Figure 6.14(c) and (d) indicate that the interchange modes with $n < M$ have a large radial extension on the inner side of torus and change phase in the radial direction on the outer side of torus. This is because the normal magnetic curvature is more unfavorable on the inner side of torus than that on the outer side of torus as shown in Figure 6.4(c) and also consistent with the results in [43] and [44]. These properties are more easily understood from Figure 6.14(b), where the Fourier modes of the the normal displacements $\xi \cdot \nabla\psi$ are displayed with the origin of the poloidal angle shifted from the outer side of torus to the inner side of torus, so that the Fourier modes with an odd poloidal mode number change their signs. In this case, the Fourier modes with $(m, n) = (7, 4)$ and $(m, n) = (5, 4)$ change their signs. The mode structure is similar to that of a ballooning mode except

that each Fourier mode has both positive and negative parts, which means that this type of interchange modes have a tendency to localize (or to extend radially) on the inner side of torus and to change phase in the radial direction on the outer side of torus through poloidal mode coupling. In other words, this type of interchange modes is anti-ballooning with respect to the poloidal mode coupling.

For moderate toroidal mode numbers $n \sim M$, Figure 6.15 shows that interchange modes still occur, in which the phase factor is $(M_P, N_P) = (38, 22)$ and the perturbation is still given by $\mathcal{P}3$. Here, tokamak-like poloidally localized ballooning modes do not appear in the helicity-dominant Mercier-unstable equilibria, in contrast with the case for the toroidicity-dominant Mercier-unstable equilibrium. The reason of this is due to the fact that the reduction of stabilizing term of ballooning modes by the Shafranov shift is not enough for tokamak-like poloidally localized ballooning modes to be destabilized as shown in Figure 6.4(b). Thus interchange modes driven by the average unfavorable magnetic curvature are destabilized. The toroidal mode coupling of interchange modes becomes stronger as the toroidal mode number increases, as shown in Figure 6.15(a) (where the origin of the poloidal angle is on the outer side of the torus) and (b) (where the origin of the poloidal angle is on the inner side of the torus), where two groups of Fourier modes with $n = 22$, and $n = 32$ are dominant. Compared with interchange modes with $n < M$ shown in Figure 6.14, the interchange modes with $n \sim M$ also have a tendency to be radially extended on the inner side of torus and to change phase in the radial direction on the outer side of torus due to poloidal mode coupling, as shown in Figures 6.15(c) and 6.15(d). Moreover, the weak toroidal mode coupling, in cooperation with the poloidal mode coupling, causes a bumpy-like localization of the perturbed pressure in the poloidal direction, which is more clearly seen on the inner side of the torus in Figures 6.15(c) and (d).

Independent of the mode family, interchange modes still occur for moderate toroidal mode numbers $n \sim M$. For the same perturbations used in the toroidicity-dominant Mercier-unstable equilibria, these interchange modes are shown from Figures 6.16 to 6.18. Clearly, as the toroidal mode number increases, the growth rate, the toroidal mode coupling, and the radial localization becomes larger or stronger.

For fairly high toroidal mode numbers $n \gg M$, just as in the toroidicity-dominant Mercier-unstable equilibrium, the modes can distinguish the fine local structure of the magnetic curvature due to helicity. This results in ballooning modes inherent to 3-D

systems just as for the toroidicity-dominant Mercier-unstable equilibrium shown in Figures 6.10 $\sim$ 6.12, which have strong poloidal and also toroidal mode coupling and localize in both the poloidal and toroidal direction. On case with phase factor $(M_P, N_P) = (171, 99)$ is shown in Figure 6.19, where the perturbation is still given by $\mathcal{P}7$. The dominant toroidal mode numbers of the Fourier modes of $\boldsymbol{\xi} \cdot \nabla\psi$ are shown in Figure 6.19(a), namely, $n = 89, 99, 109, 119, 129, 139$, and 149. One more group exists in this equilibrium than in the toroidicity-dominant Mercier-unstable one. The most dominant toroidal mode number of this ballooning mode is $n = 119$.

Ballooning modes inherent to 3-D systems occur independent of the mode family. For the same perturbations used in the toroidicity-dominant Mercier-unstable equilibria, these ballooning modes inherent to 3-D systems are shown from Figures 6.20 to 6.22. Similarly, as the toroidal mode number increases, the growth rate, the toroidal mode coupling, and the radial localization becomes larger or stronger.

Just as for toroidicity-dominant equilibria, unstable modes radially localize around the Mercier-unstable region independent of their typical toroidal mode numbers and mode families. As the typical toroidal mode numbers increase, the modes become more unstable and more radially localized, and have a stronger toroidal mode coupling through the normal magnetic curvature due to helicity. Compared to the interchange modes with low toroidal mode numbers shown in Figure 6.14, interchange modes with moderate toroidal mode numbers (shown in Figures 6.15 $\sim$ 6.18) and ballooning modes with fairly high toroidal mode numbers (shown in Figures 6.19 $\sim$ 6.22) are significantly localized in the radial direction.

The typical contribution from T-version are given in figure 6.23, in which the competition between the stabilizing effect from field line bending (curve 1: T^1) and the destabilizing effect from pressure-driven term (curve 3: T^3) is clearly demonstrated. Figure 6.23(a) shows the contributions from interchange modes with toroidal mode number $n < M$. The contributions from tokamak-like ballooning mode with toroidal mode number $n \sim M$ are shown in Figure 6.23(b), from ballooning mode inherent to 3-D systems with toroidal mode number $n \gg M$ in Figure 6.23(c). T^1 is contributed by Shear Alfvén mode which is a stabilizing term and is independent of $k_\perp$ even when $k_\perp \gg k_\parallel$. The Shear Alfvén wave is purely transverse. This cause the magnetic field lines to bend. The Shear Alfvén wave describes a basic oscillation between perpendicular plasma kinetic energy and perpendicular "line bending" magnetic energy; i.e., a balance between inertial and field line tension. T^2 (curve 2) represents the stabilizing contribution from field line compression. This term is nearly invisible since it is always minimized by the most unstable mode. T^3 (curve 3) makes a contribution the destabilization of pressure-driven modes when the magnetic curvature is unfavorable. T^4 (curve 4) represents kink contribution. As the toroidal mode number increases, this contribution becomes smaller and smaller. This fact complies with the local mode analysis since there is no kink contribution for high-mode-number ballooning modes.

All of the eigenvalues for pressure-driven modes shown from figures 6.5 to 6.22 are given in the left (right) column of Table 6.1 for the toroidicity-dominant (helicity-dominant) Mercier-unstable equilibrium. Clearly in both types of equilibria, as the dominant toroidal mode number increases, the absolute magnitude of corresponding eigenvalues becomes large.

In order to investigate those results in Sections 6.3 and 6.4 more carefully, two different auxiliary equilibria were introduced, created by changing only the boundary shape of the original equilibria. One is a toroidicity-dominant equilibrium and the other is a helicity-dominant equilibrium. Both auxiliary equilibria have quite similar local structures of the local magnetic shear and the normal magnetic curvature to those in the original equilibria, and are more Mercier unstable than the original equilibria, as shown in Figure 6.1 by the dashed curves. In spite of difference of the violated level of the Mercier criterion, namely, the magnitude of negative D_M, those two toroidicity-dominant equilibria and the two helicity-dominant equilibria produced qualitatively the same results, respectively. Therefore, thought to be quite reasonable are the categorization of the equilibria

into toroidicity-dominant and helicity-dominant Mercier-unstable equilibria according to the degree of the reduction of the local magnetic shear by the Shafranov shift, and the resultant behavior of the pressure-driven modes in the both types of Mercier-unstable equilibria.

Table 6.1 The properties of ω^2

toroidicity-dominant		helicity-dominant	
(M_P, N_P)	ω^2	(M_P, N_P)	ω^2
$(5, 3)$	-4.99×10^{-5}	$(7, 4)$	-3.07×10^{-3}
$(19, 11)$	-7.04×10^{-4}	$(19, 11)$	-5.21×10^{-3}
$(23, 13)$	-9.19×10^{-4}	$(23, 13)$	-5.25×10^{-3}
$(28, 16)$	-1.26×10^{-3}	$(28, 16)$	-5.31×10^{-3}
$(38, 22)$	-1.89×10^{-3}	$(38, 22)$	-5.26×10^{-3}
$(114, 66)$	-5.05×10^{-3}	$(114, 66)$	-6.16×10^{-3}
$(133, 77)$	-5.51×10^{-3}	$(133, 77)$	-6.45×10^{-3}
$(152, 88)$	-5.89×10^{-3}	$(152, 88)$	-6.68×10^{-3}
$(171, 99)$	-6.22×10^{-3}	$(171, 99)$	-6.88×10^{-3}

Chapter 7

Conclusions

By means of global mode analysis of ideal MHD modes for equilibria in fully 3-D systems in a planar axis $L = 2/M = 10$ heliotron system with an inherently large Shafranov shift, the conjecture from local mode analysis [12] for Mercier-unstable equilibria has been investigated and the properties of pressure-driven modes, namely, interchange modes and ballooning modes, inherent to such 3-D systems have been clarified.

From the view point of numerical procedure, an efficient eigensolver has been introduced. With the application of Lanczos recursion with no re-orthogonalization, the memory increases is controlled to a neglected order. With the application of an shift-and-invert technique, the convergence of the Lanczos recursion is accelerated considerably. In a word, the Lanczos algorithm is shown to be efficient and reliable in solving eigenproblem arising from ideal MHD stability analysis. A good starting vector in inverse iteration has been introduced to comply with the characteristics of pressure-driven modes in 3-D configurations.

From the view point of the ideal MHD stability, a vacuum configuration of a planar axis $L = 2/M = 10$ heliotron system is helicity dominant, which comes from the helical coils. Both the local magnetic magnetic shear and normal magnetic curvature are mainly determined by helicity. The characteristics of the finite-β equilibria in such systems are determined by an essentially axisymmetric, inherently large Shafranov shift. The change in the local structures of the local magnetic magnetic shear (integrated along the magnetic field line) and the normal magnetic curvature brought by the Shafranov shift is related to toroidicity. The Shafranov shift reduces the (integrated) local magnetic magnetic shear on the outside of torus, leading to the reduction of the field line bending stabilizing effect

on ballooning modes. On the other hand, the Shafranov shift enhances (reduces) the local unfavorable magnetic curvature on the inner (outer) side of torus.

According to the degree of the reduction of the local magnetic magnetic shear by Shafranov shift, the Mercier-unstable equilibria in a planar axis $L = 2/M = 10$ heliotron system has been categorized into two types, namely, toroidicity-dominant Mercier-unstable equilibria and helicity-dominant Mercier-unstable equilibria. The toroidicity-dominant Mercier-unstable equilibria are characterized by the properties that the local magnetic shear is fairly reduced by the Shafranov shift, so that ballooning modes are easily destabilized. These equilibria are created with a peaked pressure profile either with zero net toroidal current or with net toroidal current such that the rotational transform decreases slightly. The helicity-dominant Mercier-unstable equilibria are characterized by the properties that the local magnetic magnetic shear is less reduced by the Shafranov shift, so that ballooning modes are hardly destabilized. These equilibria are created with a broad pressure profile either with zero net toroidal current or with net toroidal current such that the rotational transform increases slightly. The toroidicity-dominant Mercier-unstable equilibria tend to be more Mercier stable than the helicity-dominant Mercier-unstable equilibria for the same β value at the magnetic axis, because the average magnetic curvature due to Shafranov shift is favorable (unfavorable) in the region where the pressure gradient is large, for the former (latter) equilibria.

Since the local magnetic curvature due to helicity has the same period M in the toroidal direction as the toroidal field period of the equilibria, the characteristics of the pressure-driven modes in such Mercier-unstable equilibria dramatically change according to how much the local magnetic magnetic shear is reduced and also according to the relative magnitude of the typical toroidal mode numbers n of the perturbations compared with the toroidal field period M of the equilibria.

In the toroidicity-dominant Mercier-unstable equilibria, the pressure-driven modes change from interchange modes for low toroidal mode numbers $n < M$, to tokamak-like poloidally localized ballooning modes with weak toroidal mode coupling for moderate toroidal mode numbers $n \sim M$, and finally to both poloidally and toroidally localized ballooning modes purely inherent to 3-D systems with strong poloidal and toroidal couplings for fairly high toroidal mode numbers $n \gg M$. Strong toroidal mode coupling, in cooperation with poloidal mode coupling, makes the perturbation localize to flux tubes.

In the helicity-dominant Mercier-unstable equilibria , the pressure-driven modes change

from interchange modes localized on the inner side of torus for $n < M$ or $n \sim M$, directly to poloidally and toroidally localized ballooning modes purely inherent to 3-D systems with strong poloidal and toroidal couplings for fairly high toroidal mode numbers $n \gg M$. Since the normal magnetic curvature is more unfavorable on the inner side of torus than on the outer side of torus, the interchange modes are localized on the inner side of torus for $n < M$ or $n \sim M$. This type of interchange modes is anti-ballooning with respect to the poloidal mode coupling.

Since the equilibria considered here are Mercier-unstable, interchange modes with low toroidal mode numbers $n < M$, experiencing unfavorable magnetic curvature with its local structure averaged out, occur for both toroidicity-dominant Mercier-unstable equilibria and helicity-dominant Mercier-unstable equilibria. For fairly high toroidal mode numbers $n \gg M$, the perturbations can feel fine local structure of the magnetic curvature and also the local magnetic magnetic shear is reduced more or less in both types of equilibria, and consequently poloidally and toroidally localized ballooning modes inherent to 3-D systems are destabilized for both toroidicity-dominant and helicity-dominant equilibria. The situation for moderate toroidal mode numbers $n \sim M$ is different for toroidicity-dominant and helicity-dominant equilibria. The local magnetic magnetic shear is more reduced in toroidicity-dominant Mercier-unstable equilibria than in helicity-dominant Mercier-unstable equilibria, and also the modes with moderate toroidal mode numbers $n \sim M$ can not feel the local structure of the normal magnetic curvature effectively. Thus tokamak-like poloidally localized ballooning modes with weak toroidal mode coupling can be easily destabilized in toroidicity-dominant equilibria; and interchange modes, driven by the average unfavorable magnetic curvature and not experiencing the affect of toroidal mode coupling, can be destabilized for helicity-dominant Mercier-unstable equilibria.

All of these properties of the pressure-driven modes in Mercier-unstable equilibria are common for different mode families and are quite consistent with conjecture from local mode analysis given in [12].

Appendix A

Fourier space of equilibria

The 3-D finite-β equilibria are calculated with VMEC under the fixed boundary condition. All of the quantities are expressed in terms of the Fourier decomposition in both the poloidal and toroidal directions. In order to be able to reconstruct the MHD equilibria in the Boozer coordinate system (ψ, θ, ζ) from VMEC coordinates, the accuracy of the corresponding mapping (from VMEC coordinates to Boozer coordinates) is estimated from the relative errors in B and R due to the transformation at the grid points. The maximum relative errors in B and R for the toroidicity-dominant equilibrium are 1×10^{-5} and 3×10^{-7}, respectively. For the helicity-dominant equilibrium, the corresponding relative errors are 7×10^{-7} and 1×10^{-7}. Let m_e and n_e be the poloidal and toroidal mode indices of the equilibria in the Boozer coordinates, respectively, then the total number of Fourier modes, i.e., (m_e, n_e) in an equilibrium will be given by $M^0_{eq} = (m_e + 1) \times (n_e + 1) + m_e \times n_e$. Note that the number of poloidal modes is important for equilibria with a large Shafranov shift, and that this number increases as the Shafranov shift becomes larger. The Fourier spaces of the two types of Mercier-unstable equilibria, introduced in chapter 6, are given as $\mathcal{S}1$ and $\mathcal{S}2$.

Fourier space of toroidicity-dominant Mercier-unstable equilibrium

$$\mathcal{S}1 = \{(m_e, n_e) : m_e \in [0, 30], n_e \in [-10, 10], M^0_{eq} = 641\} \tag{A.1}$$

Fourier space of helicity-dominant Mercier-unstable equilibrium

$$\mathcal{S}2 = \{(m_e, n_e) : m_e \in [0, 30], n_e \in [-10, 10], M^0_{eq} = 641\} \tag{A.2}$$

Appendix B

Fourier subset of perturbations

The Fourier subsets of perturbations are created by the given phase factors (M_P, N_P) and M_{eq} selected Fourier modes (m_e, n_e) from the equilibrium Fourier spaces $\mathcal{S}1$ or $\mathcal{S}2$ according to the mode family requirement satisfying (4.9). The total number of Fourier modes in a perturbation will be given by $M_{pt} = 2 \times M_{eq} - 1$. For different phase factors and different equilibrium Fourier modes, perturbations will be different. A perturbation, to which mode family it belongs, is determined by the relation of the toroidal index N_P and the toroidal period of equilibrium magnetic field. Since the configuration considered here has $M = 10$ toroidal field period, the basic indices of the mode families are $N_f = 0, 1, 2, 3, 4, 5$.

In this work, the following ten perturbations are investigated.

$$\mathcal{P}1 = \{(M_P, N_P) = (\ 5,\ 3), M_{eq} = \ 76, M_{pt} = 151, N_f = 3\} \tag{B.1}$$

$$\mathcal{P}2 = \{(M_P, N_P) = (\ 7,\ 4), M_{eq} = \ 62, M_{pt} = 123, N_f = 4\} \tag{B.2}$$

$$\mathcal{P}3 = \{(M_P, N_P) = (\ 38, 22), M_{eq} = 186, M_{pt} = 371, N_f = 2\} \tag{B.3}$$

$$\mathcal{P}4 = \{(M_P, N_P) = (\ 19, 11), M_{eq} = 186, M_{pt} = 371, N_f = 1\} \tag{B.4}$$

$$\mathcal{P}5 = \{(M_P, N_P) = (\ 23, 13), M_{eq} = 186, M_{pt} = 371, N_f = 3\} \tag{B.5}$$

$$\mathcal{P}6 = \{(M_P, N_P) = (\ 28, 16), M_{eq} = 186, M_{pt} = 371, N_f = 4\} \tag{B.6}$$

$$\mathcal{P}7 = \{(M_P, N_P) = (171, 99), M_{eq} = 336, M_{pt} = 671, N_f = 1\} \tag{B.7}$$

$$\mathcal{P}8 = \{(M_P, N_P) = (114, 66), M_{eq} = 336, M_{pt} = 671, N_f = 4\} \tag{B.8}$$

$$\mathcal{P}9 = \{(M_P, N_P) = (133, 77), M_{eq} = 336, M_{pt} = 671, N_f = 3\} \tag{B.9}$$

$$\mathcal{P}10 = \{(M_P, N_P) = (152, 88), M_{eq} = 336, M_{pl} = 671, N_f = 2\} \tag{B.10}$$

In the toroidicity-dominant Mercier-unstable equilibrium, the toroidal mode numbers are chosen to satisfy $n < M$, $n \sim M$, and $n \gg M$. For $n < M$ order, the phase factor $(5, 3)$ is used. The resultant perturbation is $\mathcal{P}1$, shown in Figure B.1. For $n \sim M$ order, the phase factors $(38, 22)$, $(19, 11)$, $(23, 13)$, and $(28, 16)$ are used. The resultant perturbations are $\mathcal{P}3$, $\mathcal{P}4$, $\mathcal{P}5$, and $\mathcal{P}6$, shown in Figures B.3, B.4, B.5, and B.6. For $n \gg M$ order, the phase factors $(133, 77)$, $(114, 66)$, and $(152, 88)$ are used. The resultant perturbations are $\mathcal{P}7$, $\mathcal{P}8$, and $\mathcal{P}9$, shown in Figures B.7, B.8, and B.9. Correspondingly, 76, 186, and 336 Fourier modes are selected from $\mathcal{S}1$ to centering these parameters, respectively.

In the helicity-dominant Mercier-unstable equilibrium,the toroidal mode numbers are chosen to satisfy $n < M$, $n \sim M$, and $n \gg M$. For $n < M$ order, the phase factor $(7, 4)$ is used. The resultant perturbation is $\mathcal{P}2$ shown in Figure B.2. For $n \sim M$ and $n \gg M$ orders, we use the same perturbations in the toroidicity-dominant Mercier-unstable equilibria in order to intensively study the inherent properties of pressure-driven modes in the 3-D Mercier-unstable equilibria. For $n \sim M$ order, $\mathcal{P}3$, $\mathcal{P}4$, $\mathcal{P}5$, and $\mathcal{P}6$ are used. For $n \gg M$ order, $\mathcal{P}7$, $\mathcal{P}8$, and $\mathcal{P}9$ are used.

Bibliography

[1] I.B.Bernstein, E.A.Friedman, M.D.Kruskal, and R.M.Kulsrud, *Proc. Roy. Soc. London*, Ser.**A244**, 17(1958).

[2] D.CORREA-RESTREPO, Z.Naturforsch. **33**a, 789(1978).

[3] D.CORREA-RESTREPO, Z.Naturforsch. **37**a, 848(1982).

[4] J.W. Connor, R.J. Hastie and J.B. Taylor, Proc. R. Lond. A. **365**, 1(1979).

[5] R.L. Dewar and A.H. Glasser, Phys. Fluids **26**, 3038(1983).

[6] V.D. Shafranov, Phys. Fluids **26**, 357(1983).

[7] J. Nuhrenberg and R. Zille, Phys. Lett. A **114**, 129(1986).

[8] X. Llobet, H.L. Berk, and M.N. Rosenbluth, Phys. Fluids **30**, 2750(1987).

[9] A.E. Lifschitz, Phys. Lett. A**122**, 350(1987).

[10] W.A. Cooper, S.P. Hirshman, and D.K. Lee, Nuc. Fus. **29**, 617(1989).

[11] N. Nakajima, Phys. Plasmas **3**, 4545 (1996).

[12] N. Nakajima, Phys. Plasmas **3**, 4556 (1996).

[13] M.S.Chance, J.M.Greene, R.C.Grimm, J.L.Johnson, and J.Manickam, J. Comput. Phys. **28**, 1(1978).

[14] R.C.Grimm, J.M.Greene, J.L.Johnson, Meth. Comput. Phys. **16**, 253(1976).

[15] R.Gruber, F.Troyon, D.Berger, L.C.Bernard, S.Rousset, R.Schreiber, W.Kerner, W.Schneider, and K.V.Roberts, Comput. Phys. Commun. **21**, 323(1981).

[16] D.V.Anderson, W.A.Cooper, R.Gruber, S.Merazzi, and U.Schwenn, Int. J. Supercomput. Appl. **4**, 3(1990).

[17] C.Schwab, *Phys. Fluids* B**5**, 9(1993).

[18] J.P. Freidberg, *Ideal Magnetohydrodynamics*, Plenum Press, New York, 1987.

[19] S. Chandrasekar, *Hydrodynamic and Hydromagnetic Stability*, Clarendon, Oxford, 1961.

[20] B.R. Suydam, In *Proceedings of the Second United Nations International Conference on the Peaceful Uses of Atomic Energy*, United Nations, Geneva **31**, 157(1958).

[21] C. Mercier, *Nucl. Fusion Suppl. Pt.* **2**, 801(1962).

[22] J.M. Greene and J.L. Johnson, *Phys. Fluids* **5**, 510(1962).

[23] R.D.Hazeltine and J.D.Meiss, *Phys. Rep.* **121**, 1(1985).

[24] A. Iiyoshi, M. Fujiwara, O. Motojima, N. Oyabu, and K. Yamazaki, Fusion Technol. **17**, 148(1990).

[25] A.H. Boozer, Phys. Fluids B**5**, 3195(1980).

[26] R. Gruber, J. Rappar, *Finite element Methods in Linear Ideal Magnetohydrodynamics*, Springer, New York, 1985.

[27] G. Anania and J.L. Johnson, *Phys. Fluids* **26**, 3070(1983).

[28] Y. Nakamura, K. Ichiguchi, M. Wakanani, and J.L. Johnson, *J. Phys. Soc. Japan*, **58**, 3157(1989).

[29] G.H.Golub and C.F.van Loan, *Matrix Computations*, 3rd Ed., The Johns Hopkins University Press, (1996).

[30] A.M. Ostrowski, *V. Arch. Rational. Mesh. Anal.*, **3**, 472-481(1959).

[31] C. C. Paige, Accuracy and effectiveness of the Lanczos algorithm for the symmetric eigenproblem, *Linear Algebra Appl.* **34**, (1980), p.235.

[32] J. K. Cullum and R. A. Willoughby, *Lanczos algorithms for large symmetric eigenvalue computations, volume 1, Theory* (Birkhauser, Boston 1985).

[33] C. Lanczos, An iterative method for the solution of the eigenvalue problem of linear differential and integral operators. *J. Res. Natl. Bur. Stand* **45**, 255(1950).

[34] W.E. Arnoldi, The principle of minimized iteration in the solution of the matrix eigenproblem. *Quart. Appl. Math.* **9**, 17(1951).

[35] C. C. Paige, Computational variants of the Lanczos method for the eigenproblem, *J. Inst. Math. Appl.* **10**, (1972), p.373.

[36] C. C. Paige, Error analysis of the Lanczos algorithm for tridiagonalizing a symmetric matrix. *J. Inst. Math. Appl.* **18**, (1976), p.341.

[37] B.S.Garbow, J.M.Boyle, J.J.Dongarra, C.B.Moler, EISPACK Guide, *Lecture Notes in Computer Science* **51**, 2nd Ed., Springer, New York (1977).

[38] E.Anderson, Z.Bai, C.Bischof, J.Demmel, J.Dongarra, J.DuCroz, A.Greenbaum, S.hammarling, A.McKenney, S.Ostrouchov, and D.Sorenson, *LAPACK Users' Guide, Release 2.0*, 2nd ed., SIAM Publications, Philadelphia (1995).

[39] J.Chen, N.Nakajima, and M.Okamoto, *Comput. Phys. Commun.* **113** 1(1998).

[40] G.Laval, C.Mercier, and R.Pellat, Nuc. Fus., **5**, 156(1965).

[41] G.Bateman, *MHD Instabilities*, The MIT Press, 1980

[42] J. Manickam, N. Pomphrey, and A.M.M. Todd, Nucl. Fusion **27**, 1461 (1987).

[43] W.A.Cooper, D.B.Singleton, and R.L.Dewar, Phys. Plasmas **3**, 275(1996).

[44] P. Cuthbert, J.L.V. Lewandowski, H.J.Gardner, M. Persson, D.B.Singleton, R.L.Dewar, N. Nakajima, and W.A.Cooper, Phys. Plasmas **5**, 2921(1998).

[45] E.Hameiri, Phys. Fluids **23**, 889(1980).

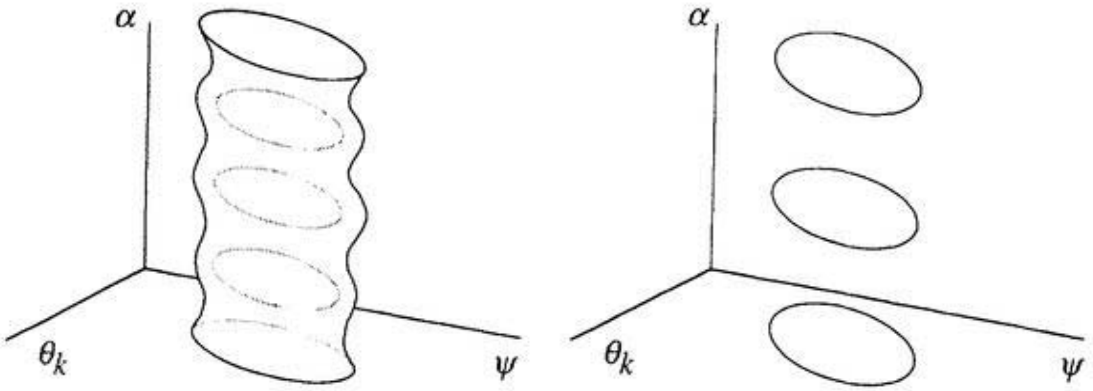

(a) (b)

Figure 3.1 Schematic pictures of the topological level surfaces
for unstable eigenvalues $\omega^2(<0)$ in (ψ, θ_k, α) space

(a) a Mercier-unstable 3-D equilibrium,
(b) a Mercier-stable 3-D equilibrium.

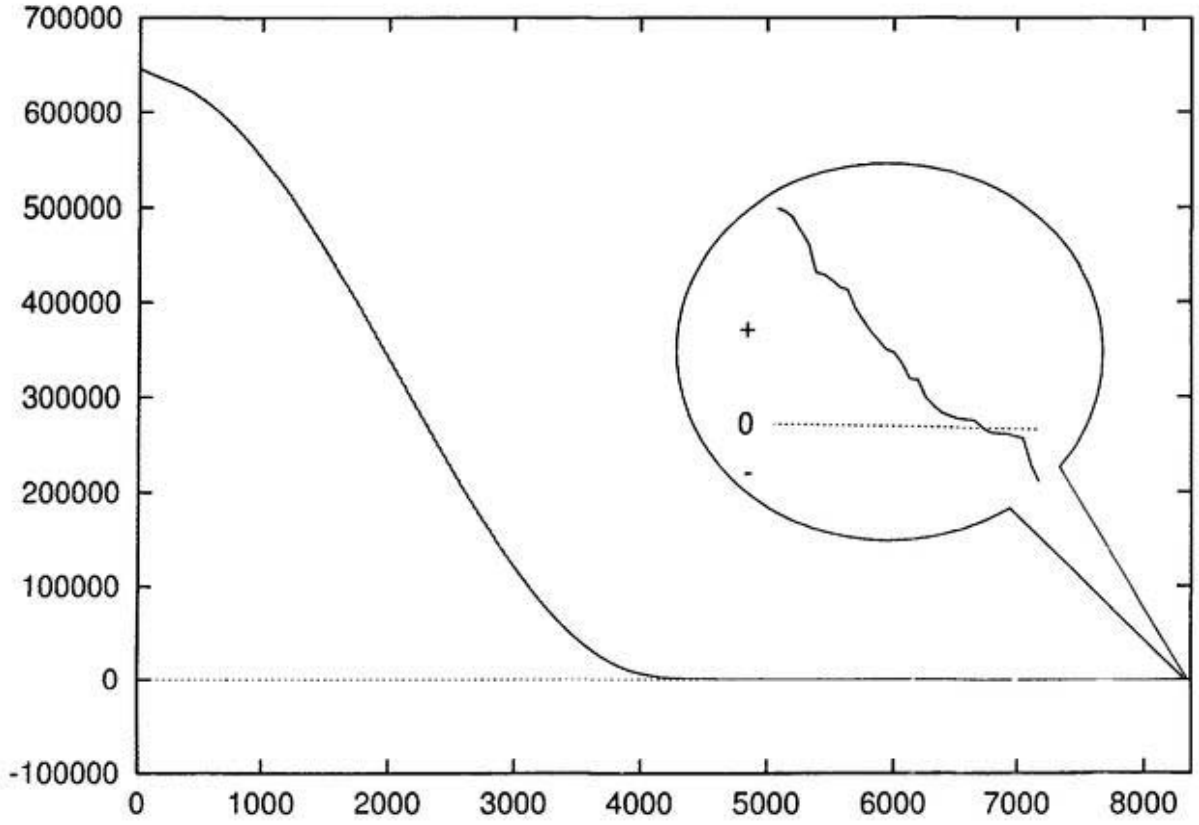

Figure 5.1 Ideal MHD Spectrum in 3-D ideal MHD equilibrium obtained by CAS3D2MN. The perturbation belongs to the $N_f = 5$ mode family with the phase factor $(M_P, N_P) = (8, 5)$. $N_S = 120$, $M_{eq} = 18$, $M_{pt} = 35$. The smallest and the largest eigenvalues are $\lambda_{min} = -2.14952 \times 10^{-3}$ and $\lambda_{max} = 6.47634 \times 10^6$, respectively. The matrix stiffness $S(\mathbf{A})$, i.e., $\lambda_{min}/\lambda_{max}$ is in $O(10^9)$ order. The positive part is dominant.

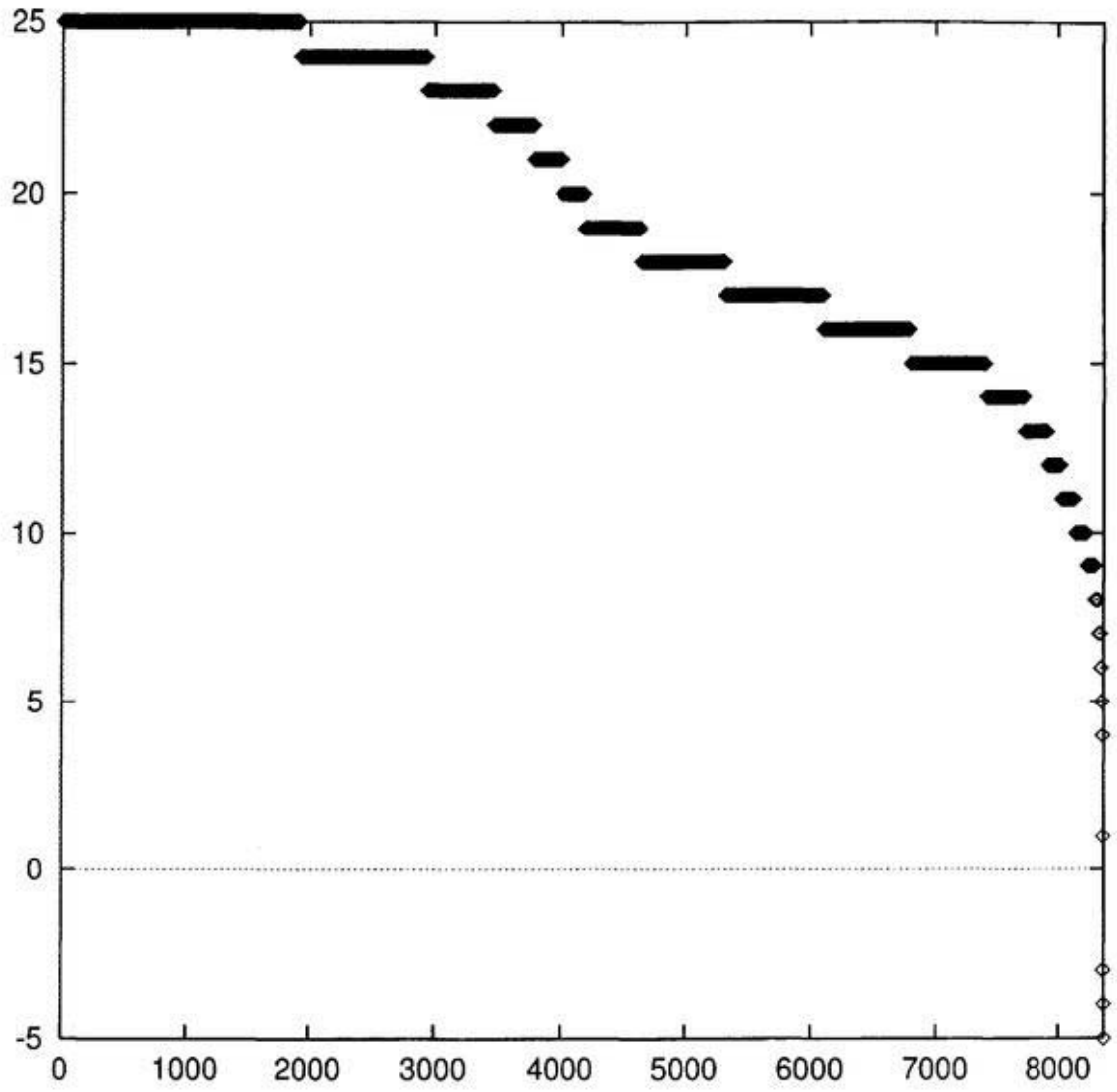

Figure 5.2 Spectrum given in Figure 5.1 is scaled by $\sinh^{-1}(\alpha\lambda)$ with $\alpha = 10^5$. $\sinh^{-1}(\alpha\lambda)$ passes origin and is symmetric about origin ($> 0, = 0, < 0$ for $\lambda > 0, = 0, < 0$). There are 8435 eigenvalues and only 7 are negative, leading to that the negative part, what we concern, is undominant.

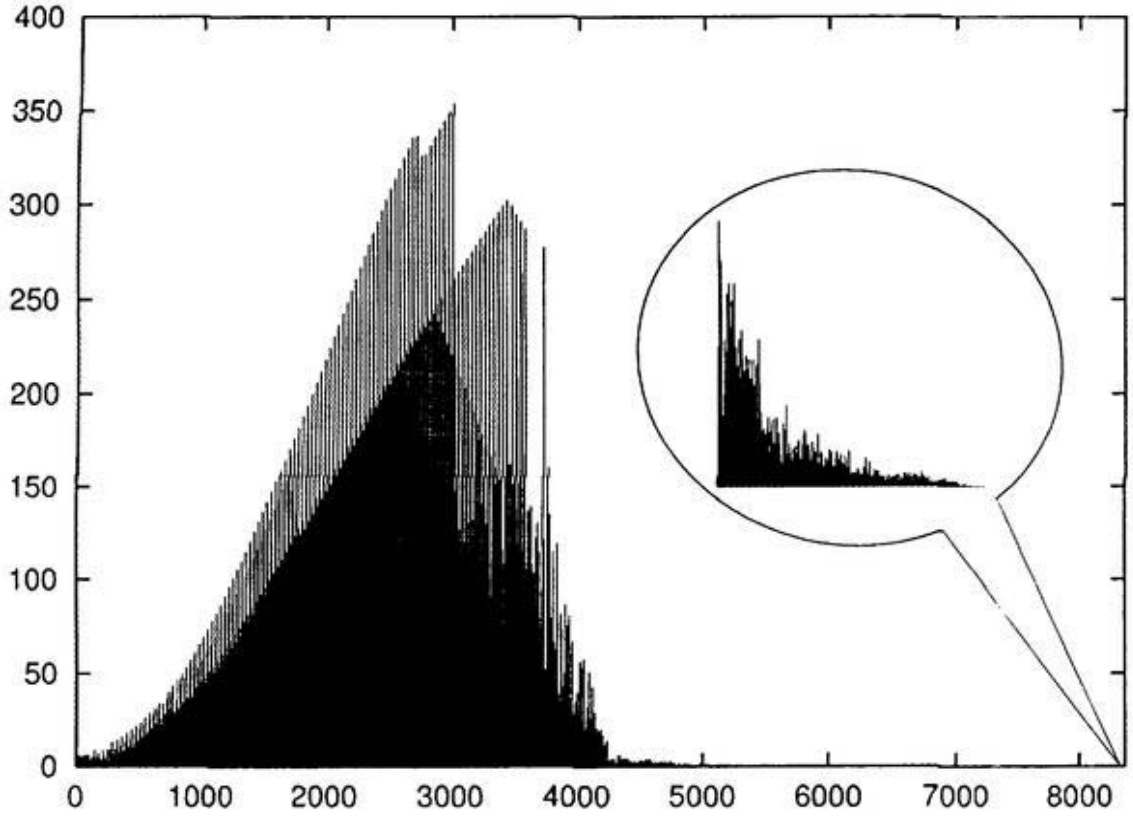

Figure 5.3 Gap stiffness for spectrum given in Figure 5.1, where $g_{min} = 4.07164 \times 10^{-6}$, $g_{max} = 3.54277 \times 10^{2}$, and $S_g(\mathbf{A}) = 8.70109 \times 10^{7}$. Lanczos steps m required by recursion (5.7) to calculate λ_{min} is $11n$.

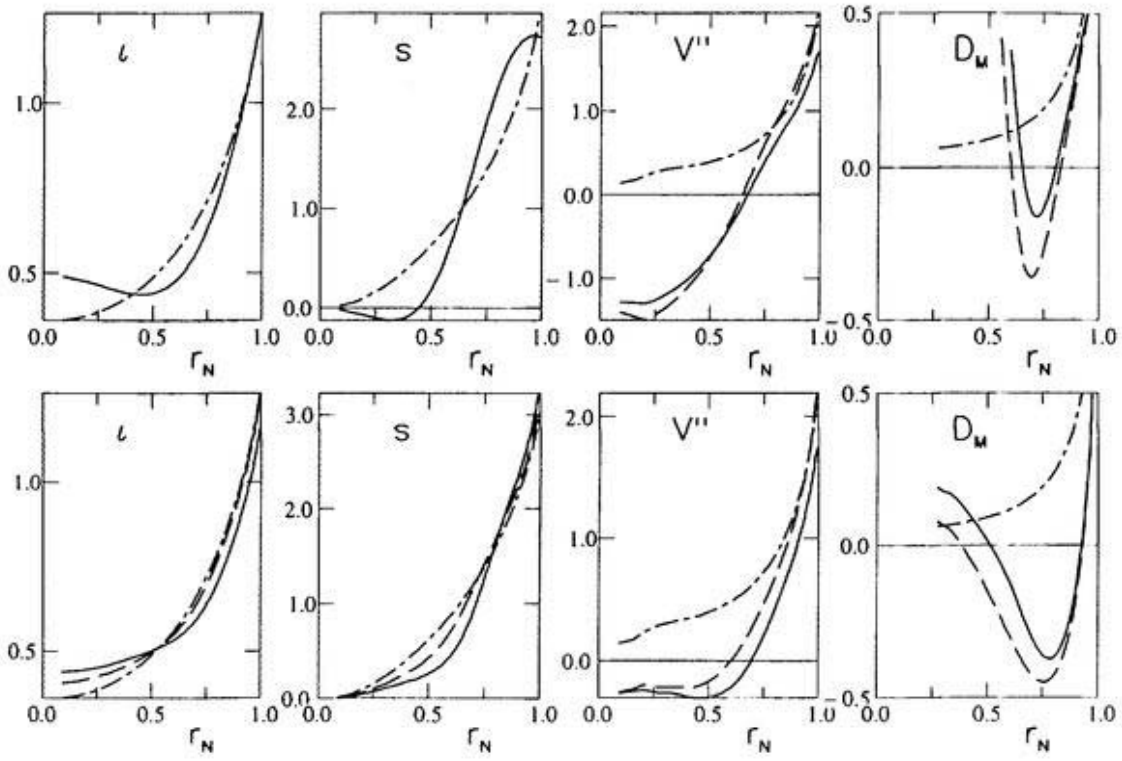

Figure 6.1 Surface quantities

(a) toroidicity-dominant Mercier-unstable equilibrium,
(b) helicity-dominant Mercier-unstable equilibrium.

Global rotational transform ι, global magnetic shear $s = 2\dfrac{d\ln\iota}{d\ln\psi}$, average magnetic curvature (average magne tic well or hill) index V'', and Mercier criterion parameter D_M. all as functions of the normalized minor radius $r_N = \sqrt{\psi_N}$. For both equilibria, quantities corresponding to the vacuum configuration are drawn by dashed-and-dotted curves. Quantities drawn by dashed curves correspond to the modified equilibria mentioned in chapter 6.

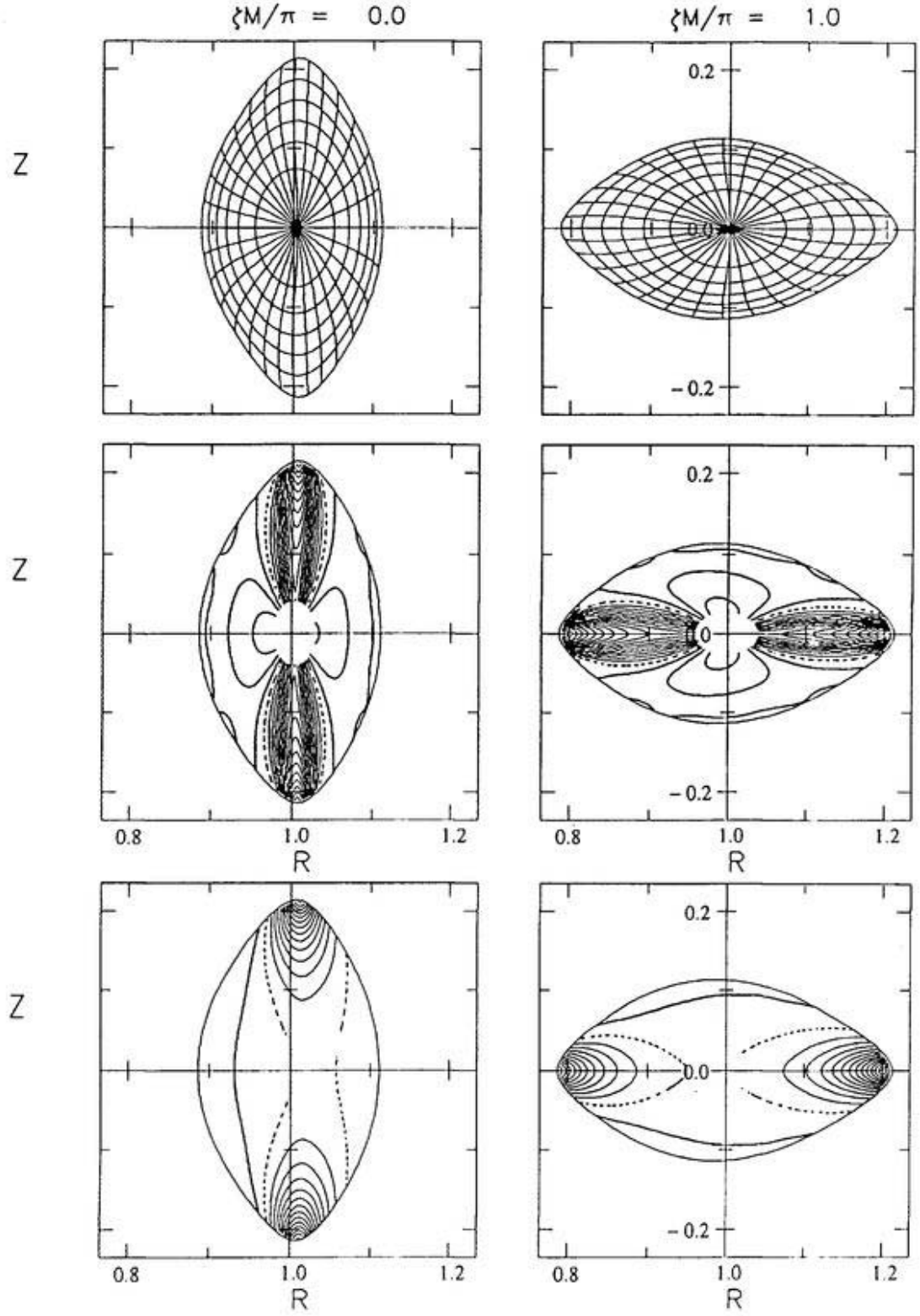

Figure 6.2 Local quantities for the vacuum configuration

(a) Equally spaced (ψ, θ) mesh,

(b) contours of the local magnetic shear $\hat{s}$,

(c) contours of the normal magnetic curvature multiplied by the Jacobian, $\sqrt{g}\kappa^n$,

on the vertically (1st column) and horizontally (2nd column) elongated poloidal cross sections. Thin (thick) curves in the contours of $\hat{s}$ indicate the negative (positive) regions. Thin and thick curves in the contours of $\sqrt{g}\kappa^n$ indicate the locally unfavorable (favorable) regions. The normal magnetic curvature is more unfavorable on the outside of the torus than on the inside of the torus.

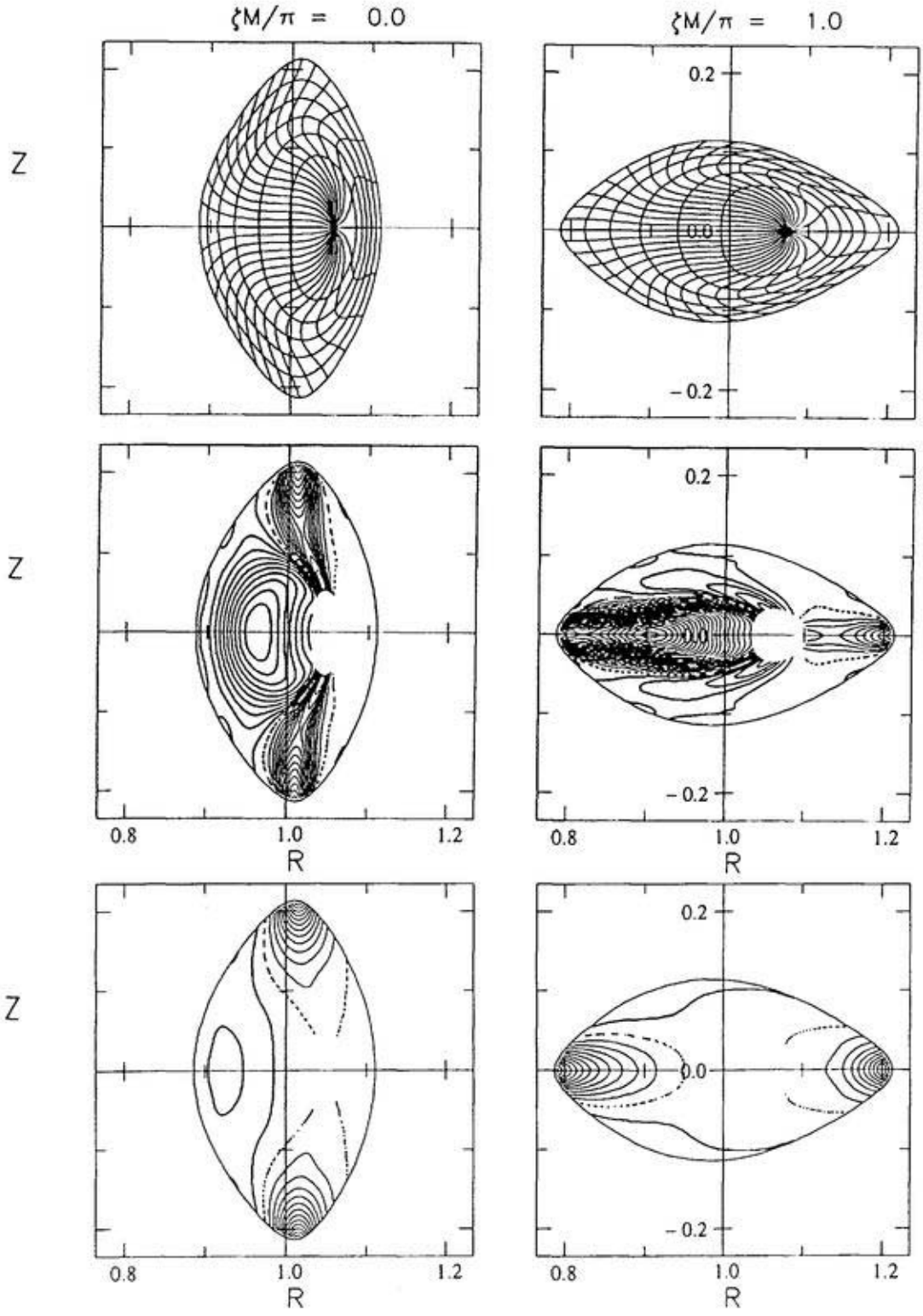

Figure 6.3 Local quantities for the toroidicity-dominant Mercier-unstable equilibrium with a relatively large Shafranov shift

Same quantities as in the vacuum configuration are drawn for the TDMULHD equilibrium. For each graph, the same contour level as one in Figure 6.2 is used. Compared with the vacuum configuration (Figure 6.2), the local magnetic shear $\hat{s}$ is strongly reduced on the outer side of the torus, especially at the horizontally (2nd column) elongated poloidal cross section. Note that the Shafranov shift makes the normal magnetic curvature to be more unfavorable on the inside of the torus than on the outside of the torus.

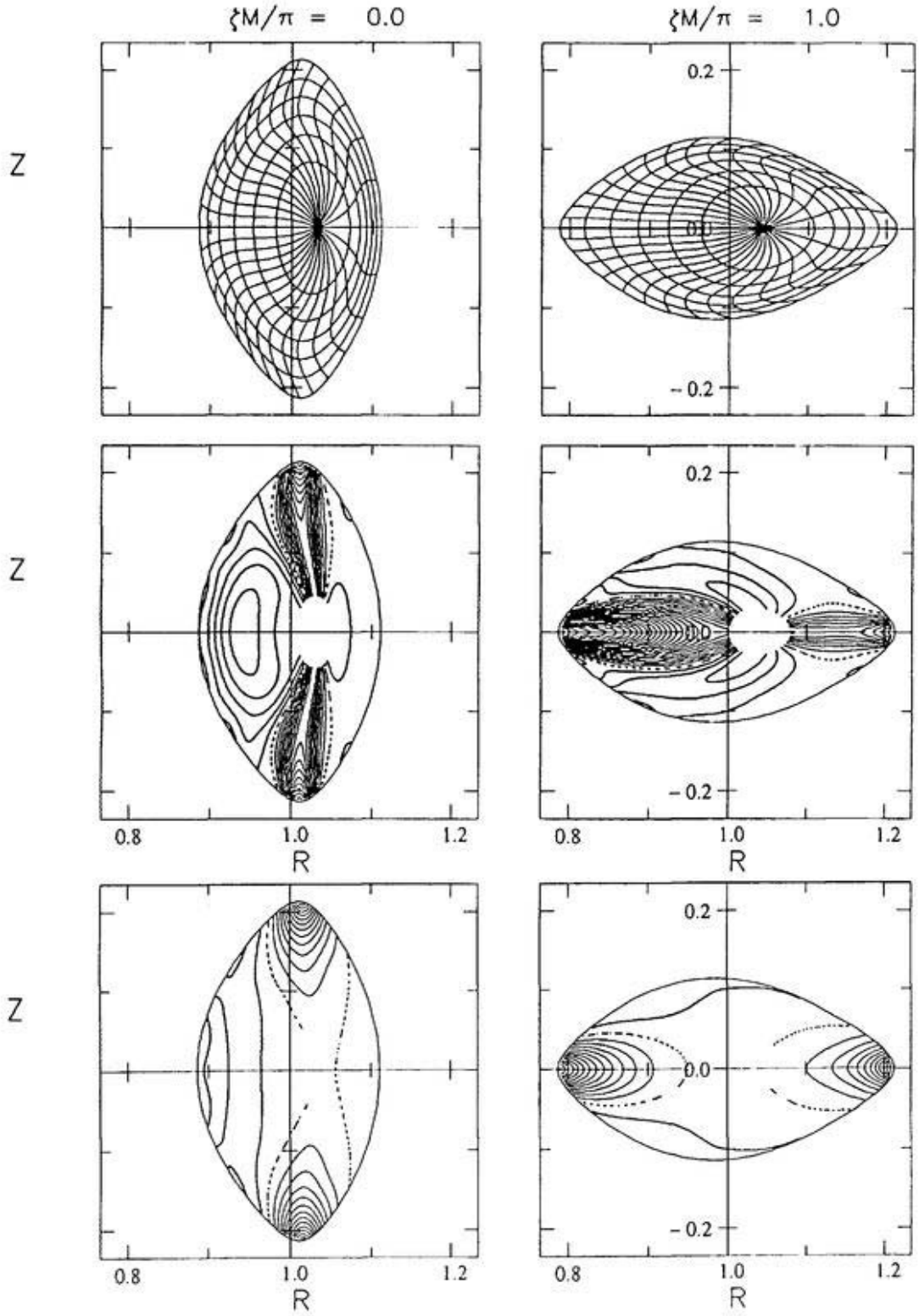

Figure 6.4 Local quantities for the helicity-dominant Mercier-unstable equilibrium with a relatively large Shafranov shift

Same quantities as in the vacuum configuration are drawn for the HDMULHD equilibrium. For each graph, the same contour level as one in Figure 6.2 is used. Compared with TDMULHD equilibrium shown in Figure 6.3, the reduction of the local magnetic shear $\hat{s}$ on the outer side of the torus is weaker. Just as in TDMULHD, the normal magnetic curvature is more unfavorable on the inside of the torus than on the outside of the torus, brought by the Shafranov shift.

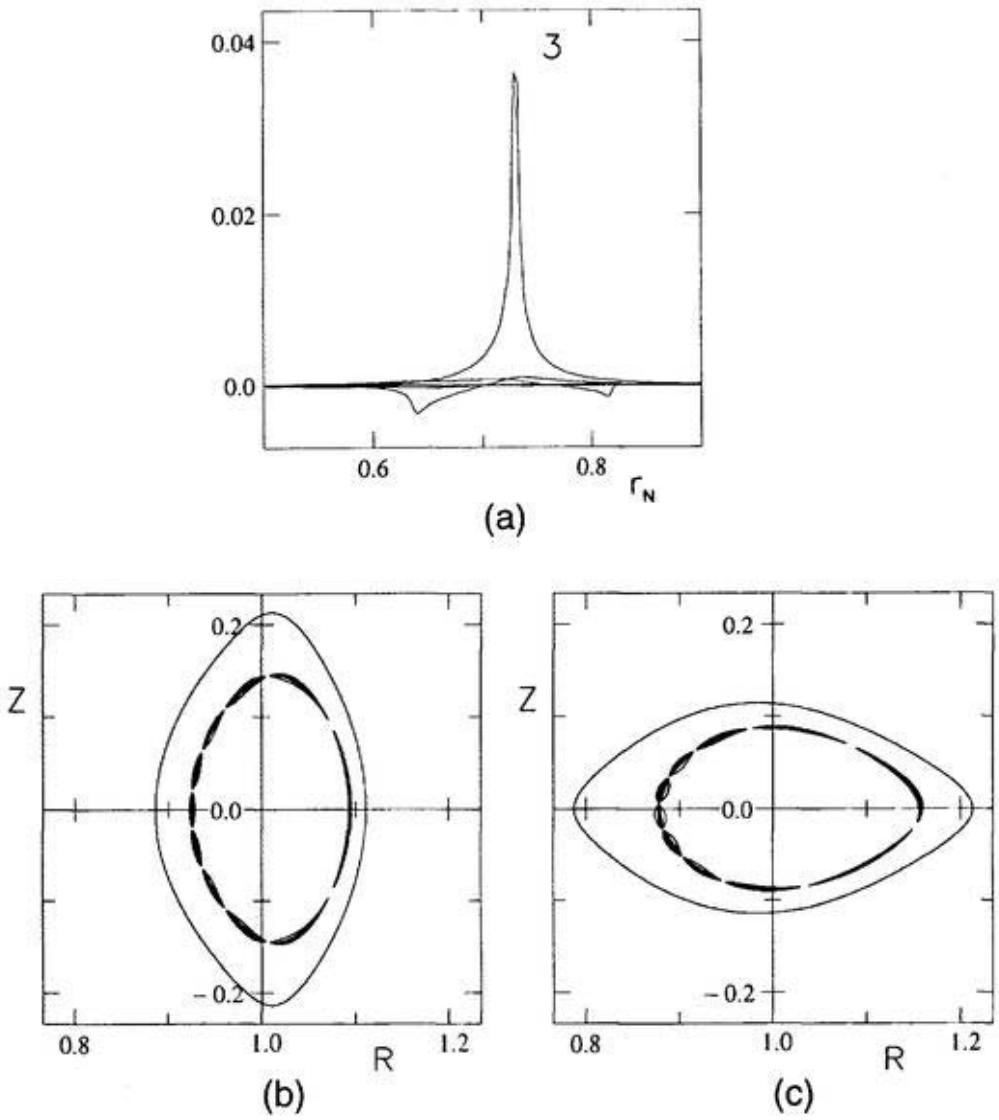

Figure 6.5. Interchange mode

$M_p = 5$, $N_p = 3$, $M_{eq} = 76$, $M_{pt} = 151$, $N_s = 240$
$\omega^2 = -4.9905E-5$

(a) radial profile of the Fourier component of the normal dispalcement with the origin of poloidal angle on the outer side of torus
(b) contour of perturbed pressure on the horizontally elongated poloidal cross section
(c) contour of perturbed pressure on the vertically elongated poloidal cross section

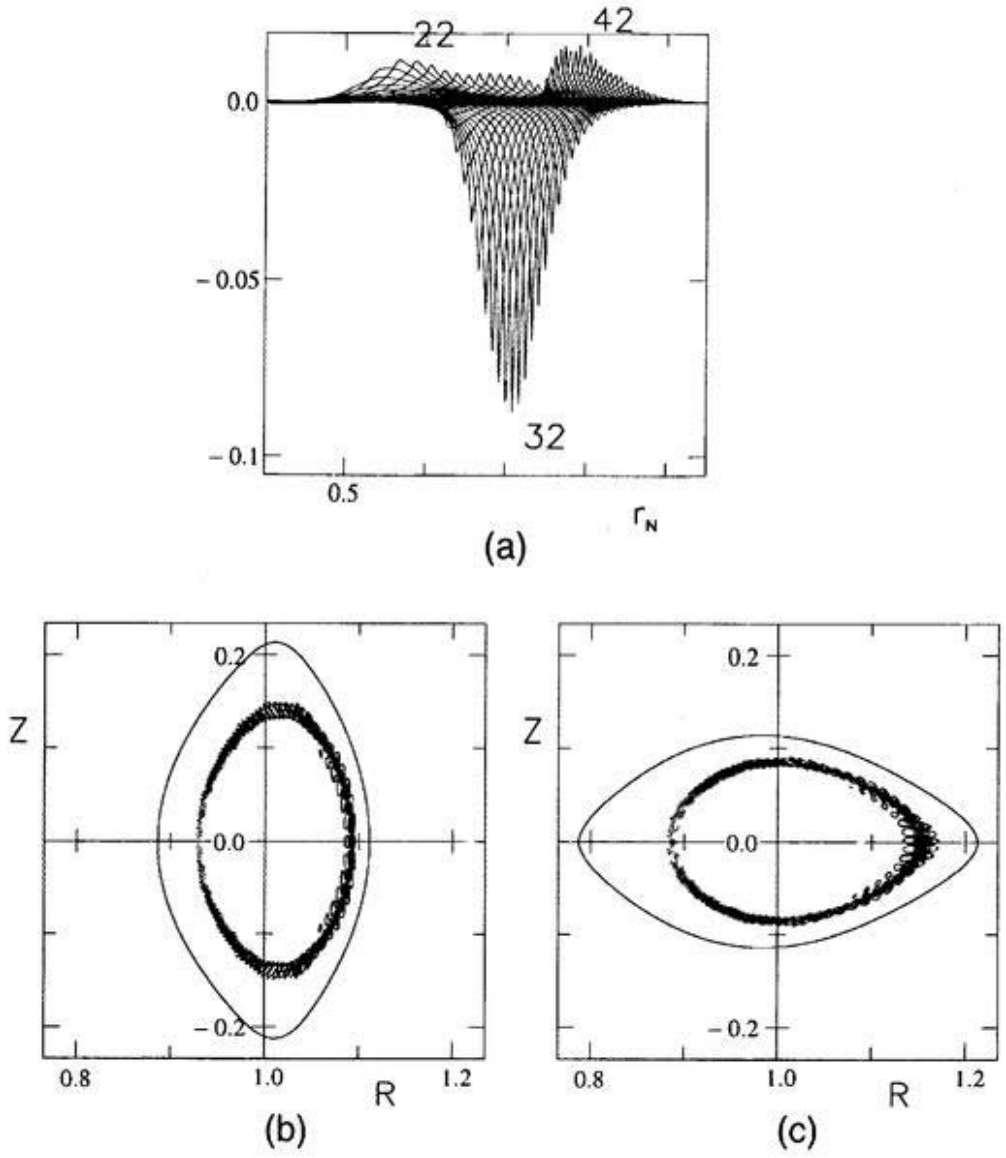

Figure 6.6 Tokamak-like ballooning mode

$M_p = 38,\quad N_p = 22,\quad M_{eq} = 186,\quad M_{pl} = 371,\quad N_s = 660$
$\omega^2 = -1.8895E-3$

(a) radial profile of the Fourier component of the normal dispalcement with the origin of poloidal angle on the outer side of torus

(b) contour of perturbed pressure on the horizontally elongated poloidal cross section

(c) contour of perturbed pressure on the vertically elongated poloidal cross section

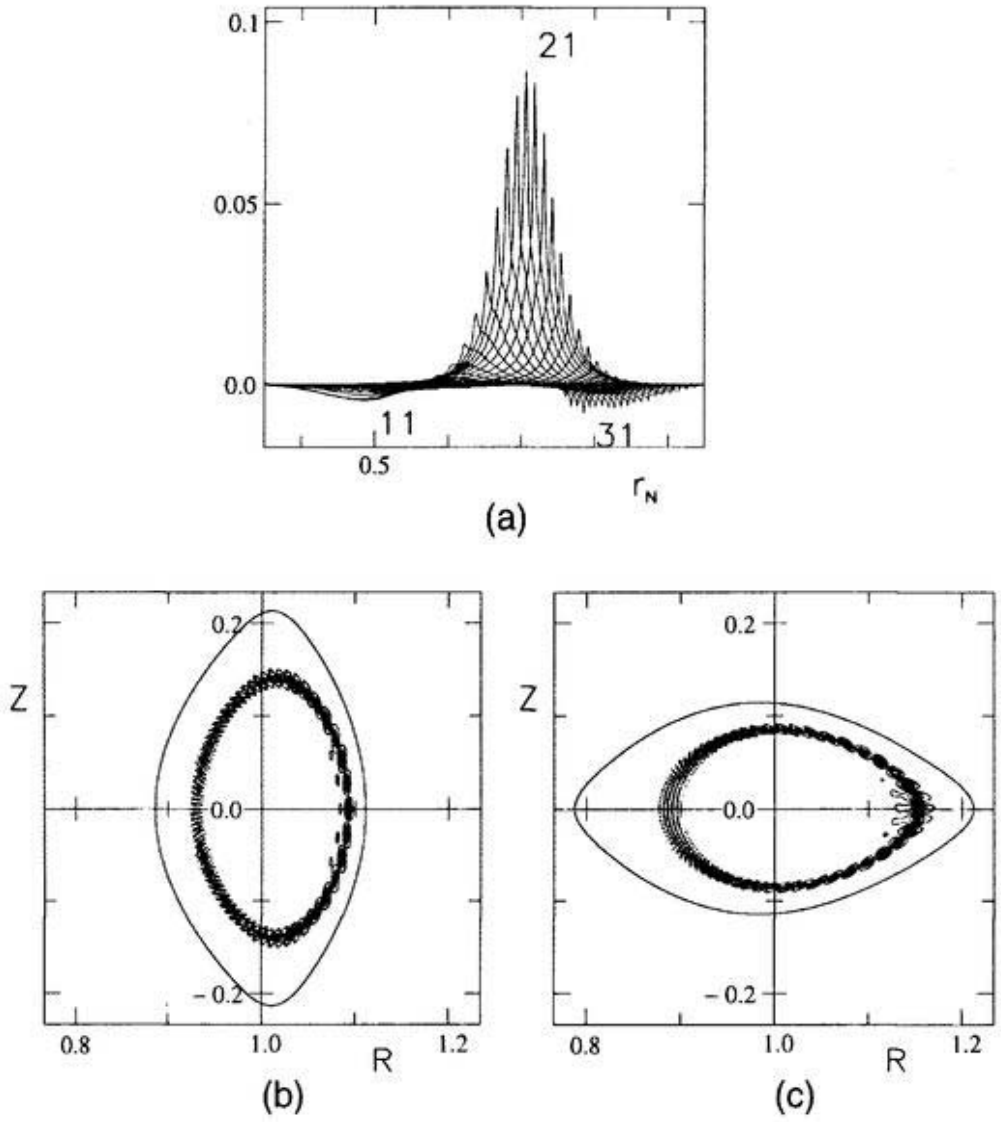

Figure 6.7 Tokamak-like ballooning mode

$M_p = 19$, $N_p = 11$, $M_{eq} = 186$, $M_{pt} = 371$, $N_s = 660$
$\omega^2 = -7.0367E-4$

(a) radial profile of the Fourier component of the normal dispalcement with the origin of poloidal angle on the outer side of torus
(b) contour of perturbed pressure on the horizontally elongated poloidal cross section
(c) contour of perturbed pressure on the vertically elongated poloidal cross section

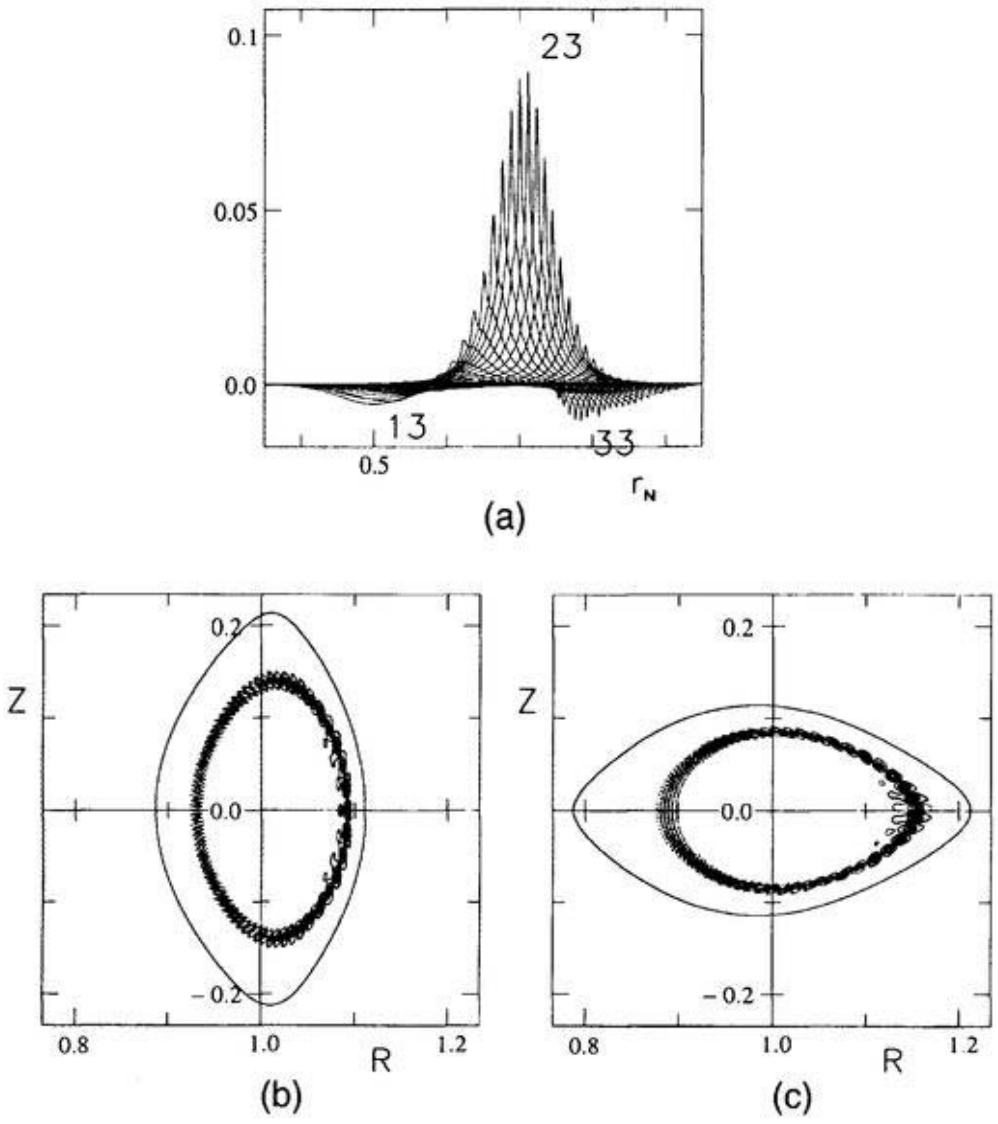

Figure 6.8 Tokamak-like ballooning mode

$M_p = 23,\ N_p = 13,\ M_{eq} = 186,\ M_{pt} = 371,\ N_s = 660$
$\omega^2 = -9.1904E-4$

(a) radial profile of the Fourier component of the normal dispalcement with the origin of poloidal angle on the outer side of torus
(b) contour of perturbed pressure on the horizontally elongated poloidal cross section
(c) contour of perturbed pressure on the vertically elongated poloidal cross section

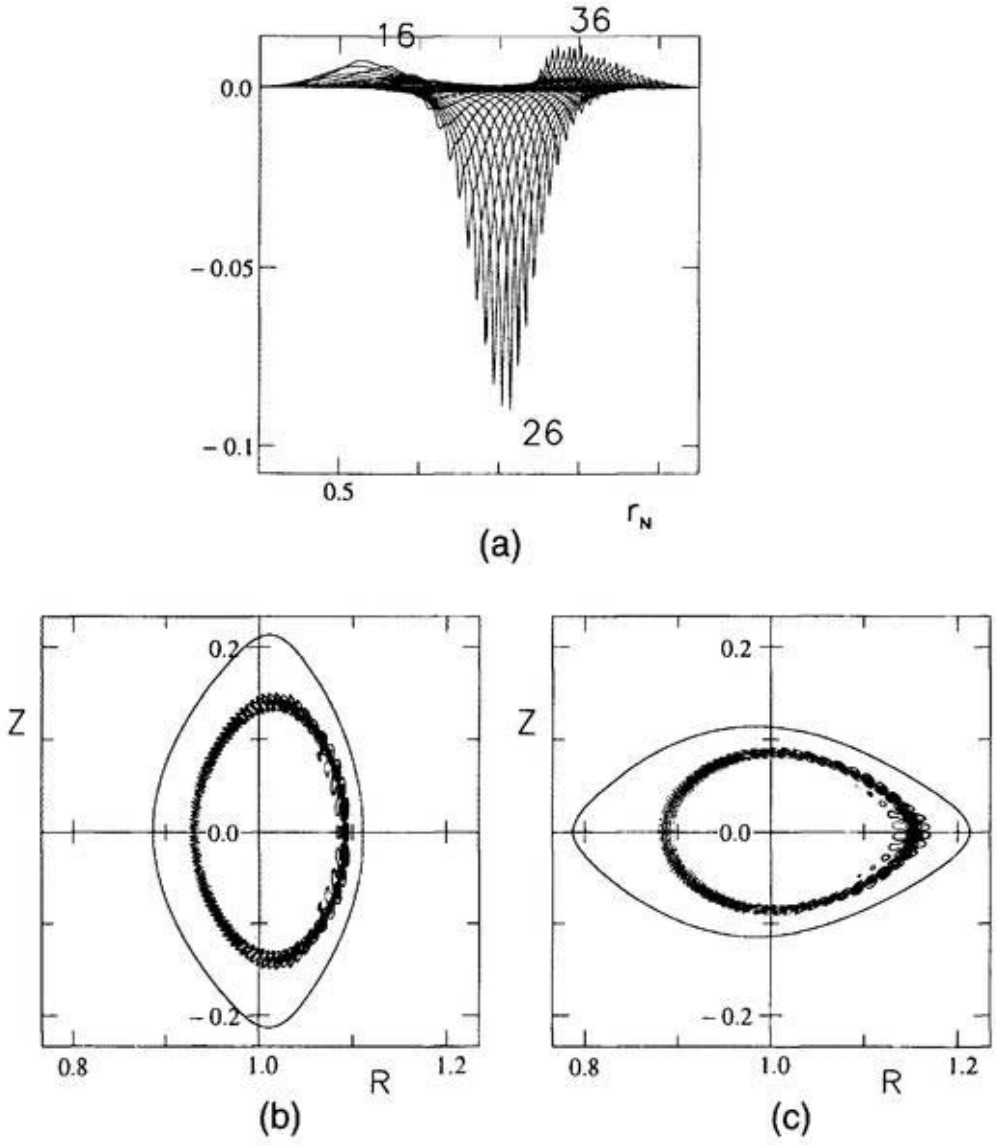

Figure 6.9 Tokamak-like ballooning mode

$M_p = 28$, $N_p = 16$, $M_{eq} = 186$, $M_{pt} = 371$, $N_s = 660$
$\omega^2 = -1.2638E-3$

(a) radial profile of the Fourier component of the normal dispalcement with the origin of poloidal angle on the outer side of torus
(b) contour of perturbed pressure on the horizontally elongated poloidal cross section
(c) contour of perturbed pressure on the vertically elongated poloidal cross section

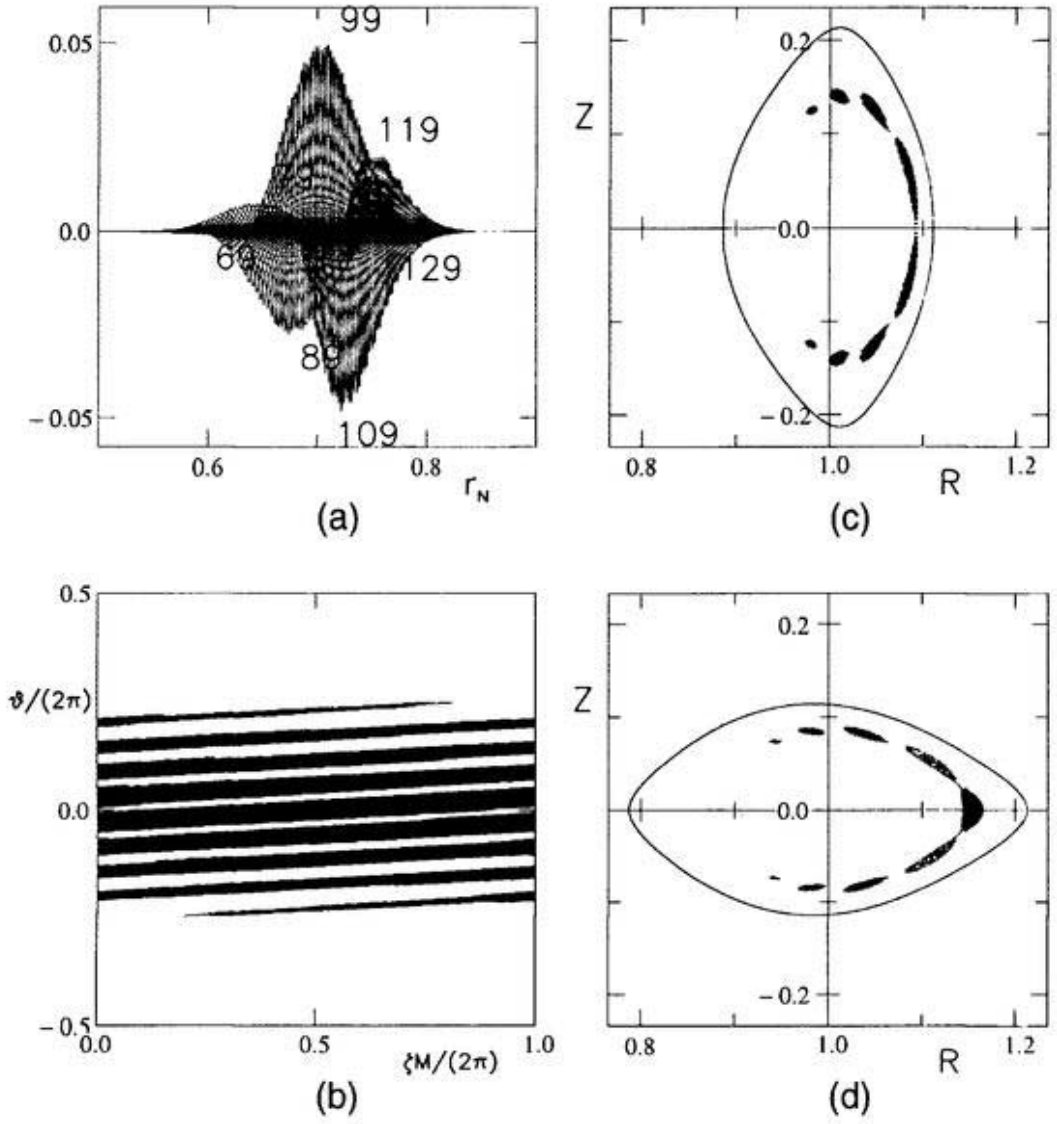

Figure 6.10 Ballooning mode inherent to 3-D systems

$M_p=171,\quad N_p=99,\quad M_{eq}=336,\quad M_{pt}=671,\quad N_s=960$
$\omega^2 = -6.2171E-3$

(a) radial profile of the Fourier component of the normal dispalcement with the origin of poloidal angle on the outer side of torus
(b) contour of perturbed pressure on the (ϑ, ζ) plane at $r_N = 0.710$
(c) contour of perturbed pressure on the vertically elongated poloidal cross section
(d) contour of perturbed pressure on the horizontally elongated poloidal cross section

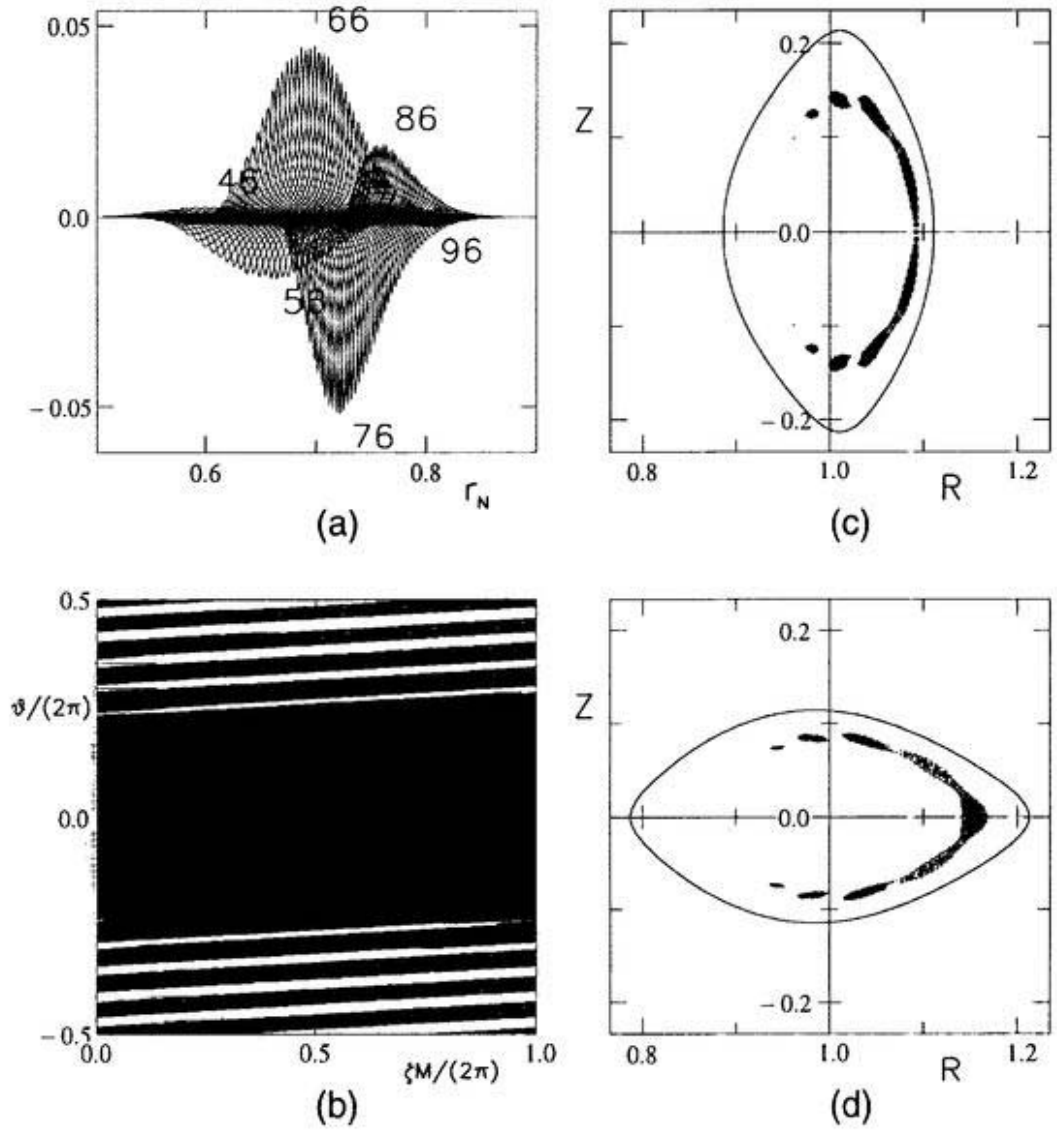

Figure 6.11 Ballooning mode inherent to 3-D systems

$M_p=114$, $N_p=66$, $M_{eq}=336$, $M_{pl}=671$, $N_s=960$
$\omega^2 = -5.0501E-3$

(a) radial profile of the Fourier component of the normal dispalcement with the origin of poloidal angle on the outer side of torus
(b) contour of perturbed pressure on the (ϑ, ζ) plane at $r_N = 0.699$
(c) contour of perturbed pressure on the vertically elongated poloidal cross section
(d) contour of perturbed pressure on the horizontally elongated poloidal cross section

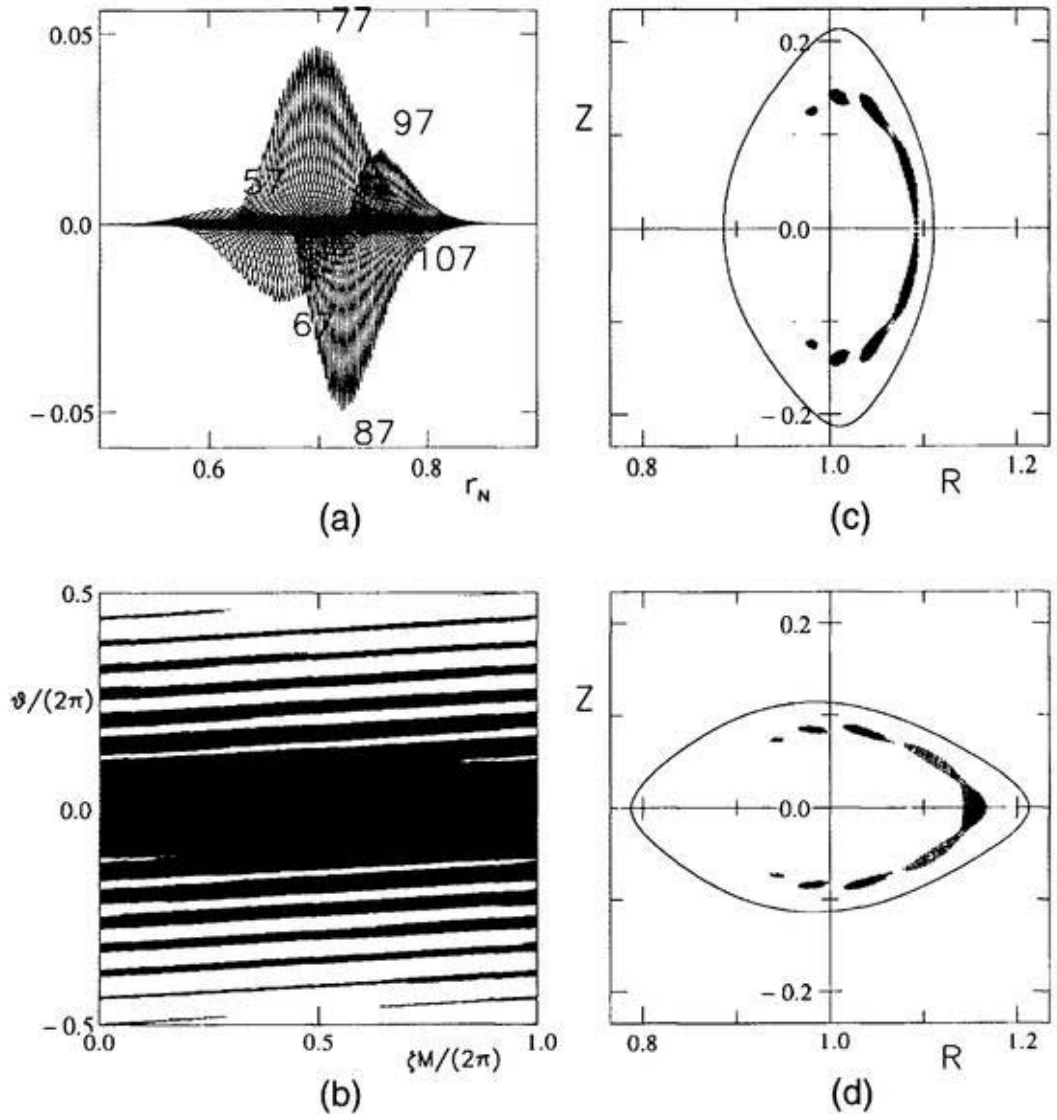

Figure 6.12 Ballooning mode inherent to 3-D systems

$M_p=133,\quad N_p=77,\quad M_{eq}=336,\quad M_{pt}=671,\quad N_s=960$
$\omega^2 = -5.5105E-3$

(a) radial profile of the Fourier component of the normal dispalcement with the origin of poloidal angle on the outer side of torus
(b) contour of perturbed pressure on the (ϑ, ζ) plane at $r_N = 0.701$
(c) contour of perturbed pressure on the vertically elongated poloidal cross section
(d) contour of perturbed pressure on the horizontally elongated poloidal cross section

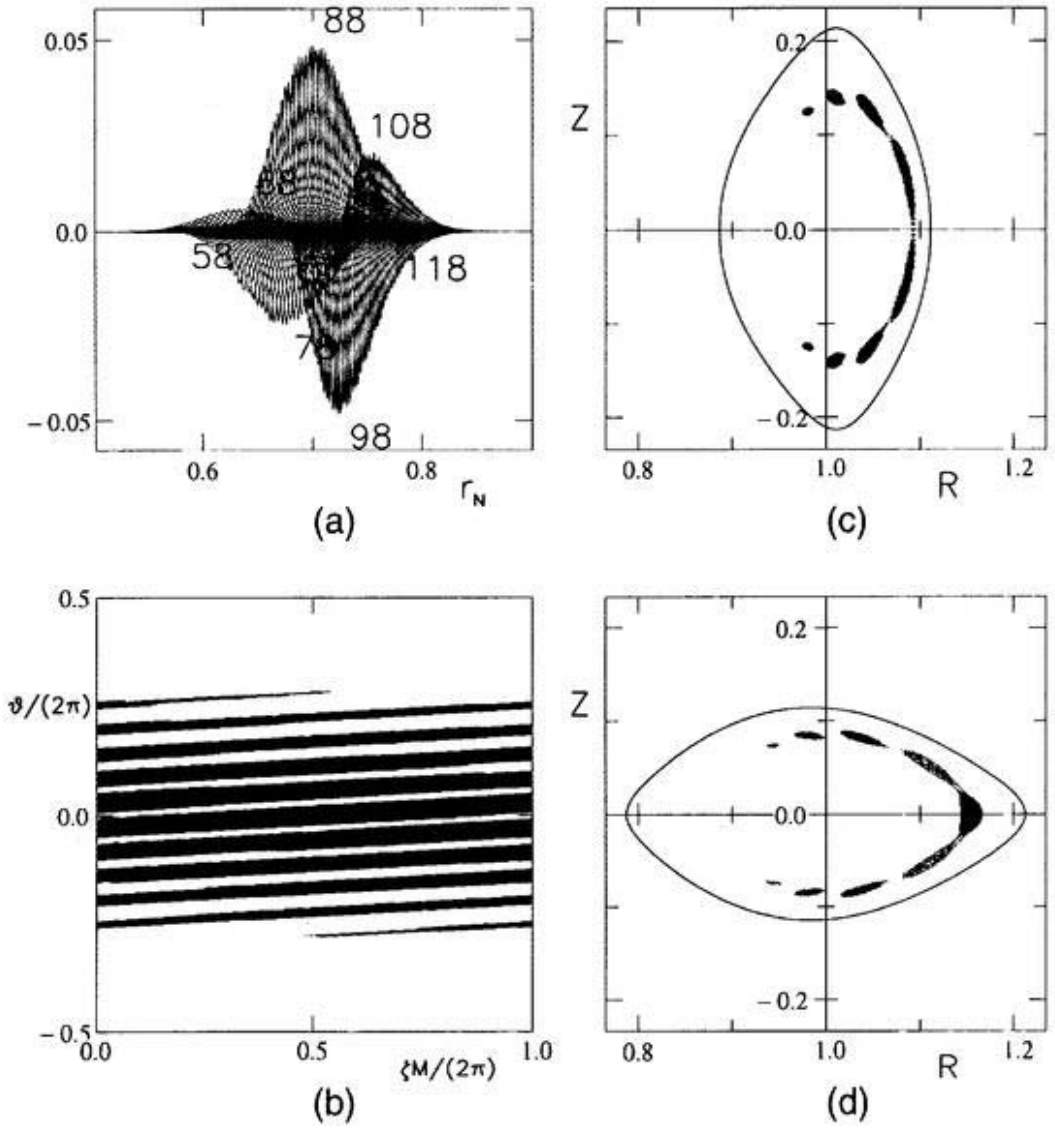

Figure 6.13 Ballooning mode inherent to 3-D systems

$M_p=152,\ N_p=88,\ M_{eq}=336,\ M_{pt}=671,\ N_s=960$
$\omega^2 = -5.8910E-3$

(a) radial profile of the Fourier component of the normal dispalcement with the origin of poloidal angle on the outer side of torus
(b) contour of perturbed pressure on the (ϑ, ζ) plane at $r_N = 0.699$
(c) contour of perturbed pressure on the vertically elongated poloidal cross section
(d) contour of perturbed pressure on the horizontally elongated poloidal cross section

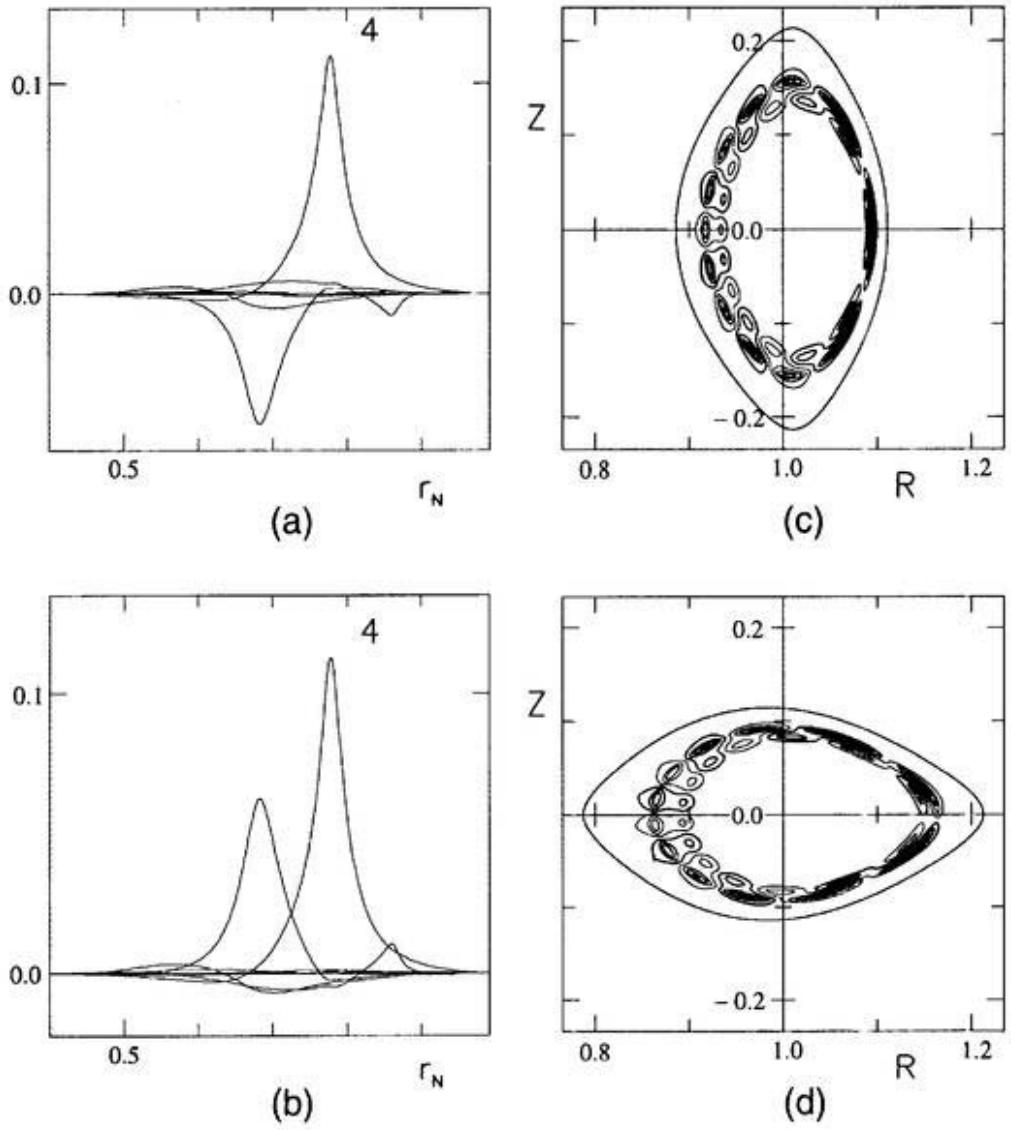

Figure 6.14 Interchange mode

$M_p = 7,\ N_p = 4,\ M_{eq} = 62,\ M_{pt} = 123,\ N_s = 300$
$\omega^2 = -3.0704E-3$

(a) radial profile of the Fourier component of the normal dispalcement with the origin of poloidal angle on the outer side of torus
(b) same quantity, with the origin of poloidal angle on the inner side of torus
(c) contour of perturbed pressure on the vertically elongated poloidal cross section
(d) contour of perturbed pressure on the horizontally elongated poloidal cross section

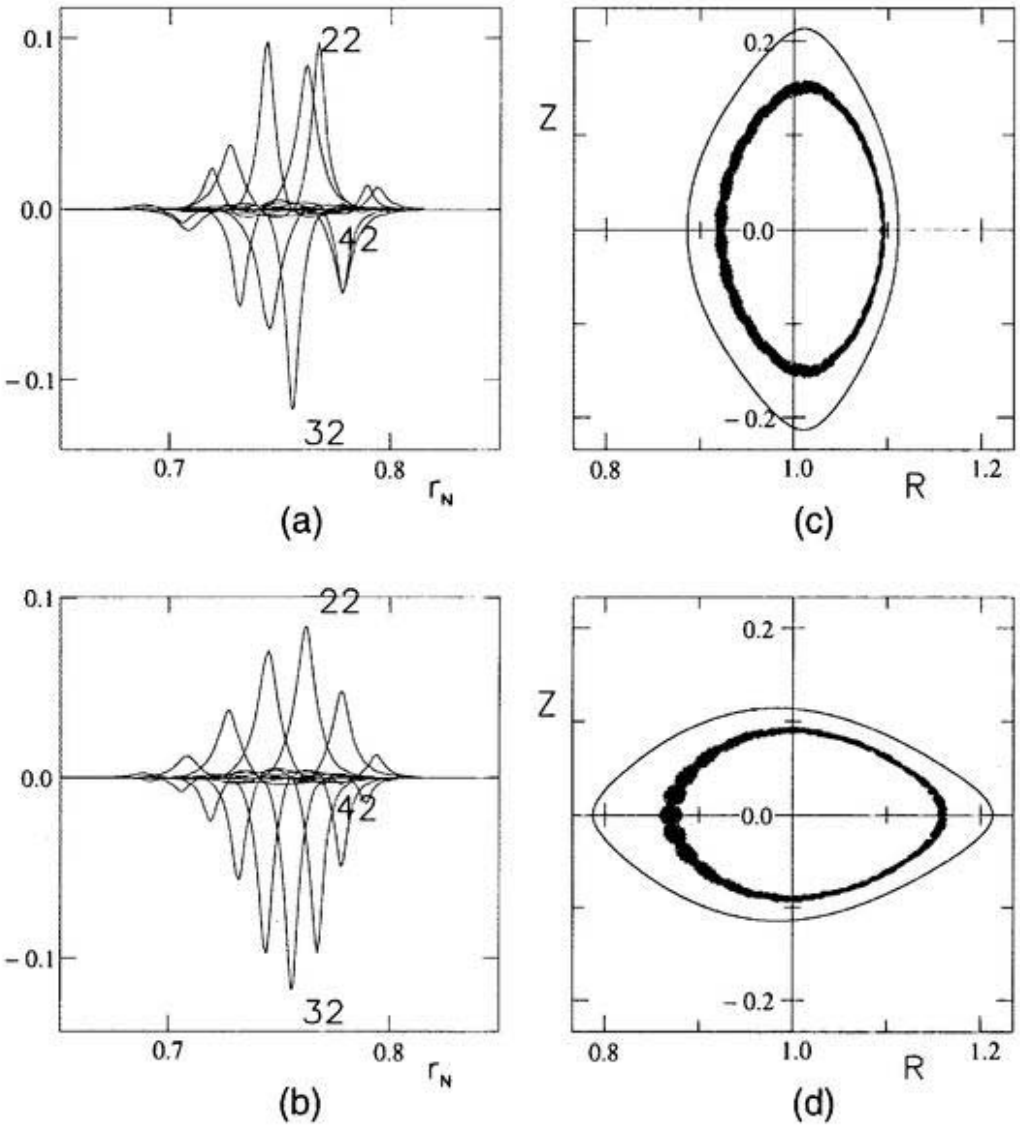

Figure 6.15 Interchange mode

$M_p = 38,\quad N_p = 22,\quad M_{eq} = 186,\quad M_{pl} = 371,\quad N_s = 660$
$\omega^2 = -5.2634E-3$

(a) radial profile of the Fourier component of the normal dispalcement with the origin of poloidal angle on the outer side of torus
(b) same quantity, with the origin of poloidal angle on the inner side of torus
(c) contour of perturbed pressure on the vertically elongated poloidal cross section
(d) contour of perturbed pressure on the horizontally elongated poloidal cross section

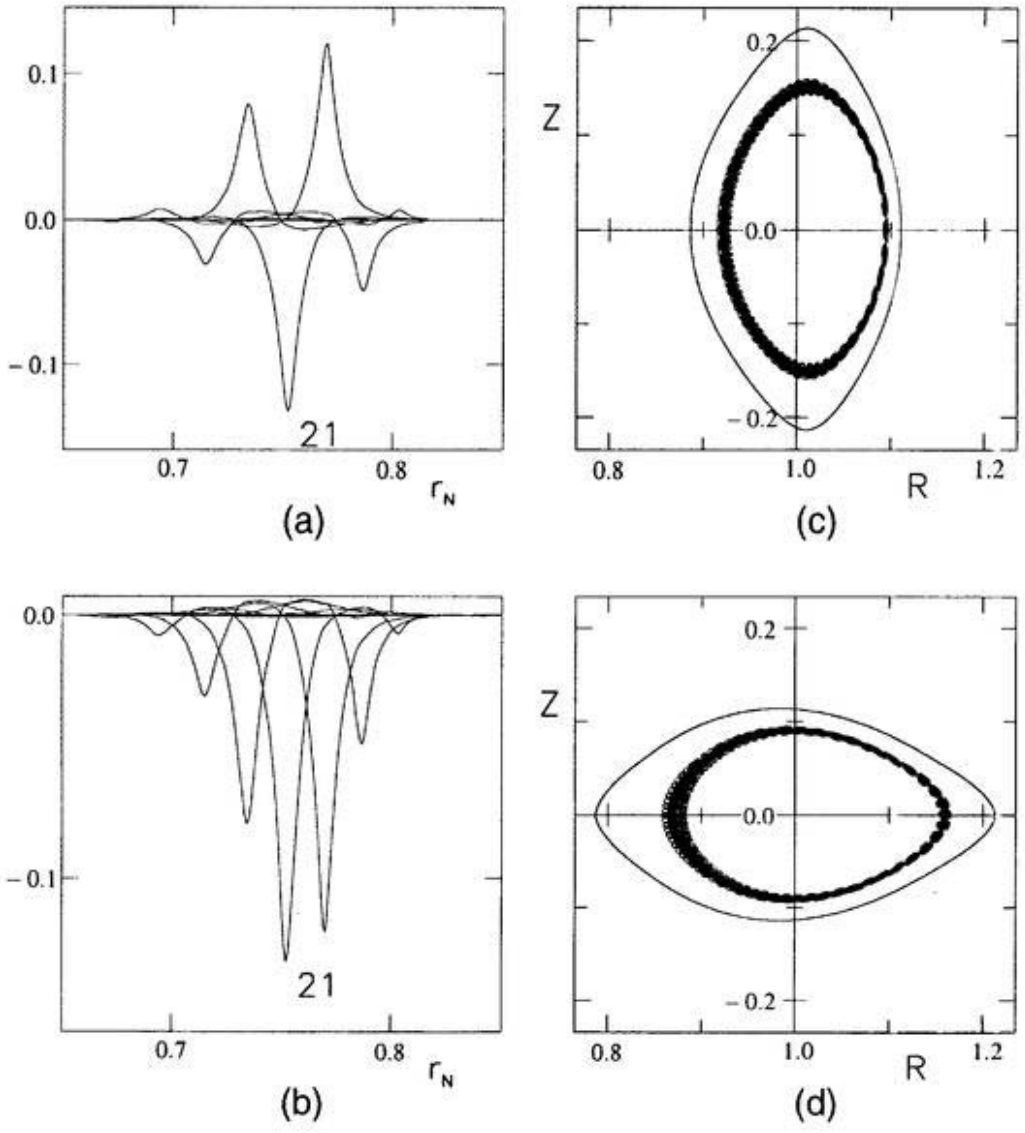

Figure 6.16 Interchange mode

$M_p = 19,\ N_p = 11,\ M_{eq} = 186,\ M_{pt} = 371,\ N_s = 660$
$\omega^2 = -5.2092E-3$

(a) radial profile of the Fourier component of the normal dispalcement with the origin of poloidal angle on the outer side of torus
(b) same quantity, with the origin of poloidal angle on the inner side of torus
(c) contour of perturbed pressure on the vertically elongated poloidal cross section
(d) contour of perturbed pressure on the horizontally elongated poloidal cross section

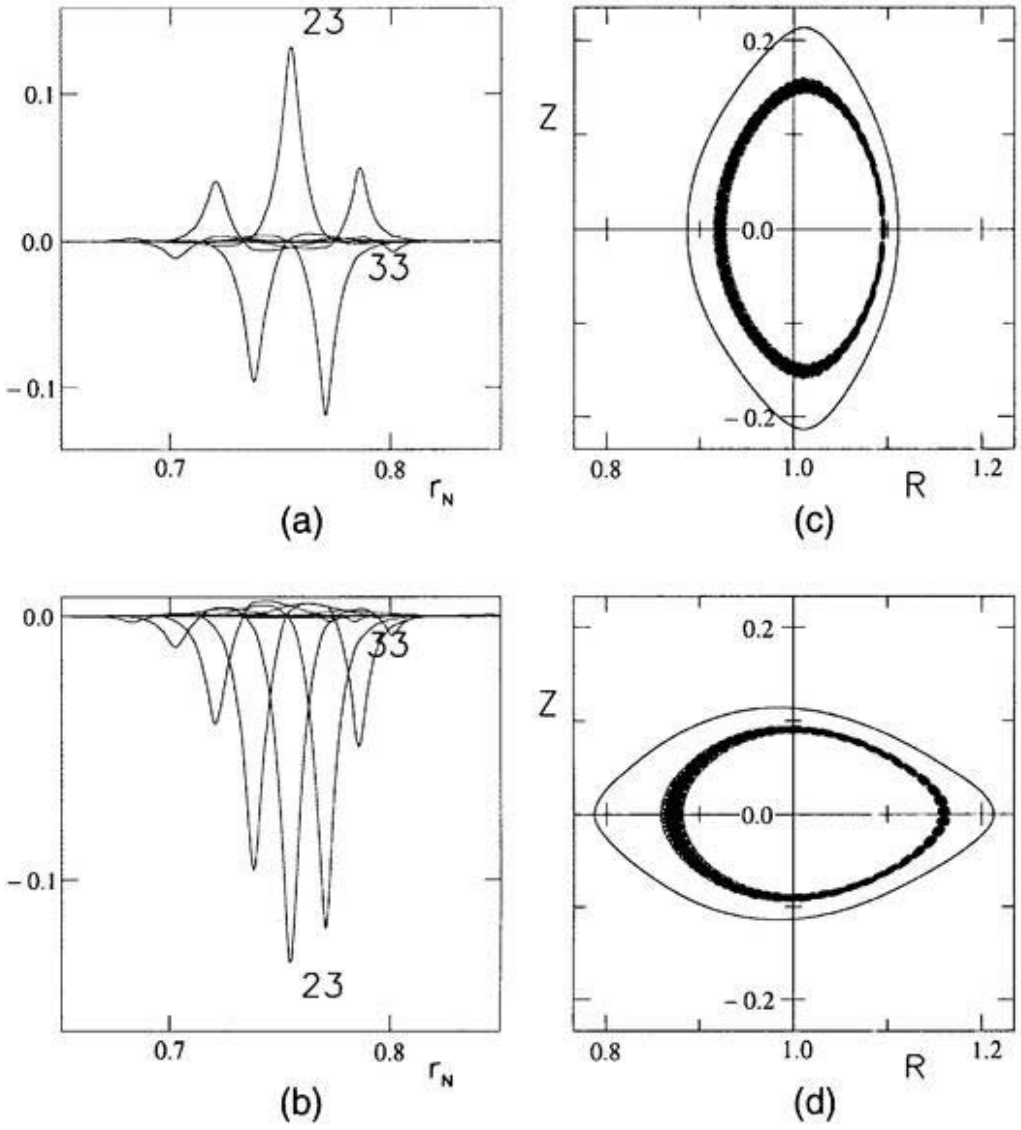

Figure 6.17 Interchange mode

$M_p = 23$, $N_p = 13$, $M_{eq} = 186$, $M_{pt} = 371$, $N_s = 660$
$\omega^2 = -5.2529E-3$

(a) radial profile of the Fourier component of the normal dispalcement with the origin of poloidal angle on the outer side of torus
(b) same quantity, with the origin of poloidal angle on the inner side of torus
(c) contour of perturbed pressure on the vertically elongated poloidal cross section
(d) contour of perturbed pressure on the horizontally elongated poloidal cross section

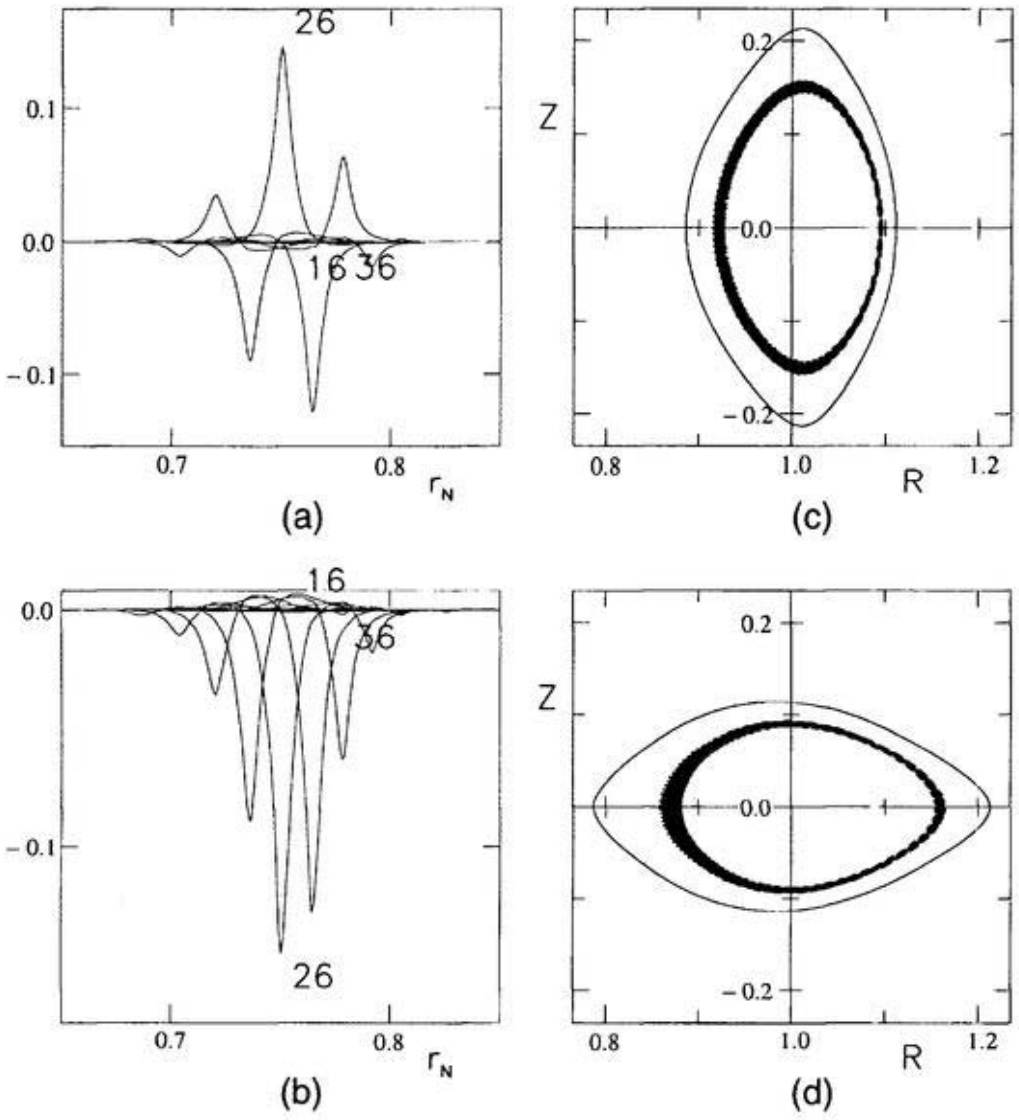

Figure 6.18 Interchange mode

$M_p = 28,\ N_p = 16,\ M_{eq} = 186,\ M_{pt} = 371,\ N_s = 660$
$\omega^2 = -5.3064E-3$

(a) radial profile of the Fourier component of the normal dispalcement with the origin of poloidal angle on the outer side of torus
(b) same quantity, with the origin of poloidal angle on the inner side of torus
(c) contour of perturbed pressure on the vertically elongated poloidal cross section
(d) contour of perturbed pressure on the horizontally elongated poloidal cross section

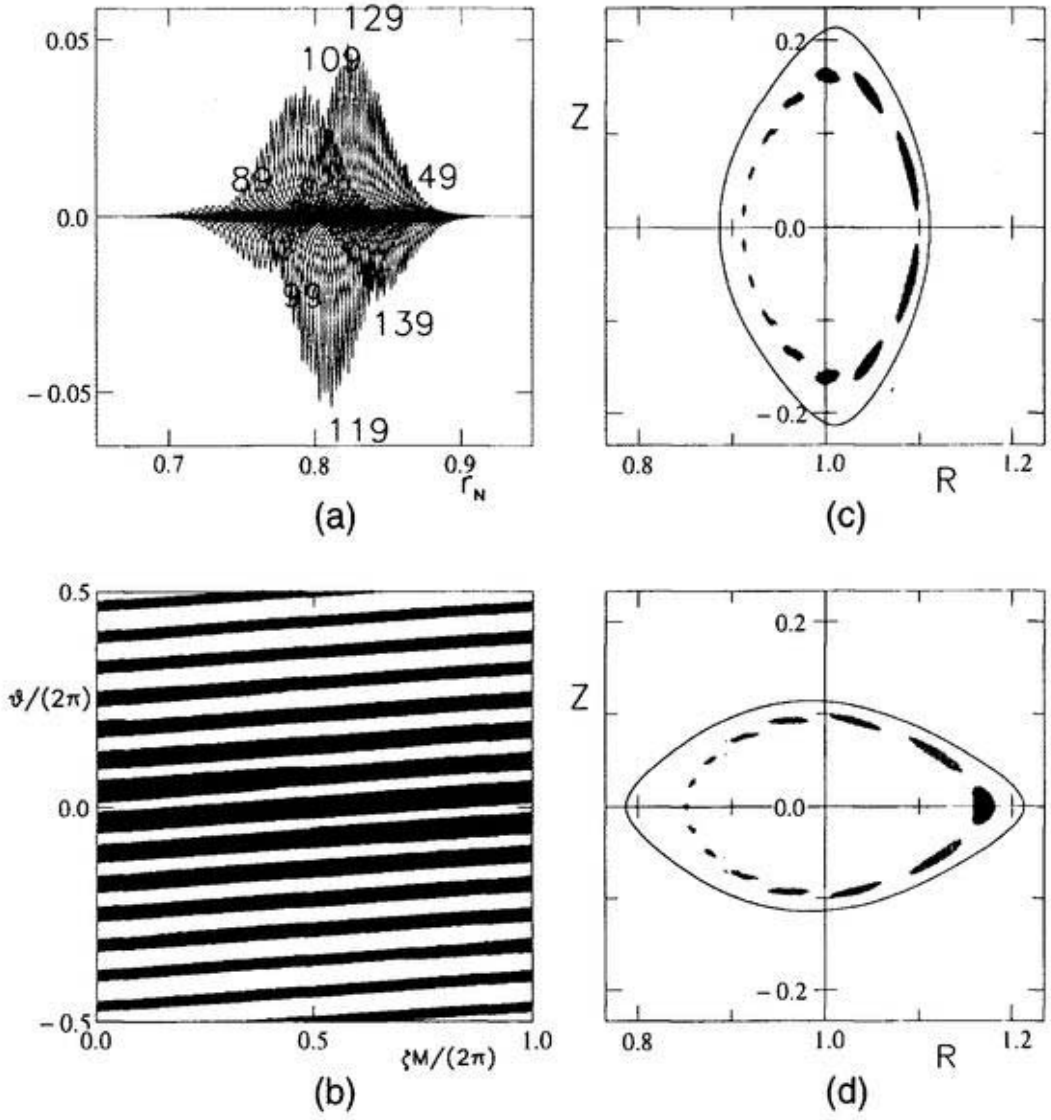

Figure 6.19 Ballooning mode inherent to 3-D systems

$M_p=171,\quad N_p=99,\quad M_{eq}=336,\quad M_{pl}=671,\quad N_s=1380$
$\omega^2 = -6.8826E-3$

(a) radial profile of the Fourier component of the normal dispalcement with the origin of poloidal angle on the outer side of torus

(b) contour of perturbed pressure on the (ϑ, ζ) plane at $r_N = 0.812$

(c) contour of perturbed pressure on the vertically elongated poloidal cross section

(d) contour of perturbed pressure on the horizontally elongated poloidal cross section

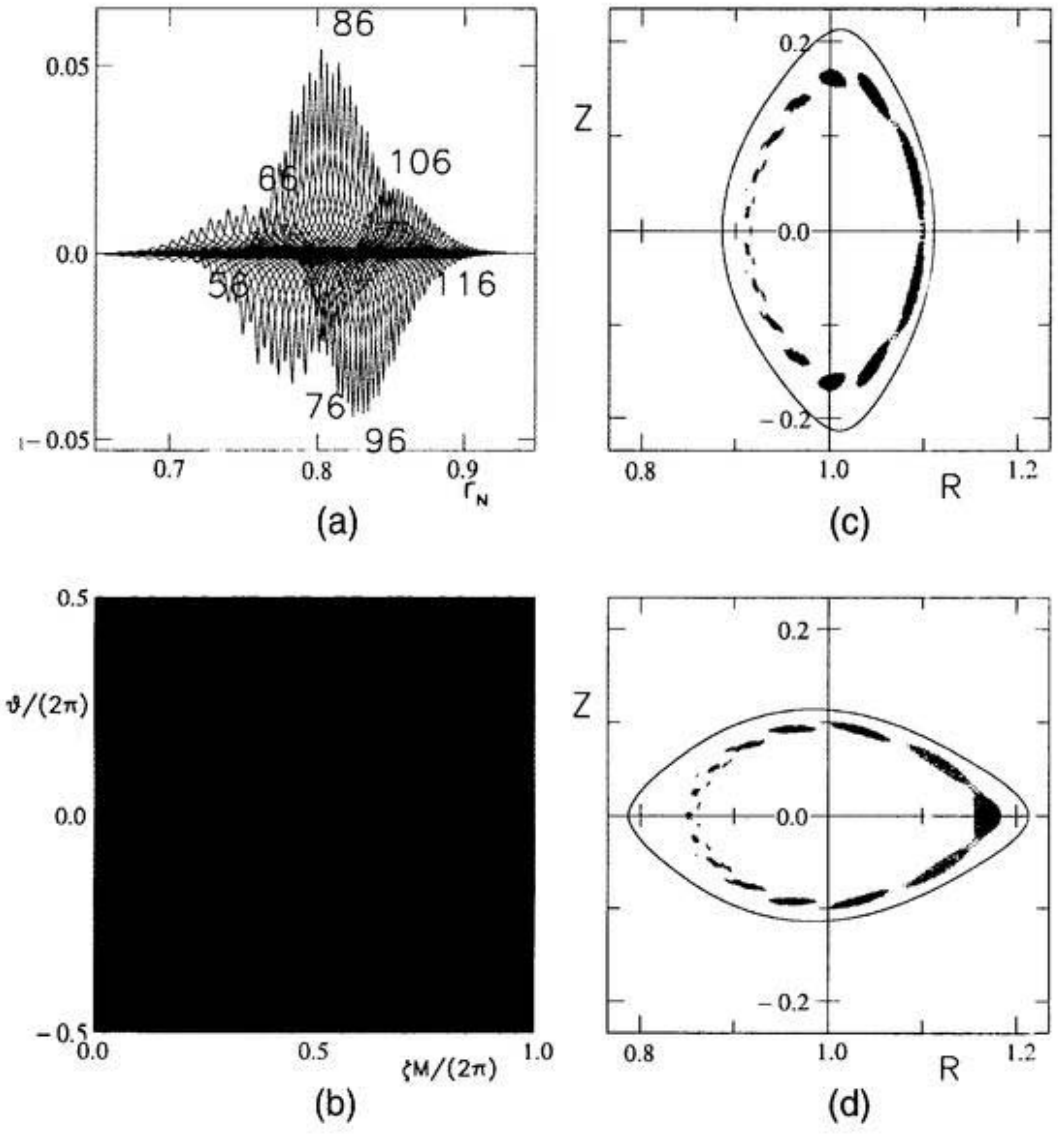

Figure 6.20 Ballooning mode inherent to 3-D systems

$M_p=114$, $N_p=66$, $M_{eq}=336$, $M_{pt}=671$, $N_s=1380$
$\omega^2 = -6.1566E-3$

(a) radial profile of the Fourier component of the normal dispalcement with the origin of poloidal angle on the outer side of torus
(b) contour of perturbed pressure on the (ϑ, ζ) plane at $r_N = 0.802$
(c) contour of perturbed pressure on the vertically elongated poloidal cross section
(d) contour of perturbed pressure on the horizontally elongated poloidal cross section

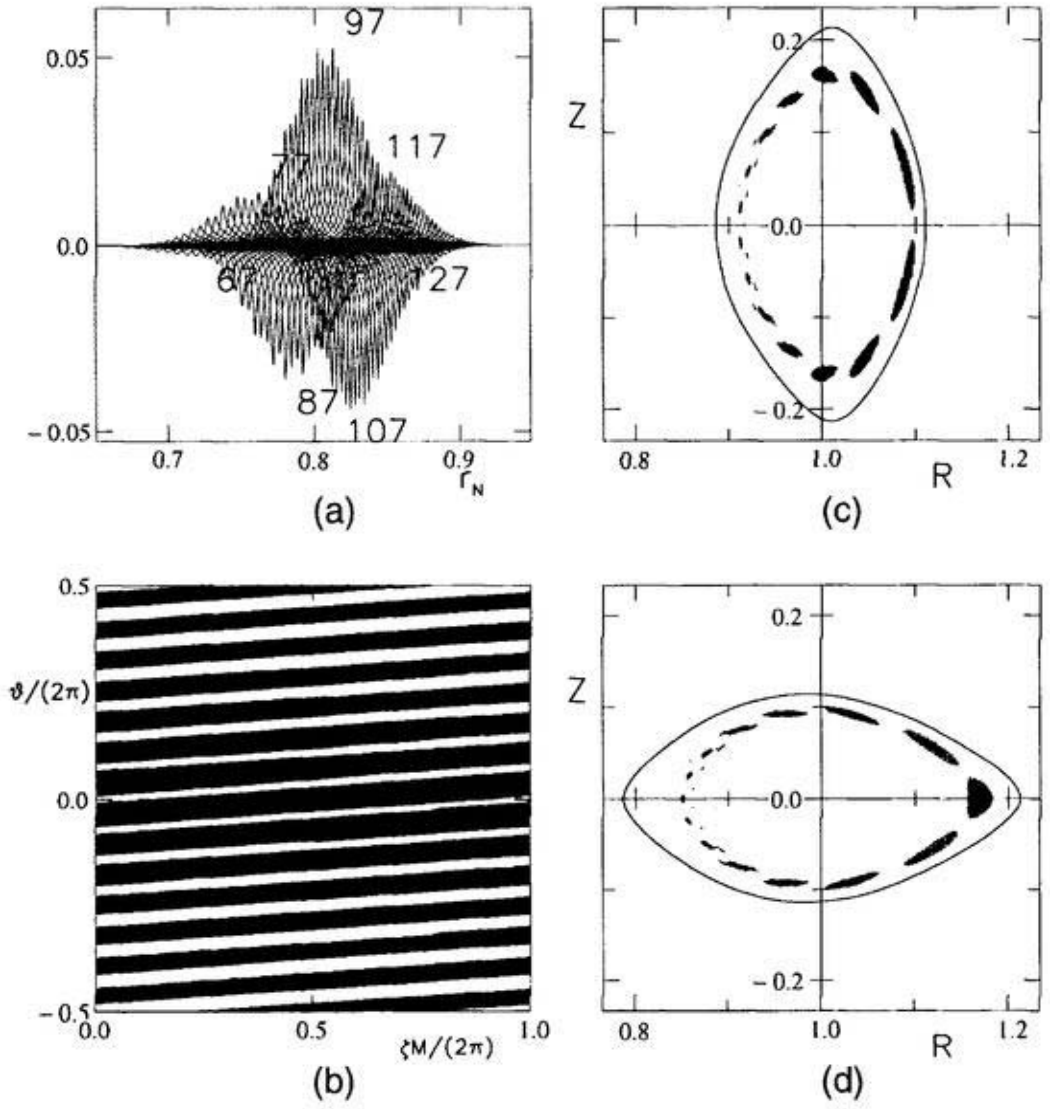

Figure 6.21 Ballooning mode inherent to 3-D systems

$M_p=133,\quad N_p=77,\quad M_{eq}=336,\quad M_{pl}=671,\quad N_s=1380$
$\omega^2 = -6.4494E-3$

(a) radial profile of the Fourier component of the normal dispalcement with the origin of poloidal angle on the outer side of torus

(b) contour of perturbed pressure on the (ϑ, ζ) plane at $r_N = 0.812$

(c) contour of perturbed pressure on the vertically elongated poloidal cross section

(d) contour of perturbed pressure on the horizontally elongated poloidal cross section

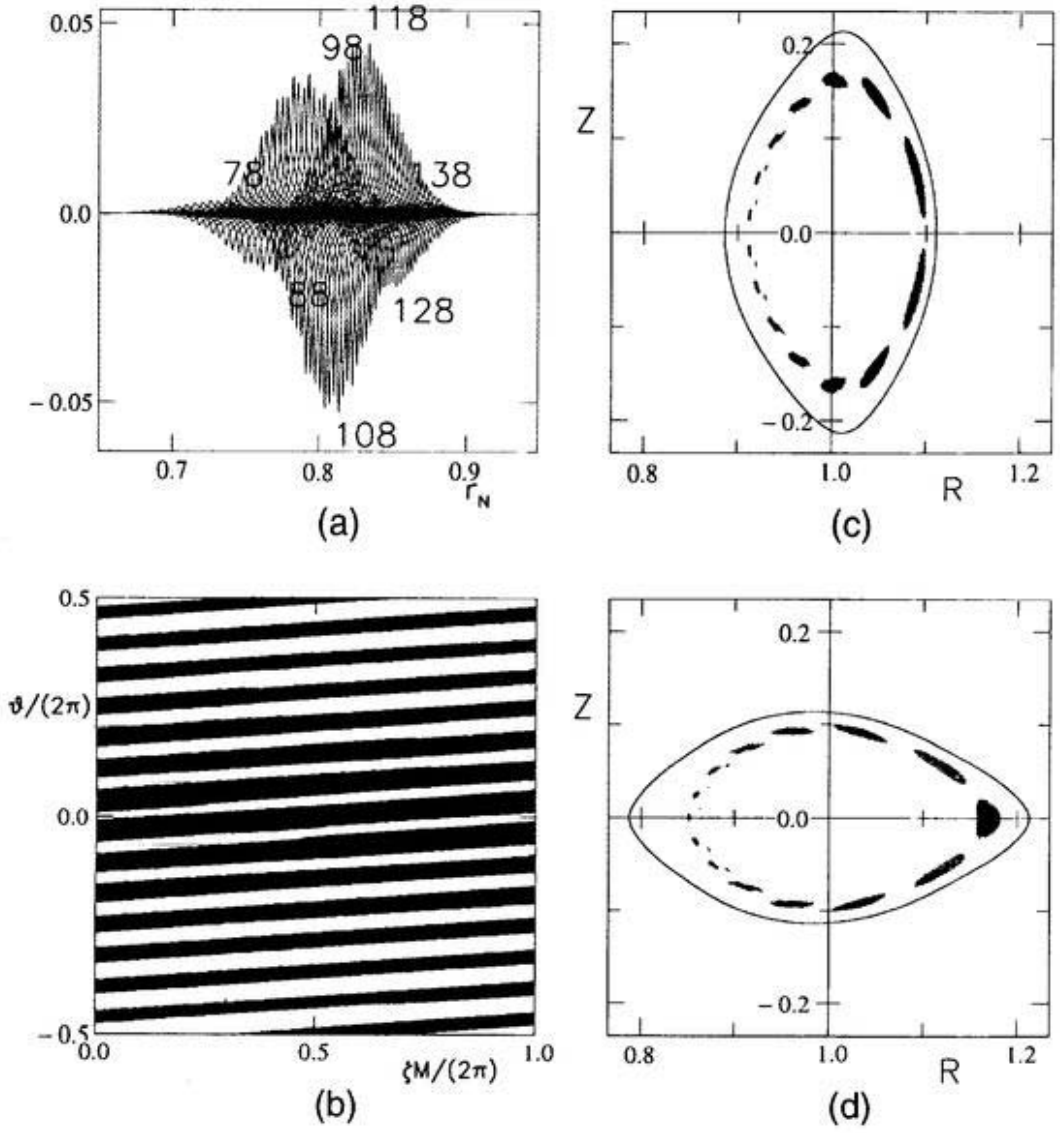

Figure 6.22 Ballooning mode inherent to 3-D systems

$M_p=152,\quad N_p=88,\quad M_{eq}=336,\quad M_{pl}=671,\quad N_s=1380$
$\omega^2 = -6.6775E-3$

(a) radial profile of the Fourier component of the normal dispalcement with the origin of poloidal angle on the outer side of torus

(b) contour of perturbed pressure on the (ϑ, ζ) plane at $r_N = 0.814$

(c) contour of perturbed pressure on the vertically elongated poloidal cross section

(d) contour of perturbed pressure on the horizontally elongated poloidal cross section

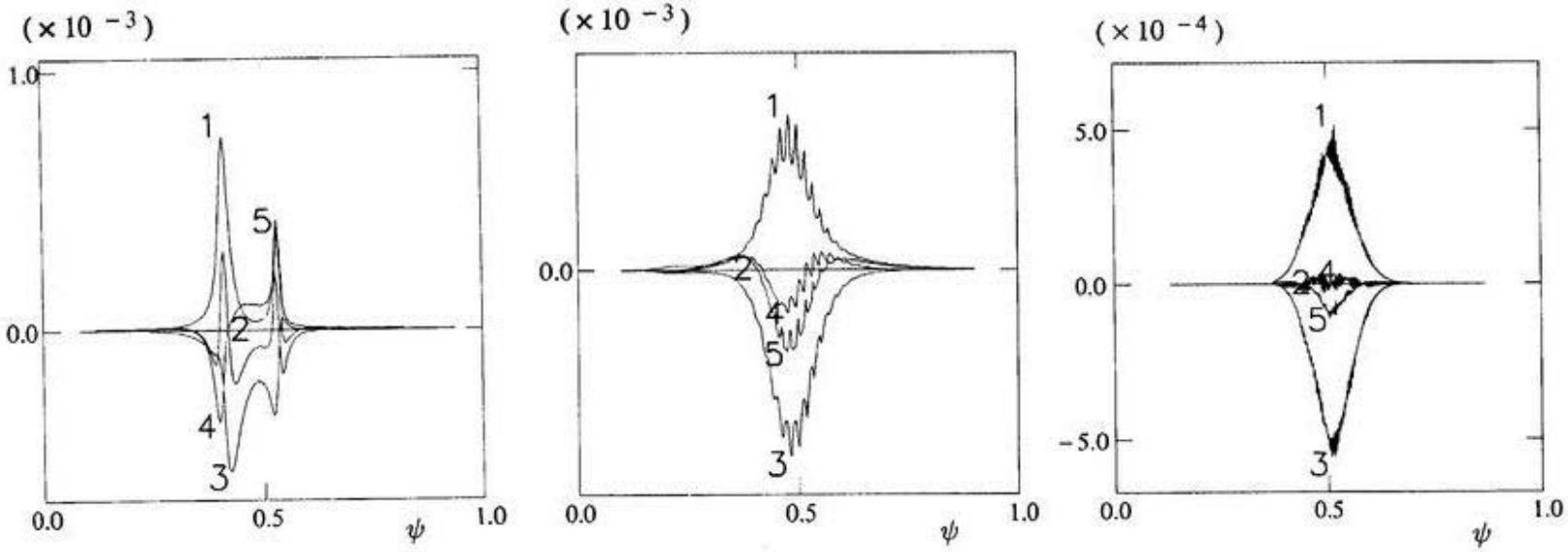

(a) (b) (c)

Figure 6.23 Contributions to the energy integral from

(a) an interchange mode with low toroidal mode number $n < M$,
(b) a tokamak-like ballooning mode with moderate toroidal mode number $n \sim M$,
(c) a ballooning mode inherent to 3-D systems with fairly high toroidal mode number $n \gg M$.

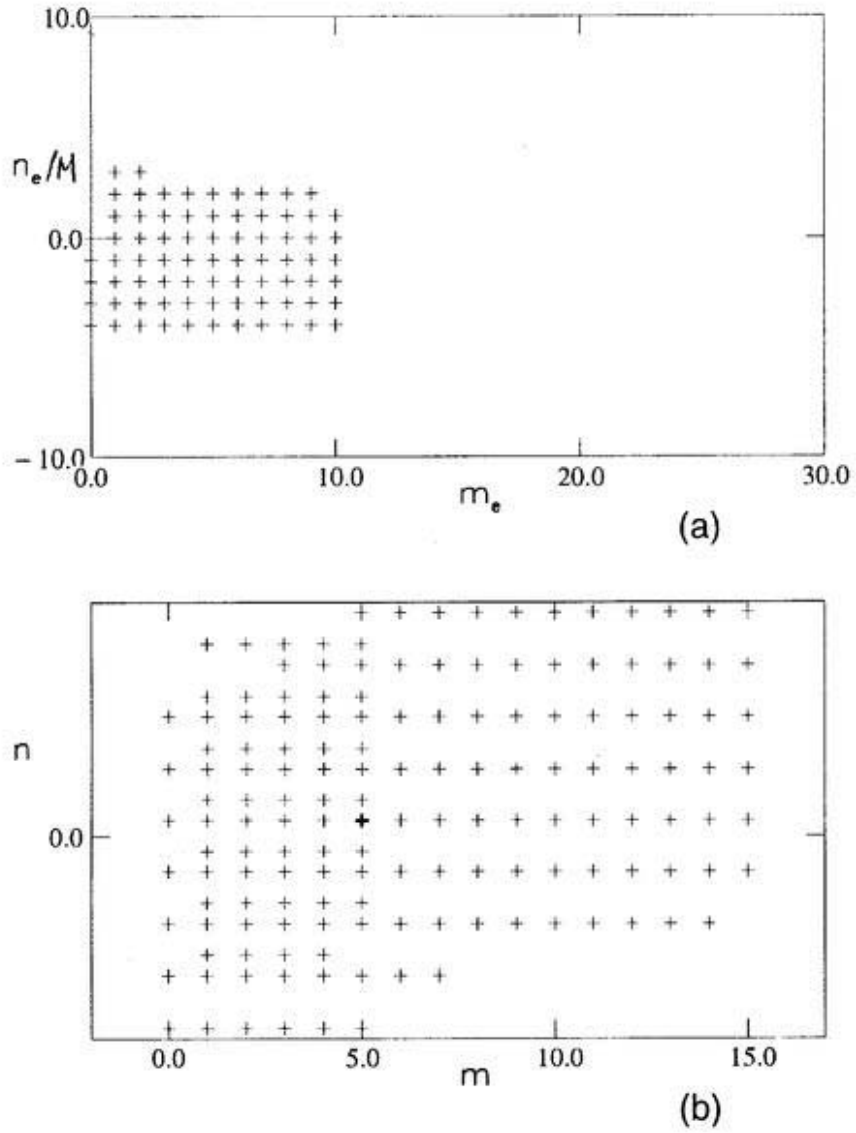

Figure B.1 Perturbation P1

Fourier modes of (a) Equilibrium; (b) Perturbation

$M_p = 5$, $N_p = 3$, $M_{eq} = 76$, $M_{pt} = 151$

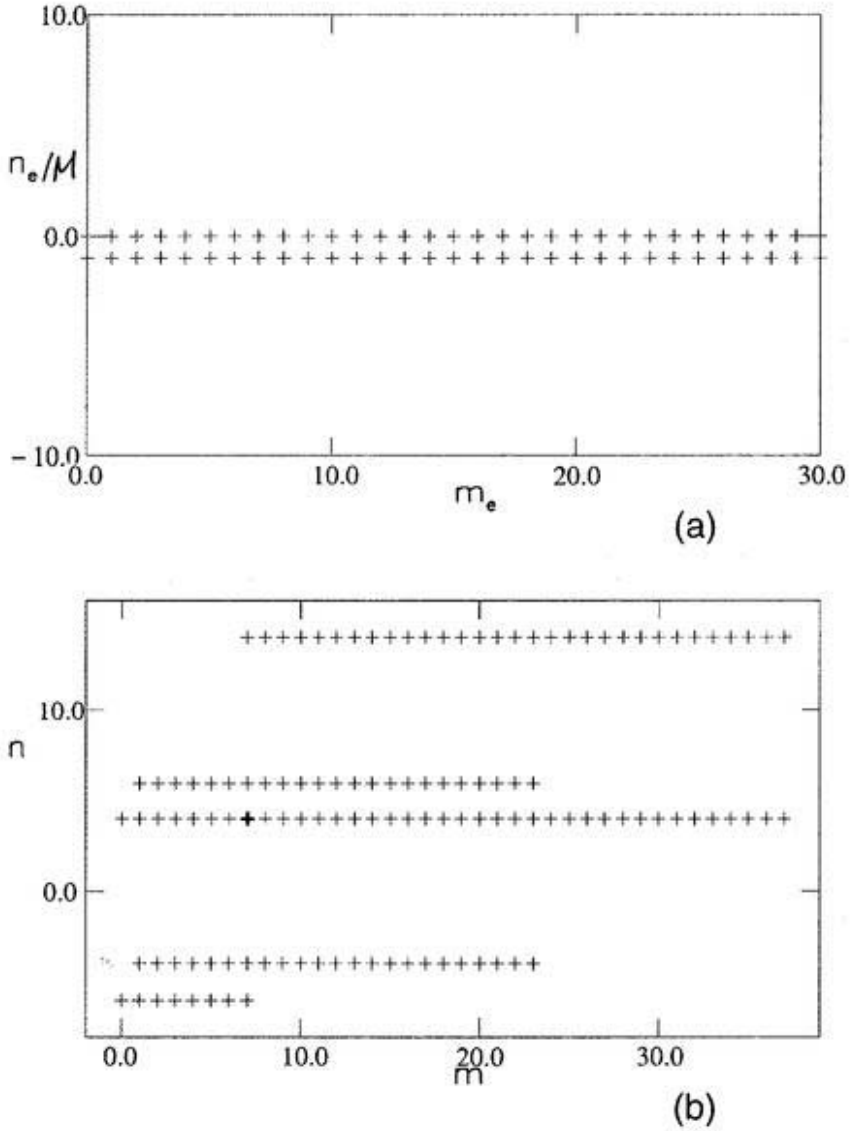

Figure B.2 Perturbation P2

Fourier modes of (a) Equilibrium; (b) Perturbation

$M_p = 7$, $N_p = 4$, $M_{eq} = 62$, $M_{pt} = 123$

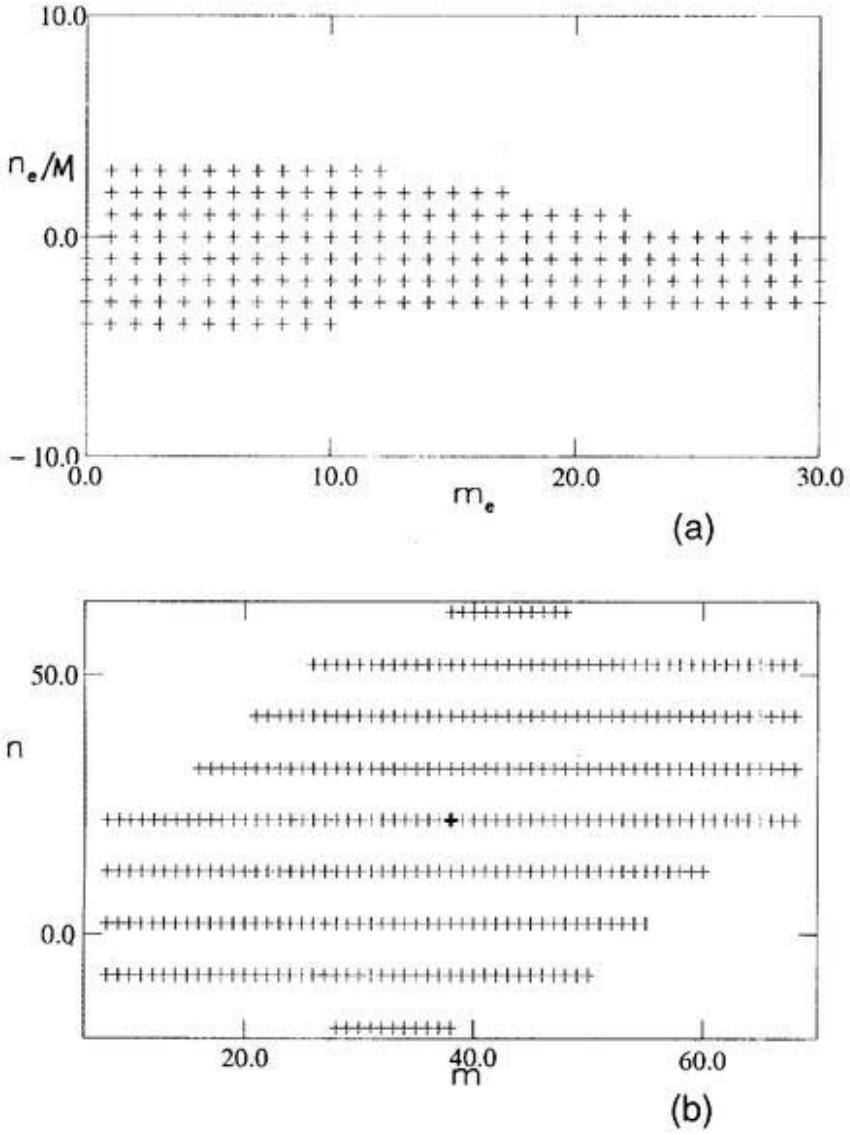

Figure B.3 Perturbation P3

Fourier modes of (a) Equilibrium; (b) Perturbation

$M_p = 38$, $N_p = 22$, $M_{eq} = 186$, $M_{pt} = 371$

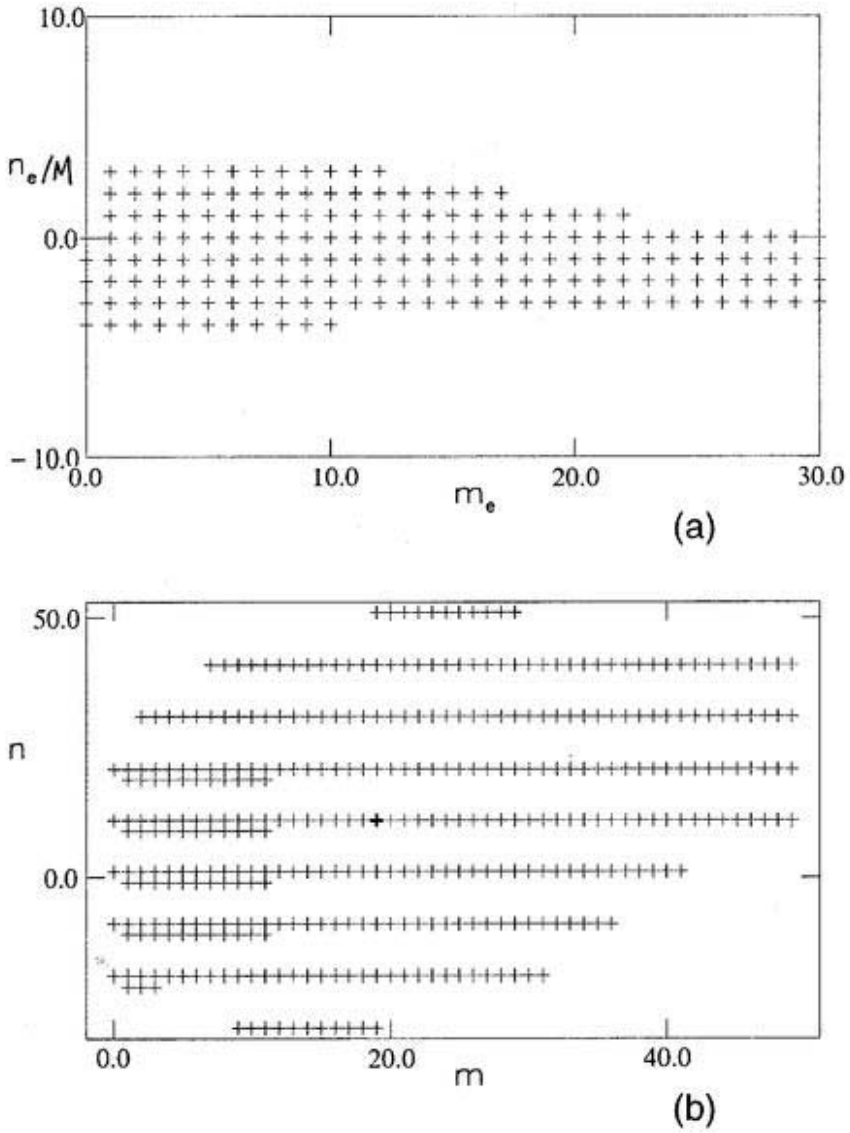

Figure B.4 Perturbation P4

Fourier modes of (a) Equilibrium; (b) Perturbation

$M_p = 19$, $N_p = 11$, $M_{eq} = 186$, $M_{pt} = 371$

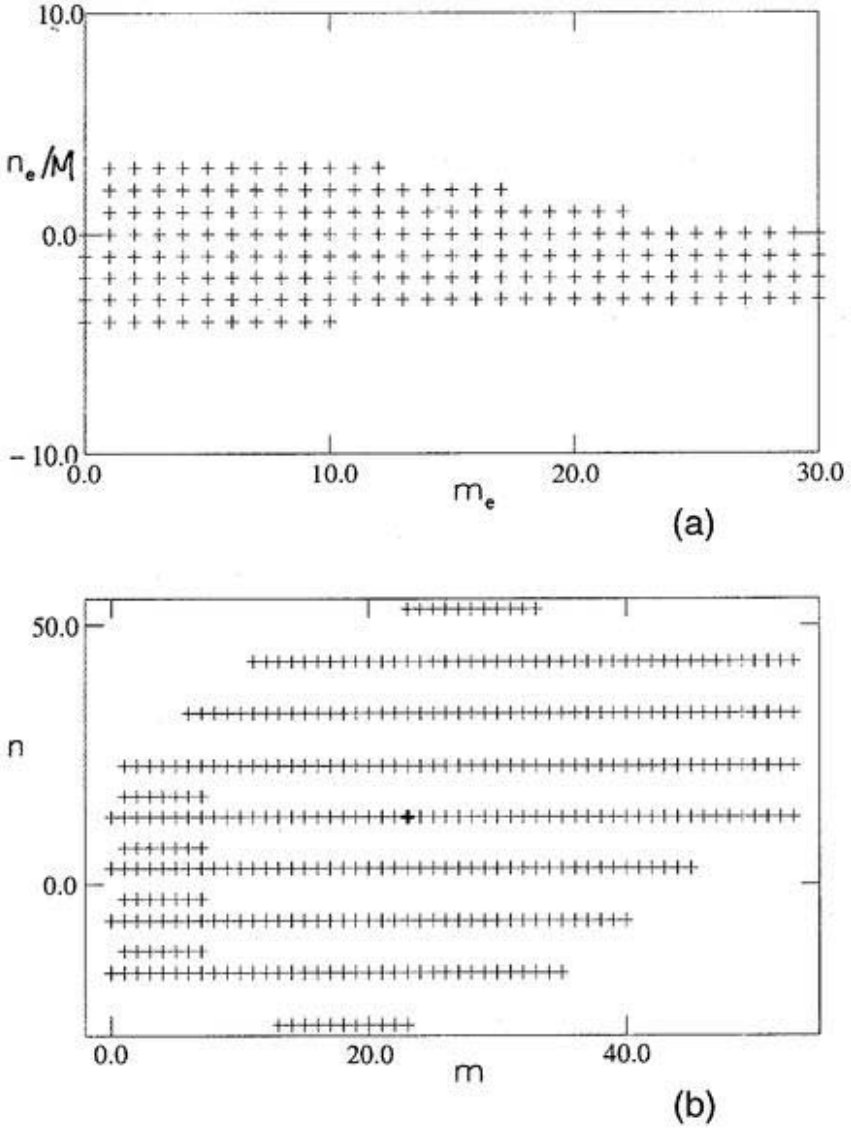

Figure B.5 Perturbation P5

Fourier modes of (a) Equilibrium; (b) Perturbation

$M_p = 23$, $N_p = 13$, $M_{eq} = 186$, $M_{pt} = 371$

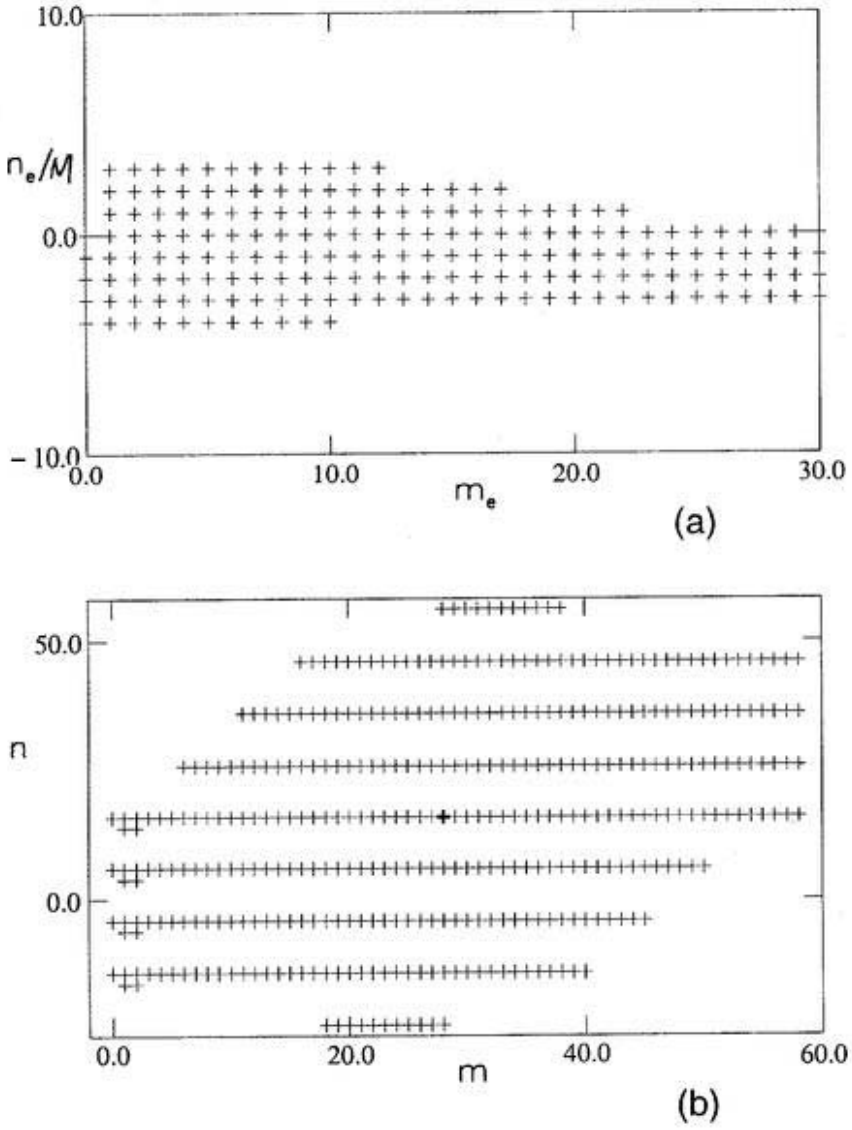

Figure B.6 Perturbation P6

Fourier modes of (a) Equilibrium; (b) Perturbation

$M_p = 28$, $N_p = 16$, $M_{eq} = 186$, $M_{pt} = 371$

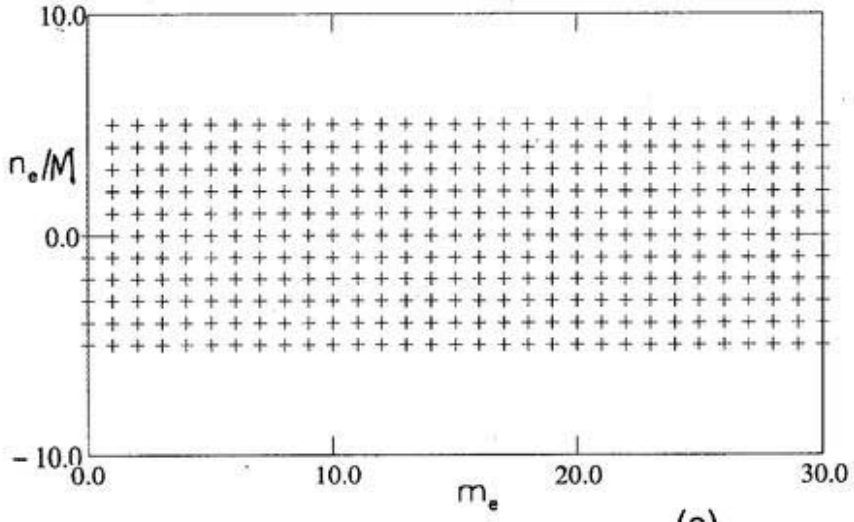

(a)

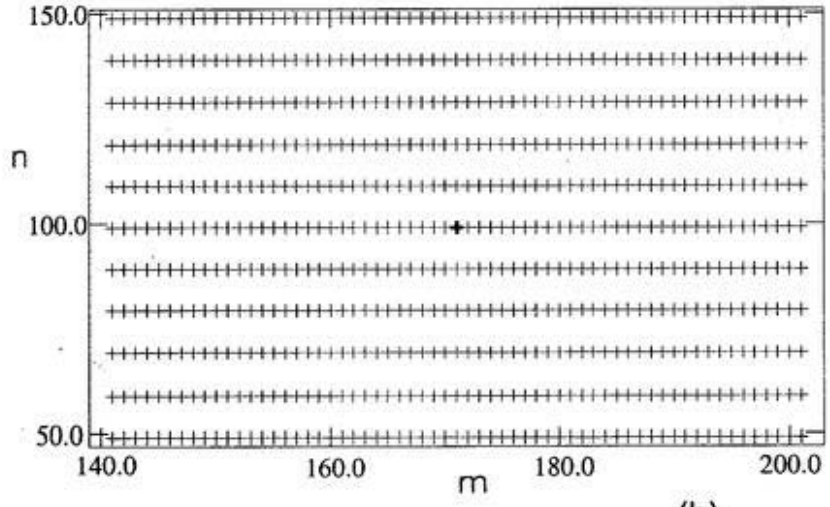

(b)

Figure B.7 Perturbation P7

Fourier modes of (a) Equilibrium; (b) Perturbation

$M_p=171$, $N_p=99$, $M_{eq}=336$, $M_{pt}=671$

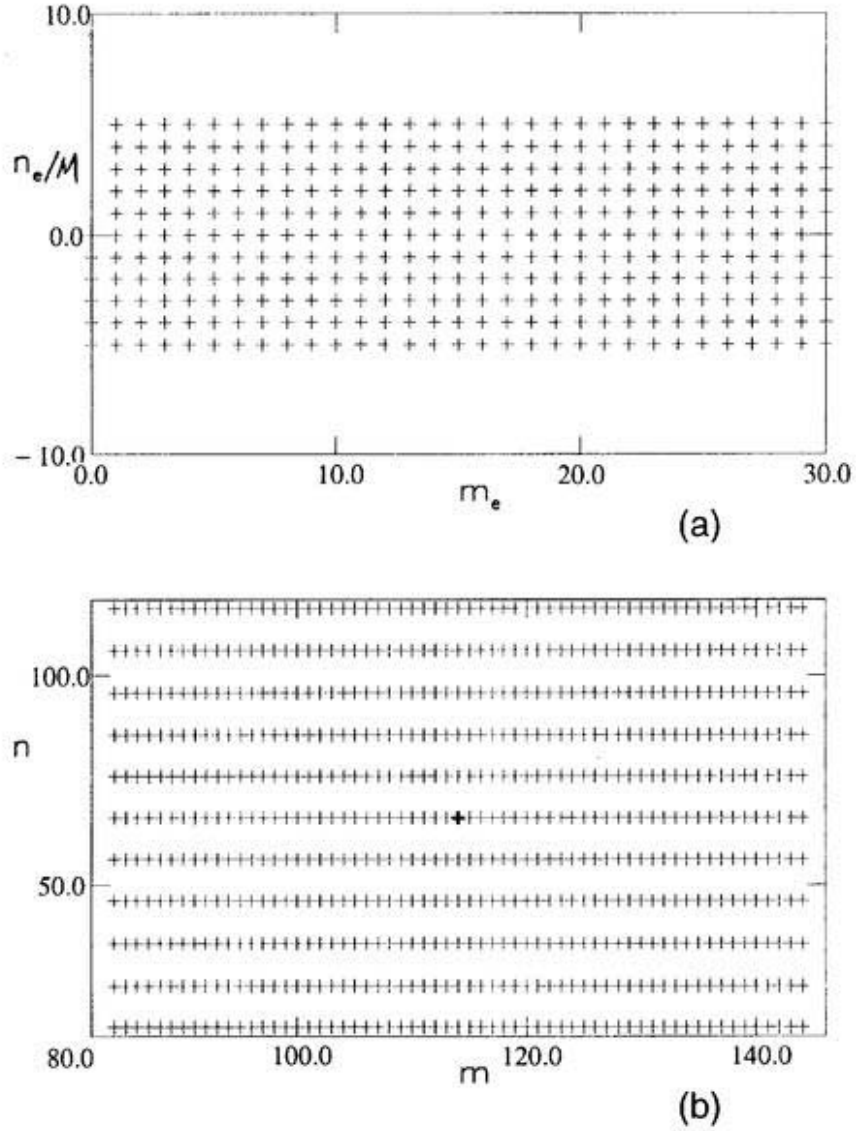

Figure B.8 Perturbation P8

Fourier modes of (a) Equilibrium; (b) Perturbation

$M_p = 114$, $N_p = 66$, $M_{eq} = 336$, $M_{pt} = 671$

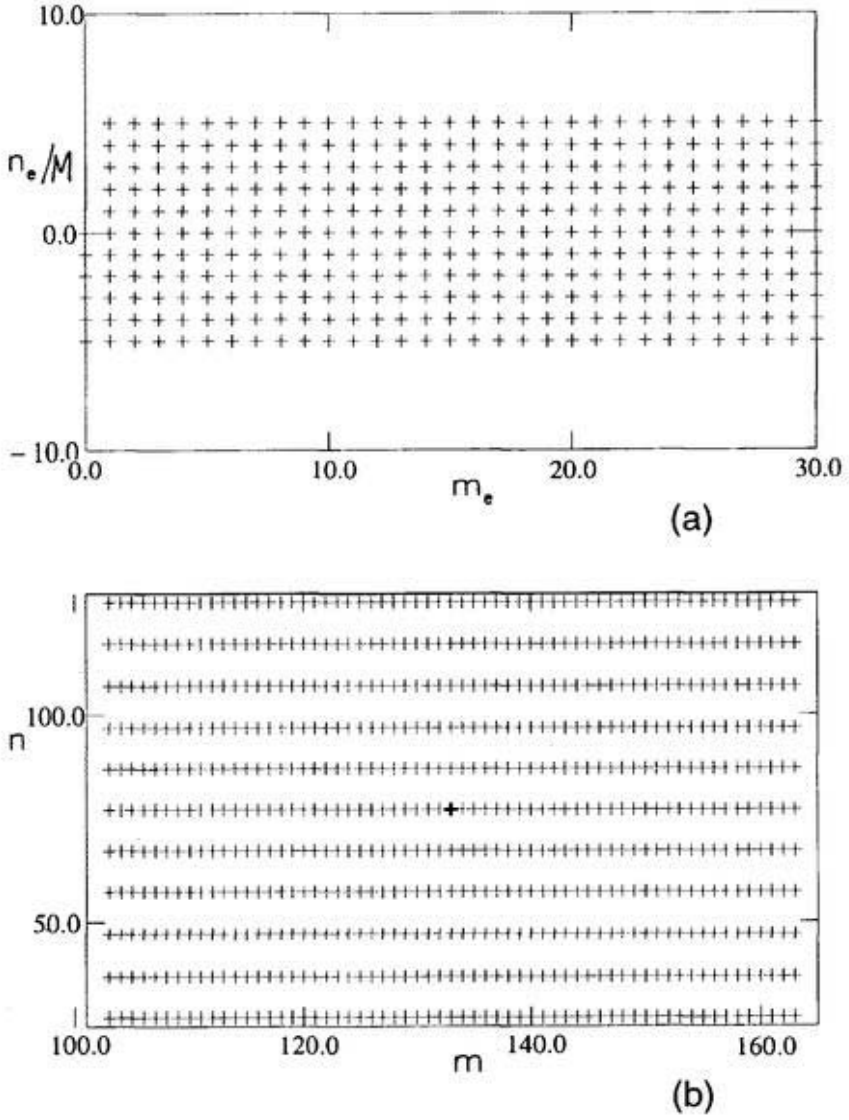

Figure B.9 Perturbation P9

Fourier modes of (a) Equilibrium; (b) Perturbation

$M_p=133$, $N_p=77$, $M_{eq}=336$, $M_{pt}=671$

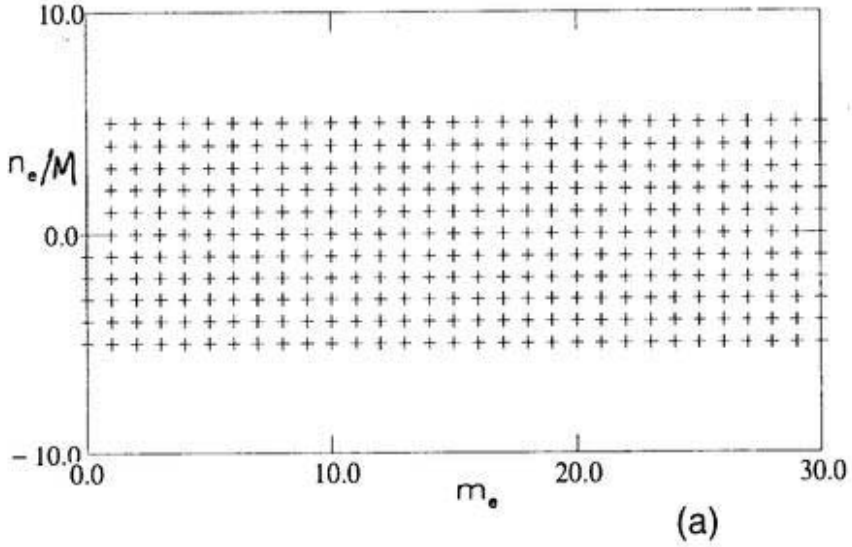

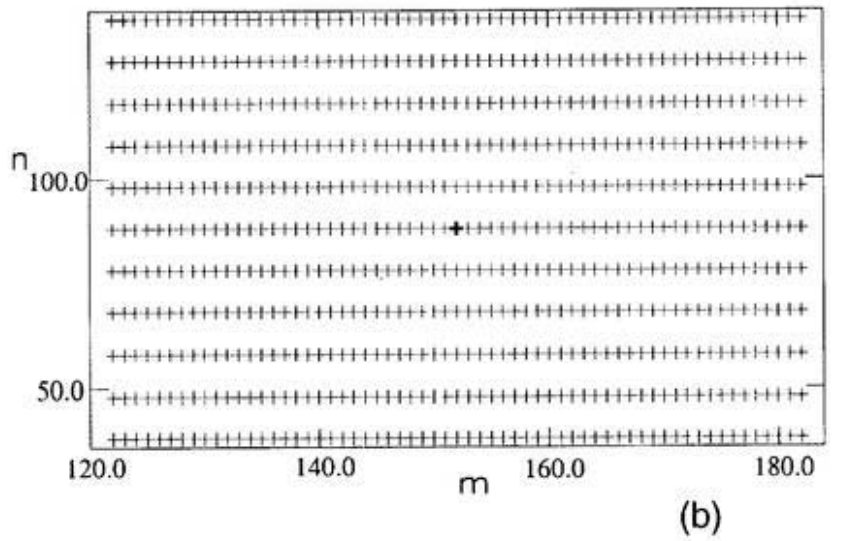

Figure B.10 Perturbation P10

Fourier modes of (a) Equilibrium; (b) Perturbation

$M_p = 152$, $N_p = 88$, $M_{eq} = 336$, $M_{pt} = 671$